

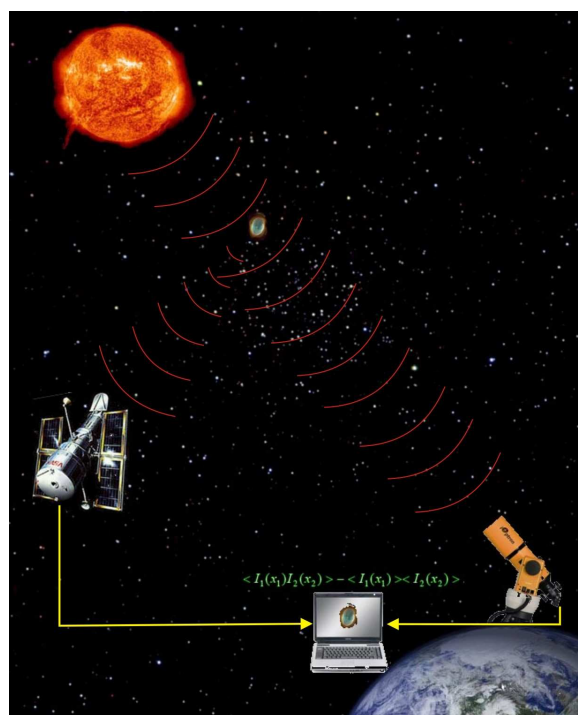
Ghost Imaging of Space Objects

Dmitry V. Strekalov, Baris I. Erkmen, Igor Kulikov, and Nan Yu

*Jet Propulsion Laboratory, California Institute of Technology,
4800 Oak Grove Drive, Pasadena, California 91109-8099 USA*

NIAC Final Report

September 2014



Contents

I. The proposed research	1
A. Origins and motivation of this research	1
B. Proposed approach in a nutshell	3
C. Proposed approach in the context of modern astronomy	7
D. Perceived benefits and perspectives	12
II. Phase I goals and accomplishments	18
A. Introducing the theoretical model	19
B. A Gaussian absorber	28
C. Unbalanced arms configuration	32
D. Phase I summary	34
III. Phase II goals and accomplishments	37
A. Advanced theoretical analysis	38
B. On observability of a shadow gradient	47
C. Signal-to-noise ratio	49
D. From detection to imaging	59
E. Experimental demonstration	72
F. On observation of phase objects	86
IV. Dissemination and outreach	90
V. Conclusion	92
References	95

I. THE PROPOSED RESEARCH

The NIAC *Ghost Imaging of Space Objects* research program has been carried out at the Jet Propulsion Laboratory, Caltech. The program consisted of Phase I (October 2011 to September 2012) and Phase II (October 2012 to September 2014). The research team consisted of Drs. Dmitry Strekalov (PI), Baris Erkmen, Igor Kulikov and Nan Yu. The team members acknowledge stimulating discussions with Drs. Leonidas Moustakas, Andrew Shapiro-Scharlotta, Victor Vilnrotter, Michael Werner and Paul Goldsmith of JPL; Maria Chekhova and Timur Iskhakov of Max Plank Institute for Physics of Light, Erlangen; Paul Nuñez of Collège de France & Observatoire de la Côte d’Azur; and technical support from Victor White and Pierre Echternach of JPL. We also would like to thank Jay Falker, Jason Derleth, Ron Turner, Katherine Reilly, and all of the NIAC team for continuous support, advice and encouragement throughout the entire research effort.

A. Origins and motivation of this research

Development of innovative aerospace technologies is critical for our nation to meet its goals to explore and understand the Earth, our solar system, and the universe. The spectacular success of many recent NASA missions hinges on the extensive technological innovations that NASA has been supporting for the past decades. To sustain this successful tradition it is very important to identify and stimulate the scientific research that may turn into a viable technology in the decades yet to come. Innovative low-TRL research stimulates the growth of the scientific knowledge and enhances the technological capabilities in a way that answers new questions and responds to new requirements. Such a research also helps finding novel creative solutions to problems constrained by schedule and budget. Moreover, the impact of this kind of research goes beyond the original area. A long-term advanced space concepts and technology development program is likely to have multiple and diverse positive outcomes.

The NASA OCT’s NIAC program which has sponsored this research effort is an example of such a long-term technological investment. This program has a history of seeding the research efforts that later turned into a great success. One of the most recent and spectacular examples of such an early innovation sponsorship is the Kepler planetary detection research

mission [1–3]. We use the achievements of this mission as benchmarks for our research.

Like the Kepler mission, our research lies in the area of observation astronomy. We aim to improve the technical methods and approaches available in this area and directed to investigation of such important space objects as exoplanets, asteroids, gravitational lenses, gas and dust clouds, and others.

Direct intensity measurement, by an eye or a detector, has always been the foundation of observation astronomy. Sometimes this technique is successfully complemented by other types of measurements, for example those relying on intensity interferometry. The pioneering application of intensity interferometric measurement in astronomy has been demonstrated by Hanbury Brown and Twiss in 1960s [4]. These measurements involved only a pair of detectors (coupled with telescopes) and were aimed at determining a star’s angular size. The success of this approach caused a brief but powerful wake of interest to intensity interferometry in the astronomy community. Unfortunately, further development of this technology was impeded by the limitations of contemporary optical detectors and fast electronics, as well as by limited computational power, for a few decades. Recently, however, the explosive progress in all these underlying technology fields revived the practical interest in intensity-interferometric imaging. It has been considered for imaging of solar spots, tidal and rotational distortions, limb darkening and other stellar phenomena [5–11]. Even a space-deployable version of this approach has been discussed [12].

Intensity correlation measurements proved to be also important in the area of science extremely distant from astronomy: in quantum optics. In particular, photon coincidence measurements have allowed for the study of nonclassical optical fields whose photons are emitted as tightly correlated pairs, e.g. in a process of parametric down conversion. Parametrically produced photons are not only tightly correlated in time, but also in space, even to the extent beyond possible in classical physics. (This phenomenon is one of the manifestations of the *quantum entanglement*.) Such a spatial correlation between parametric photons allows an observer to predict the “location” of one photon based on the observation of the other with a better resolution than is possible in a direct intensity measurement. It also enables a remarkable technique of optical imaging, called the “ghost imaging” [13].

Quantum world is usually associated with small size and low energy, and is believed to be governed by laws often defying the common sense. Quantum systems make wonderful objects for study, but rarely lend themselves as research tools in other areas of science and

engineering. Any such event in the history had truly revolutionary value. A few relevant examples are the laser, transistor, and superconductivity. It is therefore not surprising that the quantum optical phenomena attracts great interest as potential instruments for science and technology. The possibility to surpass the classical limits of optical resolution has been suggested for use in microscopic imaging [14] and lithography [15, 16]. The unique features of ghost imaging were proposed for spectroscopy [17, 18] and for the military surveillance [19] applications. In this research we take a further step and consider a possibility for application of ghost imaging (or speaking more generally, optical correlation imaging) in astronomy. We expect this approach to enhance the capabilities of conventional observation astronomy, as well as to create conceptually new capabilities.

B. Proposed approach in a nutshell

The term “ghost imaging” was coined in 1995 when an optical correlation measurement using biphoton light from parametric down conversion crystal was used to observe an image [13] or a diffraction pattern [20] of a mask placed in the *signal* channel by scanning a detector in an empty *idler* channel. This image is obtained by a gated photon counting, with the gating obtained by photon detections in the signal channel which lacks any spatial resolution, as illustrated in Fig. 1.

Besides its significance for the field of quantum optics, the ghost imaging technique has a few appealing practical advantages. Since no spatial resolution in the object channel is required, a very primitive single-pixel optical sensor could be placed in this channel, while the more advanced optics responsible for the image quality could be placed in the reference channel. This could be convenient for imaging of hard-to-access objects. The ghost imaging is especially beneficial for imaging the objects at “inconvenient” wavelengths, such as far infrared, while the reference channel wavelength is visible [17]. Furthermore, the coincidence measurement technique is more robust in the presence of the optical background illumination. Finally, the possibility of surpassing the diffraction limit in ghost imaging has been discussed. However here one should be careful to acknowledge that while the transverse intensity correlation of parametric photons is not limited by the signal or idler diffraction, it is limited by the pump diffraction.

Despite these potential advantages, the first realization of ghost imaging was extremely

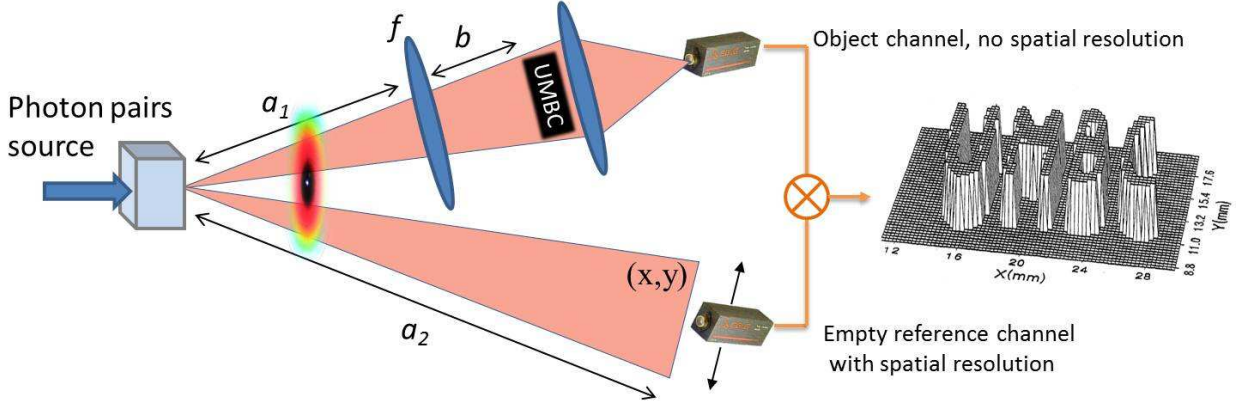


FIG. 1: Simplified illustration of the original ghost imaging experiment [13]. A mask with letters “UMBC” is placed in the object channel, where all light is collected by a “bucket detector”. Nonetheless, an image is reconstructed by correlating this detector’s photo counts with those from another detector, raster-scanning the *empty* reference channel. A sharp image is observed when a modified thin lens equation is fulfilled: $1/(a_1 + a_2) + 1/b = 1/f$.

far from any practical applications, and especially from astronomy. Indeed, the need for a laser-pumped source of photon pairs and for collecting of all light in the object channel (which means that the object has to be placed in the close vicinity of the collection optics) effectively ruled out such applications.

A first step towards practical ghost imaging was made ten years after its initial demonstration, when it was shown that the two-photon correlation properties of common thermal light are applicable for ghost imaging [21, 22]. Since thermal light sources are much more abundant than parametric light sources, and in particular in space, this realization has been very important. Next, it was shown that collecting all the light in the object channel (the “bucket detection”) is not required, and that only some small portion of scattered light could be collected instead [19]. This has allowed the object to be placed at a large distance from the observer. Remarkably, the approach by [19] has already relied on the pseudo-thermal light source rather than on parametric light, as shown in Fig. 2.

However, using thermal light sources brings about a new complication: a beam splitter that has to be placed between the source and the object (see Fig. 2). This beam splitter is needed to create the reference channel whose speckle pattern duplicates that in the object channel, enabling the intensity correlation imaging. Such a geometry can be easily

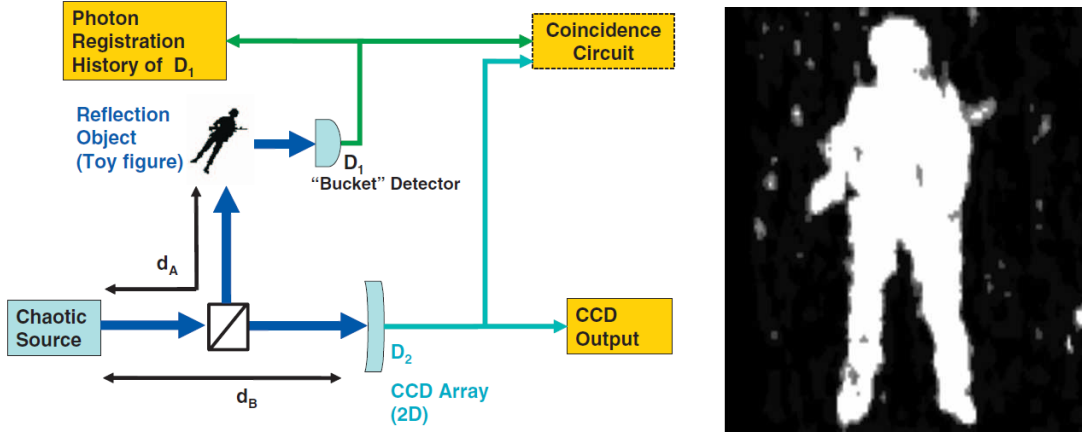


FIG. 2: Using a thermal light source with a point-like detector collecting the light scattered by an object gives access to ghost imaging of distant and hard to access objects. Experimental diagram and image from [19].

implemented in a lab, but becomes problematic when both the source and the object, and possibly the observers, are located far in space.

This is the key problem we need to solve in our research. Our approach is illustrated in Fig. 3. Its main idea is that an object that partially transmits and partially reflects or scatters light, can itself play the role of the beam splitter. Moreover, even a perfectly opaque scattering object may under certain conditions (as discussed below) create coherence between the transmitted and scattered light, which may be utilized for the intensity correlation imaging. Since the object is present in both channels, this approach leads us away from “conventional” ghost imaging towards intensity interferometry of the Hanbury Brown and Twiss type. The similarities and distinctions of these two types of imaging have been discussed in literature [23]. In our case, an important distinction is that we will not be concerned with the angular size or other properties of the source, which will be assumed to be known. Instead, we will study how the object’s geometry and location relative to the source and observer affect the intensity correlation. We will attempt to restore these parameters from the correlation measurements and show that these results could provide important information complementary to conventional direct observations.

Configuration shown in Fig. 3(b) can be realized in three different ways, when both, one or none of the detectors receive the direct light from the source in addition to the object-scattered light. The mission concepts arising from the last two configurations are illustrated

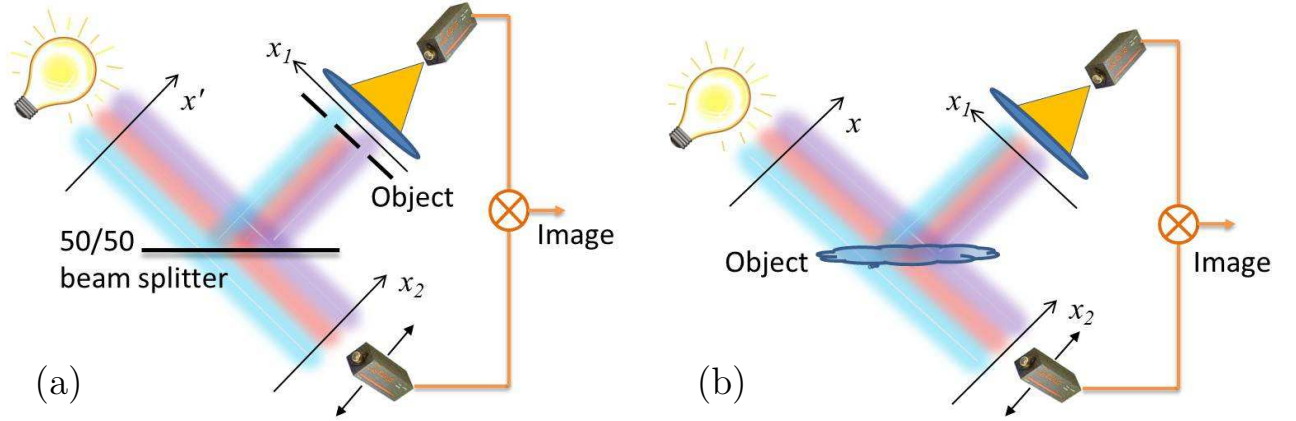


FIG. 3: Conceptual schematic of conventional thermal light ghost imaging setup (a) and of our approach (b). Colors represent transverse optical modes (speckles) responsible for the excess intensity correlation and providing the physical mechanism for the correlation imaging.

in Fig. 4 (a) and (b), respectively.

Obviously, shielding one or both detectors from the direct source light provides reduced background signal and appears advantageous, as well as simpler to analyze. However, it requires the source and object to be optically resolvable and may require placing one or both detectors in space far apart from each other. For very distant objects this may not be feasible. In the following analysis we will assume that both detectors see the direct as well as scattered (in the nearly forward direction) light, thereby realizing the scenario from

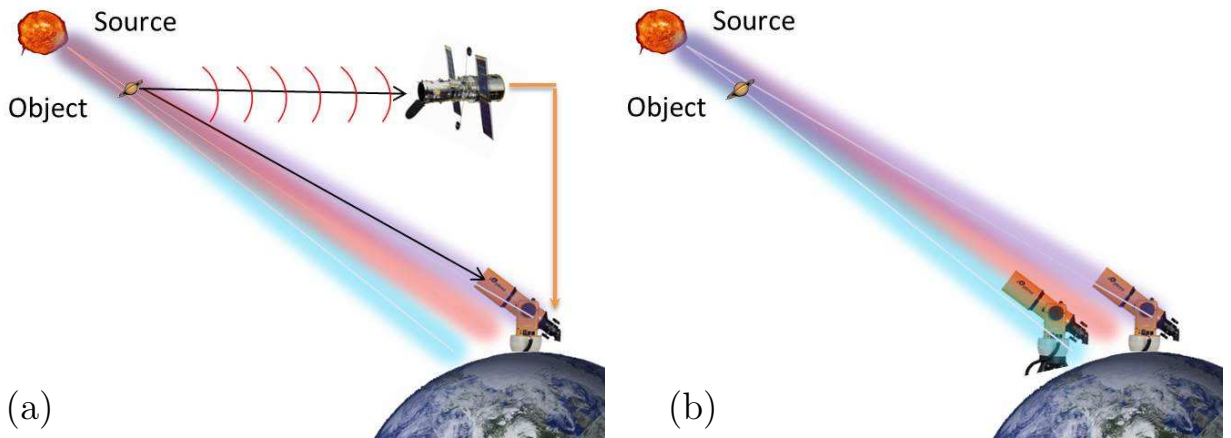


FIG. 4: Two possible mission scenarios that may arise from the measurement schematics in Fig. 3(b): one detector receives only scattered light (a); both detectors receive scattered as well as the direct light (b).

Fig. 4(b).

Below we will develop and test a simple analytic model that will allow us to study the intensity-correlation signatures of simple test objects. Based on this model we will make predictions concerning the observability of various space objects, and concerning their parameters that can be inferred from such observations. We will show that the object's image reconstruction is possible when an array of detectors is used, such as shown in Fig. 5. By the “image” here we will understand the object's column optical density in the line of sight direction. In the case of fully opaque objects such imaging is equivalent to reconstruction of the object's contour.

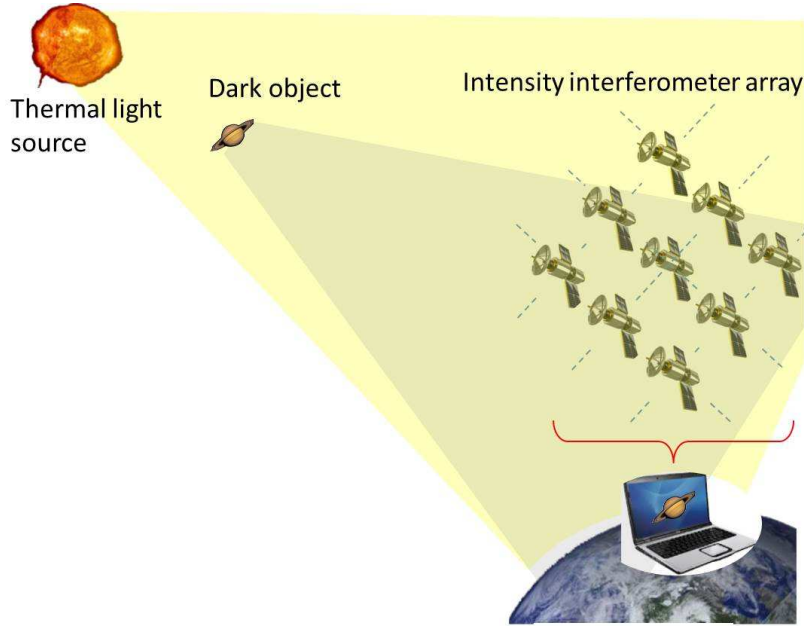


FIG. 5: In this mission concept an array of detectors is used to reconstruct the dark object's image from intensity interferometry data. The array can be either ground-based or space-based as shown.

C. Proposed approach in the context of modern astronomy

High angular resolution is indisputably the main figure of merit in astronomical observations and the main parameter in astronomy missions. Different missions performance with respect to this parameter at different wavelengths is summarized in Fig. 6. This figure also includes the projected performance of an intensity interferometer based on the Cherenkov Telescope Array (CTA) facility, which will be discussed in more details in the following. It

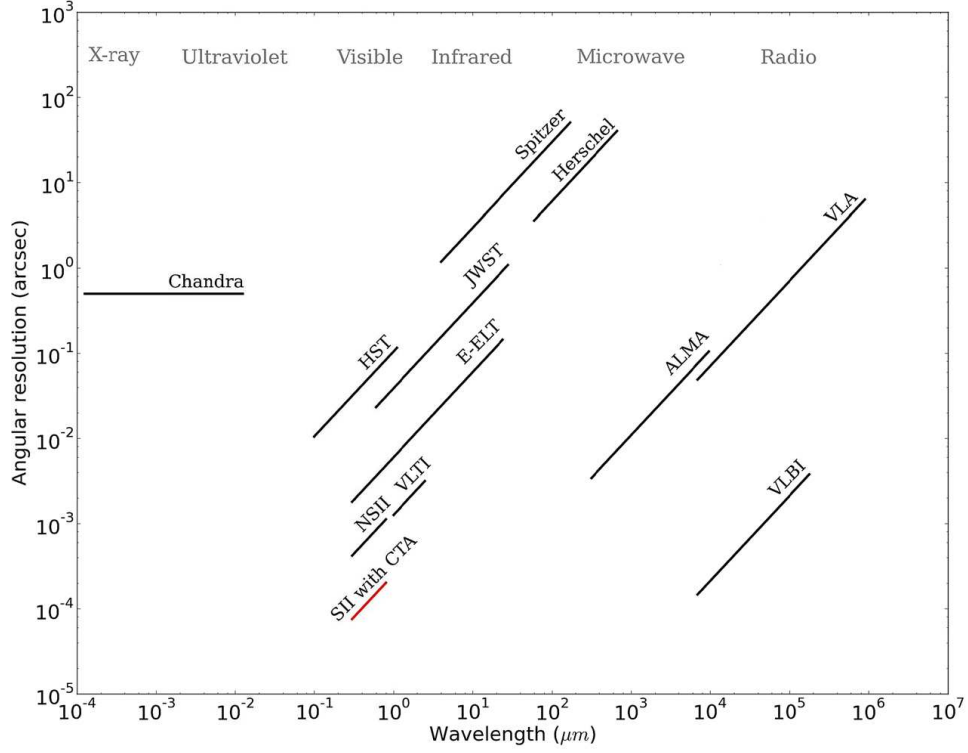


FIG. 6: The angular resolution chart illustrating various approaches capabilities. Projected capability of the intensity-interferometric technique based on the Cherenkov Telescope Array (CTA) facility is shown in red.

should be mentioned that the majority of stars in the Bright Star Catalogue have the angular size below 1 milliarcsecond, hence a much better resolution is required to observe any stellar features. The merit of the intensity interferometry in reaching this goal is evident. As a further advantage it should be mentioned that this approach is immune to atmospheric turbulence and therefore can be implemented on the ground. The turbulence limits the useful aperture of ground-based telescopes and field interferometers to approximately 60 cm; by contrast, the CTA effective aperture (the interferometer baseline) is going to reach 2 km.

We have already mentioned the sharp rise of the enthusiasm regarding the intensity interferometry applications in astronomy, which has followed Hanbury Brown and Twiss discovery but quickly subsided due to insufficient detection techniques available in the mid-20th century. Presently, the field experiences an evident revival, as can be seen from the growing number of research activities and publications in the field. For example, the University of Utah has recently (in Spring 2014) deployed a pair of 3-m diameter segmented

optical telescopes at StarBase-Utah [7]. These telescopes use photomultiplier tubes on the focal plane to detect starlight. As another example, E. Horch's group at the Southern Connecticut State University [24] carries out measurements with a 53 m baseline stellar intensity interferometer using single-photon avalanche photodiodes (SPAD) for detection. It is important to realize that the telescopes in the intensity-interferometric array need not have high imaging quality. Since the connection between them is not optical but only electronic, their error budget relates to the electronic time resolution. For example, 10 ns resolution corresponds to 3 meters light-travel distance, which greatly relaxes optical quality requirements and reduces the project cost.

Rather than building dedicated intensity-interferometric telescope arrays and high-speed detectors and electronic networks, it may be beneficial to leverage already existing Cherenkov telescopes arrays. Such arrays are equipped with high-resolution photon detectors and correlation electronics that is required for study of high-energy cosmic particles and can also be used for intensity interferometry measurements.

A few of such arrays presently exist worldwide, e.g. the High Energy Stereoscopic System (H.E.S.S.) in Namibia, see Fig. 7; the High Altitude Gamma Ray Telescope (HAGAR) in India (which is the site of the 21-m Major Atmospheric Cherenkov Experiment (MACE) telescope); Very Energetic Radiation Imaging Telescope Array System (VERITAS) in southern Arizona, measuring digital correlations between pairs of 12-m telescopes with 1.6 ns resolution [6]; Major Atmospheric Gamma-ray Imaging Cherenkov Telescopes (MAGIC) on La



FIG. 7: The High Energy Stereoscopic System (H.E.S.S.) telescopes array in Namibia.

Palma; and CANGAROO in Australia. Some of these projects are open to external research proposals, which can provide a path for the future developing of our project.

Finally, as the larger-scale effort, we should mention the CTA Consortium. It is a large international project designed to deploy a network of telescopes equipped with high-speed photodetectors and high-bandwidth time-correlation electronics. The CTA array will consist of 50-100 telescopes spread over a few square km, as shown in Fig. 8 .

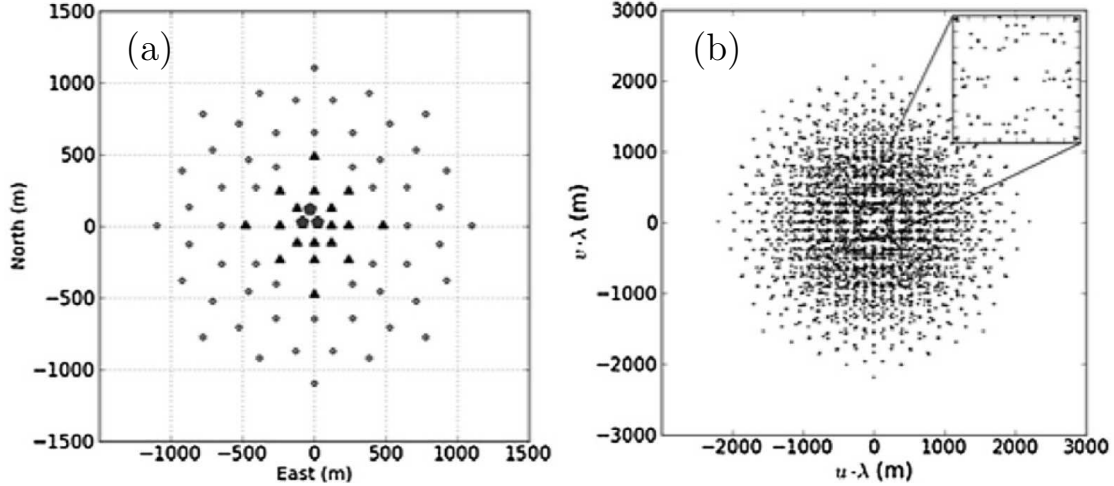


FIG. 8: One possible layout for the CTA (a) and its instantaneous reciprocal (Fourier) plane coverage in the zenith direction (b), from [8].

Various types and sizes of telescopes are considered for the CTA project. One of the most likely candidates is the SST-1M prototype, which is shown in Fig. 9. This telescope is developed by a subconsortium of Polish and Swiss institutions. It will be equipped with a novel fully digital camera based on SPADs. The telescope features a Davies-Cotton optical design with focal length $f=5.6$ m and the reflective dish of 4 m diameter, that is composed of 18 hexagonal mirror facets. The large field-of-view will allow the scans of extended regions of the sky in search of the most powerful accelerators of galactic cosmic rays. The SST-1M has been conceived to be easily mass-producible by using standard industrial technology and materials, easy to transport and install. The telescope weight, including camera and auxiliary systems, is about 9 tons. Given the compactness and weight of the structure, three telescope structures can be packed in a standard open-top 12 m container for the shipping from the production site to the assembly point. This design achieves currently the lowest costs for the SSTs.



FIG. 9: An SST1M telescope is a workhorse of the CTA project. This telescope is designed for light collection rather than for imaging, which considerably offsets the costs of its mass-production.

Close collaboration between the CTA Consortium and the intensity interferometry community is anticipated. An international workshop dedicated to intensity interferometry has been held in Nice in May 2014, featuring the progress of research groups from all over the world, including ours. The workshop was co-located with the CTA Consortium meeting and highlighted in a CTA newsletter.

Provided with suitable software, the CTA could become the first kilometer-scale optical intensity interferometer, reaching into novel microarcsecond resolution domains. Imaging luminous objects, it could reveal the surfaces of rotationally flattened stars with their circumstellar disks and winds, monitor a nova eruption, or possibly even visualize an exoplanet during its transit across some nearby star. Such measurements are in fact planned for the CTA during down time of its main operations (e.g., due to full Moon).

The most traditional goal of stellar intensity interferometry is to measure the stars angular diameter. These measurements can provide information of the effective temperature, which can be obtained by measuring the angular radius and the parallax (distance) [25]. When combined with spectroscopic and spectrophotometric measurements, it can also be used to make inferences regarding stellar atmospheres [26].

The advance of the detection and analysis techniques enabled other, even more ambitious goals, such as the study of rapidly rotating stars. Local gravity of such stars can be considerably reduced (even approaching zero) in the equatorial regions, which leads to apparent darkening of these regions. Rotation also leads to oblateness of the star disk.

Another important class of astrophysical systems that could be potentially studied with intensity interferometry technique are binary systems. Resolving such system and measuring their orbital parameters can provide important information regarding the stars' masses and possibly mass flow. The mass flow can also be studied in the case of radiatively driven stellar mass loss [27], such as may occur in hot O and B type stars. Finally, stellar features similar to solar spots and jets may also be accessible for intensity interferometric observations. A more detailed review of various stellar objects of interest that can be observed by this technique is available in [9].

Our approach significantly expands the list of potential objects of interest for astronomical intensity interferometry, including in it dark and potentially purely refracting (phase) objects eclipsing celestial light sources. Perhaps the most important class of such objects are exoplanets. Exoplanets have been already mentioned in the context of “conventional” intensity interferometry. In this context they are considered as dark spots on their host stars. While this may be a good approximation in many cases, our approach provides a more accurate treatment accounting for the distance between the planet and the star. This correction becomes important when the distance between the light source and the object approaches the distance between the object and the observer. Such situations arise in cases when the dark objects of interest are black holes, neutron stars, gas and dust clouds, Kuiper belt asteroids, and various other non-radiating objects. In the following section we will discuss the variety of such objects and the potential scientific payoff from their study in more detail.

D. Perceived benefits and perspectives

Historically, new frontiers in astrophysics have opened whenever new observation concepts become available. Intensity interferometry has already been considered for imaging a variety of stellar phenomena including tidal and rotational distortions, limb darkening and others. The proposed approach will enable new revolutionary observation techniques

granting astrophysicists the access to some of the most elusive and intriguing objects of the Universe: those that do not emit their own light. The scientific value and the impact to the state of knowledge of such studies is emphasized in the NASA 2011 Strategic Plan. Specifically, the document states that as a part of NASA's pursuit to further the understanding of how the universe works, explore how it began and evolved it seeks to improve understanding of the nature of black holes, dark energy, dark matter, and gravity, as well as to generate a census of extra-solar planets and determine their properties. In the latter context the search for Earth-like planets is considered to have a special priority.

In addition to the scientific merits discussed above, our research pursues the technological priorities defined in the 2010 Decadal Survey for Astronomy and Astrophysics, such as a broad support for high-resolution instrumentation for both stellar physics and exoplanet searches. In this context, we strive to develop an observation technique capable of advancing the optical resolution by potentially orders of magnitude compared to even most ambitious direct space telescopes and amplitude space interferometers. This goal is pursued by multiple research groups worldwide, which confirms its underlying principles and emphasizes its significance. However, the uniqueness of this JPL research is that we are the first to develop application of this technique to non-radiating objects. Observation and imaging of dark objects, such as those listed above, is one of the important but most difficult problems in astronomy. It becomes especially challenging when an object can scatter little or no star light, so its main optical effect is limited to gravitational bending of optical rays from background sources, known as gravitational lensing and microlensing. Objects that can potentially cause gravitational lensing, such as black holes, hypothesized dark matter, or neutron stars, are among the most intriguing astrophysics objects that are the key to understanding the origin and fundamental physical principles of our Universe.

The technological power of our approach is based on high resolution of intensity interferometers, at the levels that cannot be rivaled by first-order interferometry or telescopes with realistic apertures. While the Rayleigh criterion still applies to intensity interferometers, it is set not by an individual detector's aperture but by the entire size of the detectors array. Intensity correlation imaging therefore may be compared to the synthetic aperture approach with telescope arrays. However while the synthetic aperture approach requires positioning of the array element with precision and stability at the level of a fraction of the optical *wavelength*, intensity interferometers only need it at the level of the *coherence length*. The

coherence length, determined by the optical filter bandwidth, may exceed the wavelength by orders of magnitude. The optical and electronic path lengths stability requirements are relaxed accordingly, which affords larger observation baselines, and consequently, better resolution. One of the important consequences of this is that the intensity correlation technique is practically immune to atmospheric perturbations and in some cases circumvents the necessity of going to space for high-resolution observations. This in turn lifts a large number of stringent constraints, which brings about further significant benefits.

Let us briefly discuss some of the dark celestial objects that may be observable with our intensity interferometry technique.

- **Exoplanets.** In March 2014 NASA’s Kepler mission announced the discovery of 715 new planets. These newly-verified worlds orbit 305 stars, revealing multiple-planet systems much like our own solar system. This discovery marks a significant increase in the number of known small-sized planets more akin to Earth than previously identified exoplanets. High-resolution imaging of these planets by intensity interferometry technique will allow NASA to acquire information regarding their orbits orientations, presence of moons, and possibly the presence and state of atmosphere. Intensity-interferometric analysis of Kepler data is also important for eliminating the false positives and more accurate modeling of the light curve [28]. The false positives may arise due to a binary background star that could mimic planetary transient or even due to a normal background star offsetting the transient light curve, as has been the case with Kepler21b and Kepler14b [29].
- **Kuiper belt and Oort cloud asteroids.** These objects are observed while occasionally obscuring the background stars [30–36]. Understanding the nature and composition of these objects is important for understanding the origin of the Kuiper belt and Oort cloud and of the underlying astrophysics. Such understanding may be gained by intensity-interferometric study of the objects shapes and sizes.
- **Black holes.** These objects fall into the category of predominantly phase objects as described above. Their close study has great scientific merit. Unfortunately, stellar-mass black holes are very rare. Nonetheless, a remarkable discovery was reported [37] earlier this year of a black hole orbiting a star MWC 656. Investigating of this

and similar systems may greatly benefit from our approach. For example, plumes of accretion may be revealed.

- **“Phase screens” due to cold gas clouds in space.** Such gas clouds are thought to be responsible for the “hidden” mass and may present an alternative to “dark matter” [38, 39]. Studying their density distribution encoded in the transmitted light phase gradient (aka the stellar scintillation) is yet another exciting application for high-resolution intensity-interferometric imaging in the optical range.

Our approach implies a very specific observation scenario, when the object of interest passes between a light source and the observer. While perfect alignment of these three parties is not required, we have shown theoretically [40] and experimentally (see Section III D. below) that the object signature diminishes rapidly as the object moves outside the angular size of the source as seen by the observer. It is clear that although stars occultations are not uncommon in astronomy, and in fact constitute a base for some types of exoplanets [1–3] and Kuiper belt asteroids [30–36] observations, identifying appropriate object-source pairs requires a thorough investigation which would amount to a separate research effort. Here, we provide only a quick review of potential source candidates. The most promising sources are the largest and most distant (in order to increase the observation volume), but at the same time the brightest (in order to increase the signal) stars. An list of several such stars is given in Table I. Here the full angular sizes of stars θ are given in milliarcseconds (mas). The peak emission wavelength λ_p is found from the black body radiation model, and the speckle size is evaluated for this wavelength based on the distance and angular size. The speckle size d_{sp} is the full width at half maximum of the transverse auto-correlation function of a disk source

$$|G_{12}(x)|^2 = \left(\frac{J_1(2\pi\theta x/\lambda_p)}{2\pi\theta x/\lambda_p} \right)^2 \quad (1)$$

(see discussion in the next chapter). It is found from the condition

$$d_{sp} \approx \frac{1.62\lambda_p}{2\pi\theta}. \quad (2)$$

Unfortunately, the stars that are known to have planets have considerably smaller apparent magnitude, which implies more difficult observations. Some of such stars that are brighter than apparent magnitude 9 are listed in Table II. The angular sizes of stars and

planets in this case are smaller and measured in microarcseconds (μas) instead of milliarcseconds. The planet sizes are inferred from their masses, that are in turn evaluated from Doppler measurements of the radial velocity shifts of the host stars. Such inferences may not be accurate due to various planetary composition and density.

Star	Angular size (mas)	Distance (pc)	Apparent magnitude	T (K)	λ_{peak} (nm)	Speckle size (m)
Betelgeuse	51.6	197	0.42	3400	850	0.88
Arctur	20.6	11	-0.04	4300	670	1.7
Aldebaran	20.4	20	0.85	3900	740	1.9
Capella A	8.9	12.9	0.91	4900	590	3.5
α Centauri A	8.3	1.3	1.3	5300	550	3.5
Pollux	7.8	10	1.1	4700	620	4.2
Canopus	6.8	96	-0.72	7400	390	3.0
Procyon	6.6	3.5	0.34	7700	380	3.1
Capella B	6.6	12.9	0.76	5700	510	4.1
Sirius	6.2	2.6	-1.47	9900	290	2.5
Vega	3.1	7.7	0.03	9600	300	5.1
Altair	2.9	5.1	0.77	7700	380	7.0
Rigel	2.7	260	0.12	12100	240	4.8
Deneb	2.3	800	1.25	8500	340	8.0
Fomalhaut	2.1	7.7	1.16	8600	340	8.8

TABLE I: Parameters of some stars that could be potentially used for imaging dark celestial objects by intensity interferometry.

Star	Star size (μ as)	Planet size (μ as)	Distance (pc)	Apparent magnitude	Temperature (K)	λ_{peak} (nm)	Star speckle size (m)	Planet speckle size (m)
Upsilon Andromedae	1021	108	13.5	4.09	6107	474	24.7	234
82 G. Eridani	1396	23	6.1	4.254	5401	537	20.4	1216
HD 60532	921	72	25.4	4.46	6095	475	27.4	352
61 Virginis	1040	28	8.6	4.74	5531	524	26.7	976
47 Ursae Majoris	772	90	14.1	5.10	5892	492	33.8	289
Mu Arae	809	73	15.6	5.15	5704	508	33.3	371
HD 47536	1608	15	123.3	5.26	4379	662	21.9	2422
Nu ² Lupi	671	13	14.4	5.65	unknown	unknown	unknown	unknown
HD 142	509	63	25.8	5.70	6180	469	48.9	393
Gliese 777	700	68	15.9	5.71	5588	519	39.3	405
HD 169830	469	41	36.5	5.91	6266	462	52.3	602
HD 38529	668	61	39.2	5.94	5697	509	40.4	443
55 Cancri	872	119	12.3	5.95	5217	555	33.8	248
HD 69830	659	18	12.6	5.95	5385	538	43.4	1597
HR 8799	315	28	39.6	5.96	7429	390	65.7	730
HD 217107	611	64	19.9	6.18	5646	513	44.6	423
HD 134060	unknown	21	24.2	6.29	unknown	unknown	unknown	unknown
HD 11964	632	24	32.8	6.42	5522	525	44.1	1153
24 Sextantis	588	15	77.6	6.44	5098	568	51.4	1988
23 Librae	446	42	26.1	6.45	5559	521	62.0	660
HD 1461	439	7	23.3	6.47	5765	503	60.8	3747
HD 200964	unknown	12	68.4	6.49	5164	561	unknown	2564
HD 96700	unknown	13	25.4	6.50	unknown	unknown	unknown	2062
HD 82943	unknown	43	27.6	6.54	5874	493	unknown	614
HD 215456	unknown	unknown	38.0	6.63	unknown	unknown	unknown	unknown
14 Herculis	373	89	17.5	6.67	5311	546	77.8	326
HD 134606	unknown	12	26.7	6.85	unknown	unknown	unknown	2199
HD 40307	517	14	12.9	7.17	4977	582	59.8	2207
HD 177830	unknown	18	59.2	7.18	4948	586	unknown	1724
HD 141399	unknown	unknown	36.2	7.2	5360	541	unknown	unknown
HD 154857	351	20	64.1	7.25	5445	532	80.4	1409
HD 155358	unknown	20	44.2	7.27	5760	503	unknown	1312
HD 159868	unknown	23	52.7	7.27	5395	537	unknown	1257
HD 10180	287	9	38.9	7.33	5911	490	90.8	2948
HD 12661	293	35	35.0	7.44	5742	505	91.5	759
HD 31527	unknown	unknown	38.6	7.48	unknown	unknown	unknown	unknown
HD 93385	257	4	42.3	7.49	unknown	unknown	unknown	unknown
HD 128311	410	83	16.6	7.51	4965	584	75.6	373
HD 13908	unknown	unknown	71.1	7.51	6255	463	unknown	unknown
HD 11506	248	27	51.8	7.54	6058	478	103	933
83 Leonis	977	37	18.1	7.57	4875	594	32.3	859
HD 74156	237	29	64.4	7.61	6039	480	108	870
HD 37124	226	25	33.7	7.68	5606	517	121	1115
HD 47186	unknown	17	39.6	7.79	5675	511	unknown	1628
HD 187123	unknown	24	48.1	7.83	5714	507	unknown	1101
HD 183263	204	26	55.2	7.86	5888	492	128	1010
HD 21693	unknown	unknown	32.2	7.94	unknown	unknown	unknown	unknown
HD 65216	unknown	29	34.3	7.98	5666	511	unknown	936
HD 204313	unknown	30	47.2	7.99	5767	502	unknown	884

TABLE II: Parameters of some brightest stars that are known to have a planet, potentially suitable for intensity interferometry observations.

Alternatively to stars, quasars can also be used as light sources. The advantage of quasars is their great distance from us (billions of light years) which increases the chance of occultation with a dark object. In fact quasars have produced the most spectacular gravitational lensing images even with conventional observation techniques. The disadvantage is their low photon flux. The brightest known quasar, 3C 273, has apparent visible brightness of

only 12.9. Another potential disadvantage of quasars is that their radiation has strongly non-thermal nature, and the presence and degree of thermal photon bunching, providing the physical background for intensity interferometry, yet needs to be established.

From the above examples we see that different types of source-object systems will have its own set of key parameters (such as the source photon flux and its attenuation by the object, the transient time, the source speckle size, spectral parameters, and others) that may vary dramatically from system to system. Therefore each case will require a separate feasibility study under its own specific constraints, such as allowed observation time, required detectors array size, timing accuracy, observation wavelength and so on.

To summarize this Section, we would like to emphasize that the optical imaging in astronomy will remain an active area of NASA's deep space exploration efforts for many years to come. Developing a novel technology geared to provide new or enhanced data will definitely have a high impact. Potential benefits of our approach will include new capabilities for enhanced resolution, which is determined by a large baseline between the two detectors, in a way similar to the synthetic aperture approach. These benefits will also include the capability for faint object detection, and broader range imaging of extra-terrestrial objects, such as Earth-like planets (including those near bright stars), black holes, dust or gas clouds, and possibly dark matter. We envision the emergence of new research programs and space missions enabled by the technology we currently develop. The ramifications of our research may extend beyond the scope of astronomy and astrophysics. Ghost imaging of remote objects or of objects with limited access attracts increasing attention from the military and national security agencies.

II. PHASE I GOALS AND ACCOMPLISHMENTS

The Phase I primary objective has been to evaluate the feasibility of our approach at a conceptual level. We investigated the possibility of performing the thermal-light Ghost imaging without the optical beam splitter, which has been indispensable in all prior realizations. In our approach the object itself plays the role of the beam splitter by creating coherence between the detectors in a way that imprints the object's optical properties onto the measured intensity correlation function. If proved viable, this approach will allow for practical application of the correlation imaging technique, in particular for astronomy observations.

While the earlier study of ghost imaging provided solid theoretical base for the underlying approach, a thorough feasibility study is required prior to launching a large-scale mission-focused effort. The main goal of the one-year-long Phase I has been to carry out such a study and present the recommendations for the Phase II, as to whether such an effort would be practical at the present or future level of technology. Three key questions to be answered by the Phase I research have been the following:

1. Is the proposed approach feasible at the fundamental level?
2. What are the advantages or value added to the conventional approaches?
3. What would a possible future mission look like?

To achieve the Phase I goals we carried out the theoretical analysis of the base ghost imaging configuration as shown in Fig. 4(b). This configuration choice entailed a more complicated analysis and less favorable object observability, compared to the configuration of Fig. 4(a). However the considerations of mission feasibility have prevailed and determined our configuration choice as a conceptual example of the potential mission architecture.

The analysis carried for the selected configuration has yielded the positive answer to the first Phase I question. This analysis has been further used to provide the theoretical estimates of the technique's expected performance with respect to astronomical objects of interest. Based on these estimates, we discuss the practical aspects of ghost imaging in space, such as the signal-to-noise ratio (SNR), optical bandwidth, clock synchronization requirements, and others, to evaluate the advantages or establish the added benefits of the correlation imaging technique. The account of Phase I research has been condensed into list of benchmarks summarized below with a brief discussion of the accomplishments.

A. Introducing the theoretical model

In this Section we present our fundamental analysis using a simple model object and carried out in paraxial planar geometry. We consider a flat source and a flat object placed in the source and object planes, respectively. In these planes we introduce the local transverse coordinates $\vec{\rho}$ for the source and $\vec{\rho}_o$ for the object. We designate L_s as the distance between the source and object planes, and $L_{1,2}$ as the distances between the object plane and the

planes of point-like detectors 1 and 2. The local transverse positions of these detectors are denoted as $\vec{\rho}_1$ and $\vec{\rho}_2$, respectively, as shown in Fig. 10.

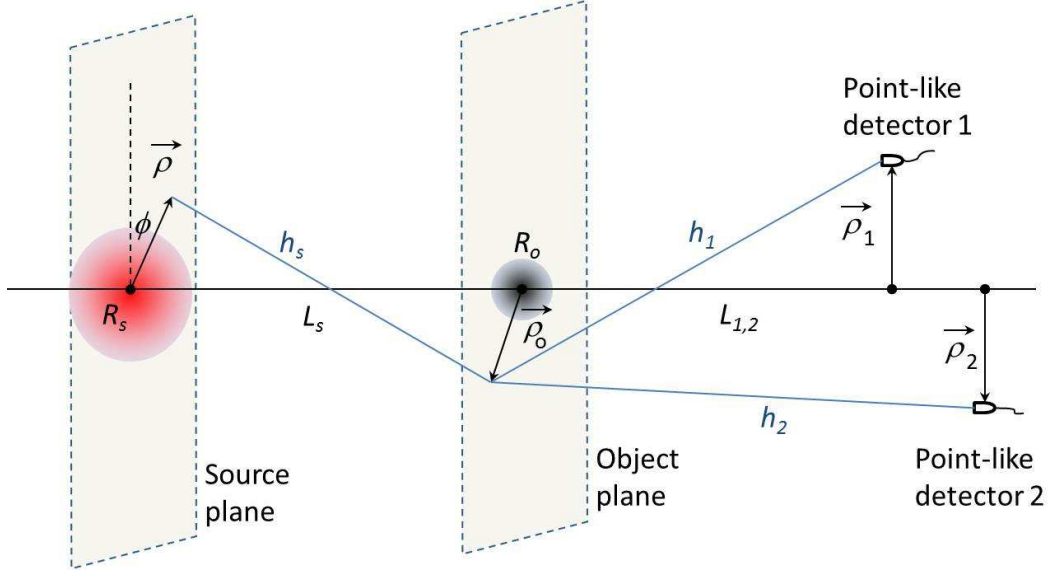


FIG. 10: Relative position of the source, object and detectors in the flat paraxial model.

Let us assume that the source field is bound by a Gaussian envelope with the width R_s and can be written as $E(\vec{\rho}, t) e^{-\frac{\rho^2}{2R_s^2}}$. This model approximates the source with a diameter (intensity distribution FWHM) equal to $\sqrt{2}R_s$. In paraxial approximation, the field at detector 1 is related to the field of the source as

$$E_1(\vec{\rho}_1, t) = \iint d^2\rho d^2\rho_o e^{-\frac{\rho^2}{2R_s^2}} E(\vec{\rho}, t - \frac{L_1 + L_s}{c}) h_{L_s}(\vec{\rho} - \vec{\rho}_o) T(\vec{\rho}_o) h_{L_1}(\vec{\rho}_o - \vec{\rho}_1), \quad (3)$$

Although it looks complicated, expression (3) is actually quite straightforward. It uses the paraxial approximation for the optical field propagation function

$$h_Z(\vec{x}) = \frac{e^{ikZ}}{i\lambda Z} e^{ik\frac{|\vec{x}|^2}{2Z}} \quad (4)$$

that relates the electric field at two spatial points separated by a distance Z along the line of sight and by a transverse displacement \vec{x} (assuming that $x \ll Z$ for the paraxial approximation) in the transverse directions. A field produced by an extended source in a remote point is then given by a convolution of (4) with the source's own field distribution. This procedure yields the field distribution across the object. We then multiply this field by the object's *field transmission function* $T(\vec{\rho}_o)$ which may be real (for a purely absorbing object), imaginary (for a purely phase object, e.g. a thin lens), or complex. Then we repeat

the propagation and integration steps to obtain expression (3) for the field at the detector. A relation similar to (3) can be written for the field at the other detector.

Let us consider the intensity correlation observable

$$\langle I_1(\vec{\rho}_1, t_1) I_2(\vec{\rho}_2, t_2) \rangle = \langle E_1^\dagger(\vec{\rho}_1, t_1) E_2^\dagger(\vec{\rho}_2, t_2) E_1(\vec{\rho}_1, t_1) E_2(\vec{\rho}_2, t_2) \rangle. \quad (5)$$

For thermal light, the phase-sensitive term in (5) vanishes [41], and we arrive at

$$\langle I_1(\vec{\rho}_1, t_1) I_2(\vec{\rho}_2, t_2) \rangle = |\langle E_1^\dagger(\vec{\rho}_1, t_1) E_2(\vec{\rho}_2, t_2) \rangle|^2 + \langle |E_1(\vec{\rho}_1, t_1)|^2 \rangle \langle |E_2(\vec{\rho}_2, t_2)|^2 \rangle, \quad (6)$$

where the first term describes the possible ghost image and the second term gives the uncorrelated “background” intensity product, which also describes the object’s shadow. To separate these effects it is convenient to introduce the normalized Glauber correlation function [42]

$$g^{(2)}(\vec{\rho}_1, t_1; \vec{\rho}_2, t_2) = 1 + \frac{|\langle E_1^\dagger(\vec{\rho}_1, t_1) E_2(\vec{\rho}_2, t_2) \rangle|^2}{\langle |E_1(\vec{\rho}_1, t_1)|^2 \rangle \langle |E_2(\vec{\rho}_2, t_2)|^2 \rangle} = 1 + \frac{|G_{12}|^2}{G_{11} G_{22}}. \quad (7)$$

It is also convenient to consider $|G_{12}|^2$ as an observable, which can be accessed by measuring a correlation of the detector’s photocurrents fluctuations. Indeed, let us assume that the detection is performed by two pinhole photo detectors that have equal sensitive areas A_d and quantum efficiencies η and are located at $\vec{\rho}_1$ and $\vec{\rho}_2$ of the $z = L + L_s$ plane. We also assume that the detectors are small enough to neglect the field variation across A_d . The stochastic photocurrents generated by these detectors in response to the incident field $E_d(\vec{\rho}, t)$ (here $d = 1, 2$) have the following first-order conditional moments normalized to photoelectrons/s:

$$\langle i_d(t) | E_d(\vec{\rho}_d, t) \rangle = \eta A_d \int d\tau |E_d(\vec{\rho}_d, \tau)|^2 h(t - \tau). \quad (8)$$

In Eq. (8) $h(t)$ is the detectors baseband impulse response, which includes any filtering that occurs prior to the correlation measurement. In order to eliminate a featureless background, it may be convenient to assume that a DC blocking filter is included in $h(t)$, such that $\int dt h(t) = 0$.

The blocked DC photocurrent component provides information regarding the total photon flux blocked by the object, which is at the heart of the photon flux based detection methodology, such as used e.g. in the Kepler planetary detection mission. Kepler tracks slow intensity variations of a star to detect Earth-sized exoplanets orbiting the star and to

estimate their orbital characteristics. We tailor our analysis to obtain the *additional* information that can be gathered via the intensity correlation technique, in a way that does not preclude the observer from also using the mean photon flux registered by each detector.

Correlation between the intensity fluctuations observed by the two detectors located at $\vec{\rho}_1$ and $\vec{\rho}_2$ is measured by multiplying the two photocurrents and time-averaging the product:

$$C(\vec{\rho}_1, \vec{\rho}_2) \equiv T^{-1} \int_{-T/2}^{T/2} dt i_1(t) i_2(t), \quad (9)$$

where T is the multiplication circuit integration time, or the “coincidence window” if photon counting technique is used. The stationary photocurrents correlation measurement converges to a time-independent ensemble average, given by

$$\langle C(\vec{\rho}_1, \vec{\rho}_2) \rangle = \mathcal{C} |\langle E_1^*(\vec{\rho}_1) E_2(\vec{\rho}_2) \rangle|^2 = \mathcal{C} |G_{12}|^2, \quad (10)$$

where $\mathcal{C} \equiv \eta^2 A_d^2 [|\Gamma(t)|^2 \star h(t) \star h(-t)]$, and \star denotes convolution. $\Gamma(t)$ is a δ -like function whose width corresponds to the optical coherence time. The latter may be determined by the spectral filters bandwidth. For a narrow-band source, such that $\Gamma(t)$ is much broader than $h(t)$, the parameter \mathcal{C} can be interpreted as a detection volume. For a broad-band source this value is reduced proportionally to the square of the $h(t)$ and $\Gamma(t)$ widths ratio, that is, to the number M of detected longitudinal modes. This is consistent with a well-known result for Glauber correlation function for a multimode thermal light: $g^{(2)}(0) = 1 + 1/M$.

Glauber correlation function will be our main observable in the following analysis. However, let us mention that other types of measurements are possible. In particular, one can measure higher-order correlation functions $g^{(m,n)}$ [43–45], the variance of intensities *difference* (instead of a product) [46–48], or even a multi-detector correlation [49, 50]. The analysis based on the field propagation equation (3) can be easily extended to these types of measurements. Such measurements will have different dependencies on the optical mode structure and on the detector’s quantum efficiencies, and may offer interesting resolution/SNR trade-off opportunities. The possibility of utilizing these measurement strategies distinguishes our approach from the conventional intensity interferometry.

Let us now substitute the fields $E_1(\vec{\rho}_1, t_1)$ and $E_2(\vec{\rho}_2, t_2)$ given by (3) into (7) and take into account the correlation property of thermal field $E(\vec{\rho}, t)$:

$$\langle E^\dagger(\vec{\rho}, t) E(\vec{\rho}', t') \rangle \propto \delta(\vec{\rho} - \vec{\rho}') \Gamma(t - t'). \quad (11)$$

Unless we are interested in color imaging, using narrow-band filters is undesirable because they reduce the optical power available for the measurement. On the other hand, short coherence time requires compatibly fast optical detectors and intensity-correlation circuitry in order to ensure single longitudinal mode detection. Therefore to carry out a fair comparison between the direct intensity measurement and the correlation measurement, we need to take into account the photon flux reduction due to the spectral filtering required in the latter case. As an example, let us assume a 1 ps timing accuracy and the central wavelength of 1 micron. This accuracy requirement may appear unrealistic, since most of contemporary time-stamp systems have time resolution worse than 50 ps, while the pulse front jitter in commercial photon counting detectors can be as low as 30 ps. However these state of the art figures show strong improving trends. Projecting these trends, it is reasonable to expect a single-digit picosecond time resolution systems available by the time our concept matures.

A 1 ps coherence time corresponds to a 3.3 nm wide spectral band around 1 micron central wavelength. Comparing the optical power detected within this band to the total power radiated by the Sun within the typical sensitivity band of a silicon photo detector (see Fig. 11) we find that for a correlation measurement we have in our disposal 0.5% of the optical power available for a broad-band intensity measurement. This reduces the SNR in a shot-noise limited narrow-band correlation measurement compared to a broad-band intensity measurement.

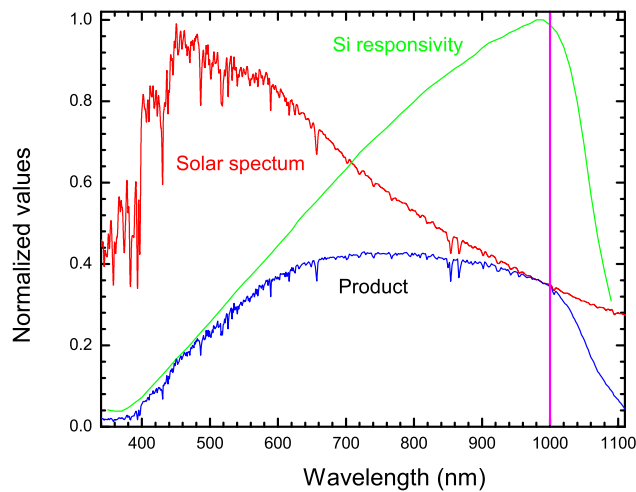


FIG. 11: The solar radiation normalized spectral density (from [51]), spectral sensitivity of a typical silicon photo diode, and their product.

The SNR loss will be less severe for the correlation measurement compared to a *color-resolved* intensity measurement, such as may be used in spectroscopy or Doppler measurements. In particular, no loss may be suffered at all, if one is interested in a very narrow-band measurement, e.g. a measurement with a specific spectral line. A more detailed discussion of the direct-intensity vs. correlation measurement SNRs will be given in Chapter III C reporting the Phase II accomplishments.

Let us point out that in addition to the high speed and low jitter requirements placed on the photo detectors and correlation electronics, a broad-band correlation measurement placed stringent requirements on the clock synchronization between the two detectors, as well as on the accuracy of their relative positioning $L_1 - L_2$ along the line of sight. Fortunately, recent spectacular breakthrough in the field of ultra-precise clocks (in particular, optical clocks) has created a powerful stimulus for developing adequate time transfer protocols. Synchronization of a pair of stationary clocks down to the required precision is already within reach.

More difficulties would arise in case of space-based observer(s). Then the clock synchronization problem is inseparable from the ranging problem, which, in our example of 1 ps timing accuracy, should be better than 30 microns. This problem also has a solution. As one example, in the recent GRAIL mission Ka-band ranging has allowed for the 10 microns ranging precision [52]. Even more accurate ranging is required and is being developed for the optical VLBI and synthetic aperture applications, such as LISA. We expect to be able to leverage this technology which may be expected to advance even further by the time of the “Ghost imaging of space objects” mission design.

As an alternative, the time synchronization problem can be considerably alleviated if one takes the advantage of the fact that in our approach we always rely on the maximum correlation, that is, zero delay between the photon arrival times. This will allow us to continuously adjust the local clocks so as to maximize the measured correlation function, and to monitor the change of this maximal value. In a sense, this would amount to using the detected signal as a time-synchronization signal, an approach one might call a *stellar GPS*.

To continue our analysis we will assume that perfect synchronization between the detectors has been achieved and $\Gamma(t - t') = 1$ in (11). We then suppress the temporal part of the

problem. For the numerator in (7) we derive

$$G_{12}(\vec{\rho}_1, \vec{\rho}_2) = \int d^2\rho d^2\rho'_o d^2\rho_o e^{-\frac{\rho_o^2}{R_s^2}} T_2(\vec{\rho}_o) T_1^*(\vec{\rho}'_o) h_{L_s}^*(\vec{\rho} - \vec{\rho}'_o) h_{L_s}(\vec{\rho} - \vec{\rho}_o) h_{L_1}^*(\vec{\rho}'_o - \vec{\rho}_1) h_{L_2}(\vec{\rho}_o - \vec{\rho}_2). \quad (12)$$

In (12) we have introduced $T_{1,2}(\vec{\rho}_o)$ to allow the transmission functions to be different for detectors 1 and 2. This will allow us to consider the case when the object (partially) obscures the source light for one detector, and scatters it to the other, therefore addressing the scenario in Fig. 4(a). In this case one detector receives the direct light from the source, while the other only sees the light scattered by the object. In handling such situations we still need to make sure the paraxial approximation holds, and that the approximation of a flat object remains reasonable.

For the following analysis it will be convenient to introduce an aperture-limited propagation function

$$G_{12}^{(R_s)}(Z_a, \vec{\rho}_a; Z_b, \vec{\rho}_b) = \int d^2\rho e^{-\frac{\rho^2}{R_s^2}} h_{Z_a}^*(\vec{\rho} - \vec{\rho}_a) h_{Z_b}(\vec{\rho} - \vec{\rho}_b) \quad (13)$$

for the fields propagating to locations $(Z_a, \vec{\rho}_a)$ and $(Z_b, \vec{\rho}_b)$ from a Gaussian source of thermal light that has a width R_s and is located at $Z = 0$. Equivalently, from the *advanced wave* perspective [53], it describes time-reversed propagation of a photon from $(-Z_a, \vec{\rho}_a)$ to the source, and then forward in time to $(Z_b, \vec{\rho}_b)$. If the source is infinitely large, $R_s \rightarrow \infty$, the aperture-limited propagation function (13) becomes equal to a usual paraxial point-source propagation function from one detector to the other:

$$G_{12}^{(\infty)}(Z_a, \vec{\rho}_a; Z_b, \vec{\rho}_b) = h_{Z_b - Z_a}(\vec{\rho}_b - \vec{\rho}_a). \quad (14)$$

The aperture-limited propagation function arises in (7):

$$G_{12}(\vec{\rho}_1, \vec{\rho}_2) = \int \int d^2\rho_o d^2\rho'_o h_{L_2}(\vec{\rho}_o - \vec{\rho}_2) h_{L_1}^*(\vec{\rho}'_o - \vec{\rho}_1) T_2(\vec{\rho}_o) T_1^*(\vec{\rho}'_o) G_{12}^{(R_s)}(L_s, \vec{\rho}'_o; L_s, \vec{\rho}_o), \quad (15)$$

and likewise for $G_{11}(\vec{\rho}_1)$ and $G_{22}(\vec{\rho}_2)$. To evaluate $G_{12}^{(R_s)}(Z_a, \vec{\rho}_a; Z_b, \vec{\rho}_b)$ in a general form we introduce polar coordinates such that

$$\int d^2\rho = \int_0^\infty \rho d\rho \int_0^{2\pi} d\varphi, \quad |\vec{\rho}_a - \vec{\rho}_b|^2 = \rho_a^2 + \rho_b^2 - 2\rho_a\rho_b \cos(\varphi_a - \varphi_b). \quad (16)$$

The angular integration in Eq. (13) yields

$$\begin{aligned} G_{12}^{(R_s)}(Z_a, \vec{\rho}_a; Z_b, \vec{\rho}_b) &= 2\pi \frac{e^{ik(Z_b - Z_a)}}{\lambda^2 Z_a Z_b} e^{i\frac{k}{2}(\rho_b^2/Z_b - \rho_a^2/Z_a)} \\ &\times \int_0^\infty \rho d\rho e^{-\rho^2 \left[\frac{1}{R_s^2} + ik \frac{Z_b - Z_a}{2Z_a Z_b} \right]} J_0 \left(k\rho \left| \frac{\vec{\rho}_b}{Z_b} - \frac{\vec{\rho}_a}{Z_a} \right| \right). \end{aligned} \quad (17)$$

Then integrating over the radius we obtain

$$G_{12}^{(R_s)}(Z_a, \vec{\rho}_a; Z_b, \vec{\rho}_b) = 2\pi \frac{R_s^2}{\lambda^2} \frac{e^{ik(Z_b-Z_a)}}{2Z_a Z_b + ikR_s^2(Z_b - Z_a)} \quad (18)$$

$$\times e^{i\frac{k}{2}(\rho_b^2/Z_b - \rho_a^2/Z_a)} e^{-\frac{k^2}{2} \left| \frac{\vec{\rho}_b}{Z_b} - \frac{\vec{\rho}_a}{Z_a} \right|^2 \frac{R_s^2 Z_a Z_b}{2Z_a Z_b + ikR_s^2(Z_b - Z_a)}}.$$

In the case of interest (15) we have $Z_a = Z_b = L_s$, which leads to

$$G_{12}^{(R_s)}(L_s, \vec{\rho}'_o; L_s, \vec{\rho}_o) = q^2 \pi^{-1} e^{i\frac{q}{R_s}(\rho_o^2 - \rho_o'^2)} e^{-q^2 |\vec{\rho}_o - \vec{\rho}_o'|^2}, \quad (19)$$

where $q^{-1} = 2L_s/(kR_s)$ is the Gaussian width of the correlation function for a source that has Gaussian field distribution introduced above. This value also represents the FWHM of a Gaussian source speckle.

Let us discuss another source of practical significance: a uniform disk. In order to match the total source luminosity, the disk radius has to be $\sqrt{2}R_s$, as has been discussed above. This case can be analyzed by changing Eq. (18) into the form

$$G_{12}^{[\sqrt{2}R_s]}(Z_a, \vec{\rho}_a; Z_b, \vec{\rho}_b) = 2\pi \frac{e^{ik(Z_b-Z_a)}}{\lambda^2 Z_a Z_b} e^{i\frac{k}{2}(\rho_b^2/Z_b - \rho_a^2/Z_a)} \quad (20)$$

$$\times \int_0^{\sqrt{2}R_s} \rho d\rho e^{-ik\rho^2 \frac{Z_b - Z_a}{2Z_a Z_b}} J_0 \left(k\rho \left| \frac{\vec{\rho}_b}{Z_b} - \frac{\vec{\rho}_a}{Z_a} \right| \right).$$

For $Z_a = Z_b = L_s$ this yields

$$G_{12}^{[\sqrt{2}R_s]}(L_s, \vec{\rho}'_o; L_s, \vec{\rho}_o) = q^2 \pi^{-1} e^{i\frac{q}{R_s}(\rho_o^2 - \rho_o'^2)} \frac{J_1(2\sqrt{2}q|\vec{\rho}_o - \vec{\rho}_o'|)}{\sqrt{2}q|\vec{\rho}_o - \vec{\rho}_o'|}. \quad (21)$$

This expression has been used to derive (1).

The correlation observables (i.e., speckle shapes) for a Gaussian and disk sources calculated according to Eqs. (18) and (21), respectively, are shown in Fig. 12. We see that they are very close, which means that the Gaussian source model provides a surprisingly good approximation of realistic sources of thermal light in space. We will continue to use it for the rest of this section. We will also limit the discussion to a special balanced case when $L_1 = L_2 = L$. While this case limits possible observation scenario, it allows us to carry out exact analytical calculations in many cases of interest, and to evaluate the practical utility of our approach.

To carry out the further calculation it will be convenient to introduce new coordinates: $\vec{x} = (\vec{\rho}_o + \vec{\rho}_o')/\sqrt{2}$ and $\vec{y} = (\vec{\rho}_o - \vec{\rho}_o')/\sqrt{2}$. Then substituting (19) into (15) we obtain

$$G_{12}(\vec{\rho}_1, \vec{\rho}_2) = A \int \int S(\vec{x}, \vec{y}) e^{-2q^2 y^2} e^{i\vec{\Delta}\vec{x}} e^{i\vec{\Sigma}\vec{y}} e^{i\gamma\vec{x}\vec{y}} d^2x d^2y, \quad (22)$$

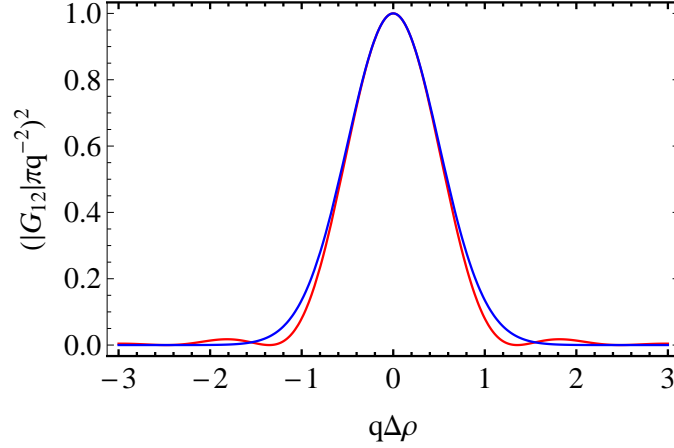


FIG. 12: The speckle shapes (intensity correlation observables) for a Gaussian and disk sources of equal luminosity are given by the blue and red curves, respectively.

where

$$\begin{aligned}
 A &= \pi \left(\frac{R_s}{\lambda^2 L L_s} \right)^2 e^{\frac{ik}{2L}(\rho_2^2 - \rho_1^2)}, \\
 S(\vec{x}, \vec{y}) &= T_2\left(\frac{\vec{x} + \vec{y}}{\sqrt{2}}\right) T_1^*\left(\frac{\vec{x} - \vec{y}}{\sqrt{2}}\right), \\
 \vec{\Delta} &= \frac{k}{\sqrt{2}L}(\vec{\rho}_1 - \vec{\rho}_2), \\
 \vec{\Sigma} &= \frac{k}{\sqrt{2}L}(\vec{\rho}_1 + \vec{\rho}_2), \\
 \gamma &= k(1/L + 1/L_s).
 \end{aligned} \tag{23}$$

The Gaussian term in (22) arises from Fourier transform of the source field distribution. This suggests that (22) could be generalized for any such distribution, which is then to be treated numerically. This approach will be explored in the framework of the Phase II research program. At this stage we will limit our consideration to a Gaussian source.

As a sanity check, let us notice that if we “turn off” the object by setting $S(\vec{x}, \vec{y}) = 1$, the integral over d^2x in (22) yields $(2\pi)^2\delta(\vec{\Delta} + \gamma\vec{y})$. Then the d^2y integral yields, quite expectedly, the correlation function of a Gaussian source (19) with increased free-space propagation length $L_s \rightarrow L + L_s$:

$$G_{12}(\vec{\rho}_1, \vec{\rho}_2) \rightarrow G_{12}^{(R_s)}(L + L_s, \vec{\rho}_1; L + L_s, \vec{\rho}_2). \tag{24}$$

Let us now consider a few example objects and discuss their possible relevance for the astronomy applications.

B. A Gaussian absorber

Let us consider an object that has a Gaussian absorption profile. This case can approximate e.g. a spherical dust or gas cloud of roughly uniform density. It also can be used as a crude model for a planetary occultation of a star. The transmission function of such an object can be modeled as

$$T(\vec{\rho}_o) = 1 - T_0 e^{-\frac{\rho_o^2}{2R_o^2}}, \quad (25)$$

which gives rise to four terms:

$$S(\vec{x}, \vec{y}) = S_0 + S_{1a} + S_{1b} + S_2 = 1 - T_0 e^{-\frac{(\vec{x}+\vec{y})^2}{4R_o^2}} - T_0 e^{-\frac{(\vec{x}-\vec{y})^2}{4R_o^2}} + T_0^2 e^{-\frac{x^2+y^2}{2R_o^2}}. \quad (26)$$

In (25) and (26) T_0 is the amplitude transmission of the most opaque (central) part of the object. Consequently, the correlation function also will consist of four terms: $G_{12} = G_{12}^{(0)} + G_{12}^{(1a)} + G_{12}^{(1b)} + G_{12}^{(2)}$, where the zero-order term corresponds to free-space propagation (24): $G_{12}^{(0)} = G_{12}^{(R_s)}(L + L_s, \vec{\rho}_1; L + L_s, \vec{\rho}_2)$. A straightforward but cumbersome calculation leads to the following expression for both the first- and the second-order terms:

$$G_{12}^{(1,2)}(\vec{\rho}_1, \vec{\rho}_2) = \frac{(-T_0)^n}{\pi(\tilde{q}^2 + R_o^2 \tilde{\gamma}^2)} \left(\frac{k^2 R_s R_o}{2LL_s} \right)^2 e^{-i \frac{k^2 R_o^2 \tilde{\gamma}}{2L^2} \frac{\rho_2^2 - \rho_1^2}{\tilde{q}^2 + R_o^2 \tilde{\gamma}^2}} e^{-\frac{k^2 (\vec{\rho}_2 + \vec{\rho}_1)^2}{8L^2 (\tilde{q}^2 + R_o^2 \tilde{\gamma}^2)}} e^{-\frac{k^2 R_o^2 \tilde{q}^2}{2L^2} \frac{(\vec{\rho}_2 - \vec{\rho}_1)^2}{\tilde{q}^2 + R_o^2 \tilde{\gamma}^2}}. \quad (27)$$

To obtain $G_{12}^{(1a,b)}$, we need to substitute in (27)

$$n = 1, \quad \tilde{q}^2 = 2q^2 + \frac{1}{4R_o^2}, \quad \tilde{\gamma} = \gamma \pm \frac{i}{2R_o^2}.$$

For $G_{12}^{(2)}$, we substitute

$$n = 2, \quad \tilde{q}^2 = 2q^2 + \frac{1}{2R_o^2}, \quad \tilde{\gamma} = \gamma.$$

We notice that in the multi-mode case when the speckle size on the object greatly exceeds the object size $\tilde{q}^2 \approx 2q^2$. This situation is to be expected for most of source-object systems in space, however we do not need to make this approximation now.

Let us investigate the result (27) for a set of parameters that can be easily implemented on an optical table. In Fig. 13 we show a correlation function $g^{(2)}(\vec{\rho}_1 = -\vec{\rho}_2)$ and the intensity profile featuring the object's shadow. In this simulation an opaque ($T_0 = 1$) object is placed between a source with $R_s = 1$ cm and the detectors plane so that $L_s = L = 50$ cm. The object size R_o is varied from zero to 1, 2 and 3 mm. As the object becomes larger its shadow becomes deeper and, less intuitively, the speckle size becomes smaller. For larger objects the speckle shape also becomes distorted.

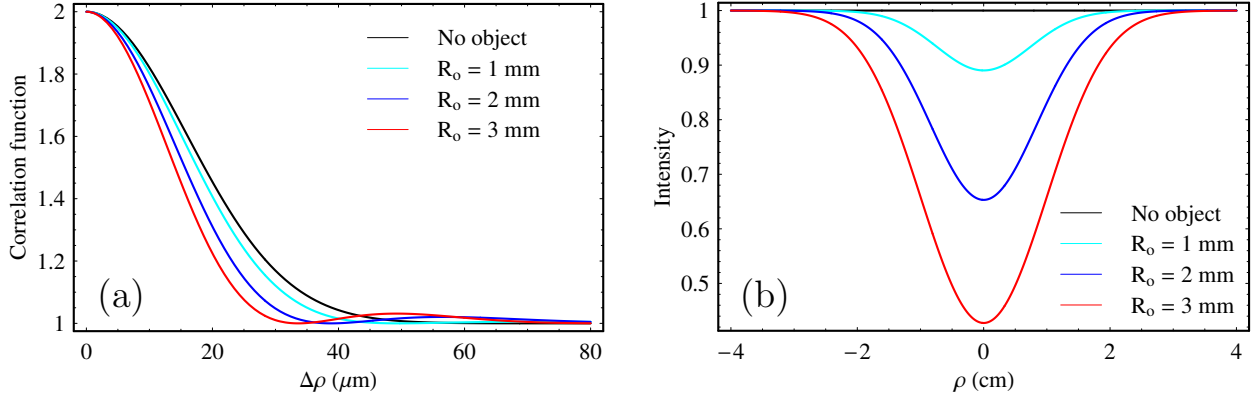


FIG. 13: The correlation function $g^{(2)}(\vec{\rho}_1, \vec{\rho}_2)$ vs. the distance $\Delta\rho = |\vec{\rho}_1 - \vec{\rho}_2|$ (a) and the intensity profile (b) for a lab parameter set $T_0 = 1$, $L_s = L = 50$ cm and $R_s = 1$ cm. The object size R_o is varied from zero to 1, 2 and 3 mm.

Even less intuitive evolution is undergone by the speckle size (the FWHM) as the object is moved across the line of sight, imitating a planet passing across the star. To simulate this transient we actually changed the detector's position $\rho_s = (\rho_1 + \rho_2)/2$ while the $R_o = 1$ mm object was fixed on the initial line of sight at $L_s = L = 50$ cm. The effective displacement of the object from the line of sight was then found as $\rho_o = \rho_s L_s / (L + L_s)$.

The speckle size evolution is shown in Fig. 14(a) for two cases: when the object is displaced along the line connecting the detectors $\vec{\rho}_1 - \vec{\rho}_2$ (red curve), and when it is displaced in the perpendicular direction (blue curve). The corresponding variation of the detected photon flux is shown in Fig. 14(b). The photon flux reaches the minimum when the object is exactly on the line of sight and does not depend on the displacement direction, as one could expect from the symmetry considerations.

The speckle width, on the other hand, strongly depends on the displacement orientation. This implies that unlike the direct intensity measurement, the correlation (speckle width) measurement has a *stereoscopic character*. Remarkably, the fractional variation of both types of observables due to the transient object is approximately 7%, see Fig. 14. In the framework of the Phase II research we will prove that this is not a coincidence but a rather general feature of the correlation measurement technique: the object signature present in the speckle-width measurement has the same relative magnitude as the one present in the direct intensity measurement. Of course, to compare the efficiencies of these two types of observations one also need to compare the measurements SNR. Analysis carried out in the

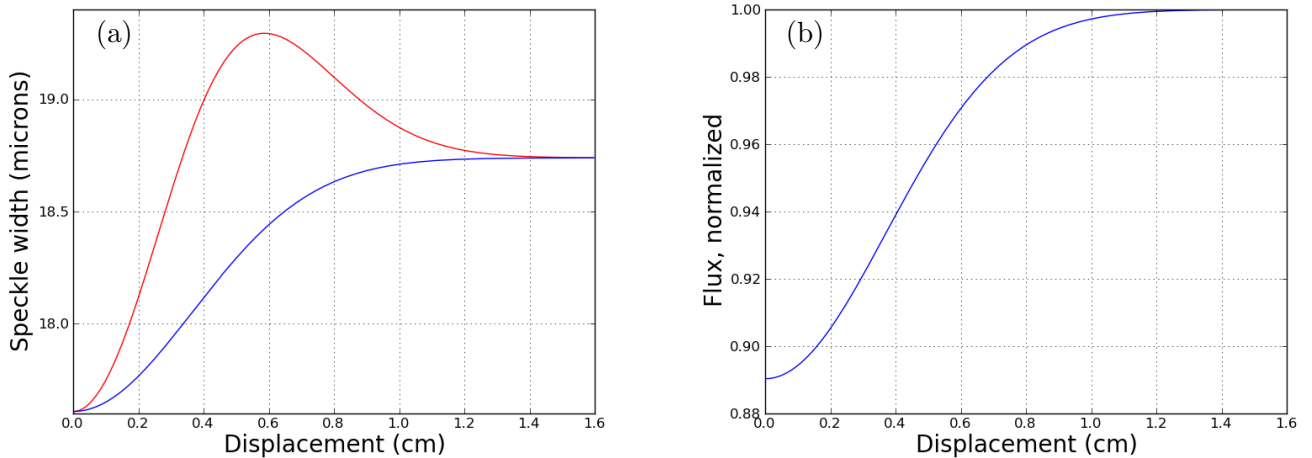


FIG. 14: (a) Speckle width as a function of the objects displacement in the direction $\vec{\rho}_1 - \vec{\rho}_2$ of the detectors' baseline (red) and in the perpendicular direction (blue). (b) Normalized photon flux corresponding to the cases from (a). The parameter set is $T_0 = 1$, $L_s = L = 50$ cm, $R_s = 1$ cm, $R_o = 1$ mm.

framework of Phase II research has shown that in this sense the correlation measurement technique is at a strong disadvantage. However, as has already been mentioned, our goal is not to compete with intensity-based observations, but to upgrade such observations with new capabilities. Such a possibility is suggested by the stereoscopic character of the speckle-width measurement shown in Fig. 14(a). Full understanding of this phenomenon has been gained in the Phase II research. This understanding has lead to the realization how not only the orbital displacement but also full 2D imaging of a dark space object is possible. We will discuss this breakthrough in the following chapters.

Let us now apply our model to an actual astronomical observation carried out by Kepler space telescope [1, 2]. Substituting the Kepler-20f parameters [2] into our model we find the relative intensity variation of the order of 10^{-4} , which is consistent with the actual observation [2], see Fig. 15. In line with the earlier discussion, we use the actual planet radius times $\sqrt{2}$ as R_o in our simulations. The discrepancy in the dip shape clearly visible in Fig. 15 arises from using the Gaussian source and absorber model while the actual star and planet are, of course, better described as disks. However the numerical agreement with the experiment shows that even a simplistic fully analytical Gaussian model can be useful.

This has encouraged us to carry out the speckle-width measurement simulation for the

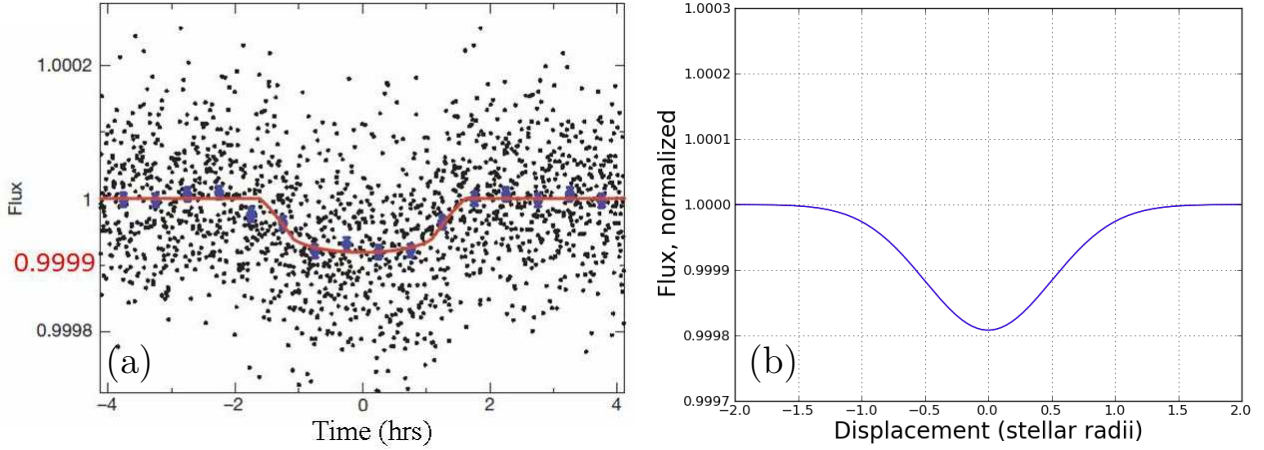


FIG. 15: The intensity variation for Kepler-20e observed in [2] (a), and computed based on our model (b).

Kepler-20f. The results of these simulations are shown in Fig. 16. As expected, the character of the transient observable strongly depends on the orbit plane orientation relative to the detectors' baseline. Again, the magnitude of the speckle width variation, from 3,603.6 m to 3,604.2 m, or 1.7×10^{-4} fractional change, is very close to the magnitude of the photon flux variation shown in Fig. 15. We view this result as very encouraging and justifying the Phase II research effort.

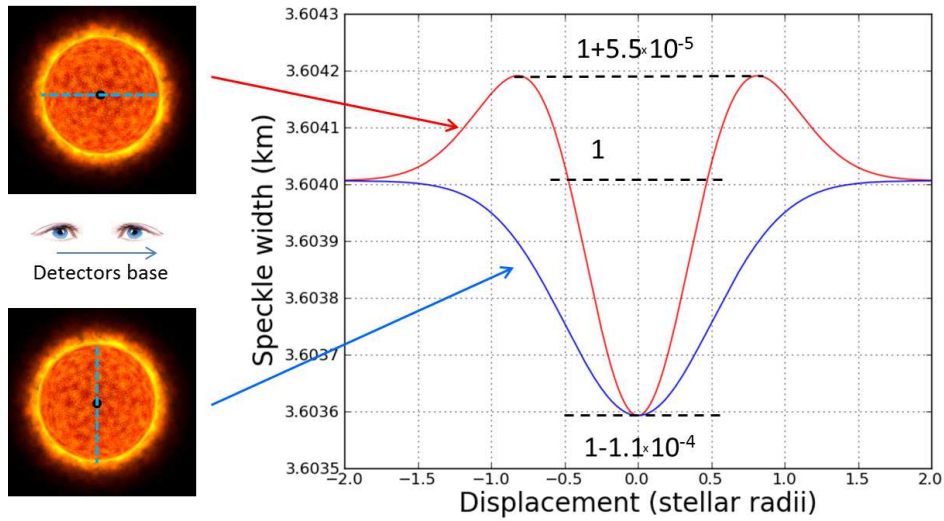


FIG. 16: The predicted speckle width variation for Kepler-20e depends on the relative orientation of the detectors' baseline and the planet's orbit.

C. Unbalanced arms configuration

So far we have assumed that both detectors are located in a plane perpendicular to the line of sight. Therefore, within the paraxial approximation, they are equidistant from the object: $L_1 = L_2$. This assumption makes the measurement of the Glauber correlation function equivalent to measuring the shape of the speckle. But this need not be the case. In this section we consider a more general situation when $L_1 \neq L_2$ which may be realized in asymmetric configurations, e.g. when the correlation measurement is performed by a ground-based detector jointly with a distant space-based detector, as in Fig. 4(a). Importantly, we will continue to assume perfect time synchronization between the two detectors, which in the asymmetric case can be achieved with an appropriate time delay. Therefore all the effects we will observe are going to be of spatial (transverse) rather of temporal (longitudinal) nature. It will not be possible to carry out the analytical calculations without making further approximations. From (19) we see that the *large aperture approximation* (14) holds when

$$\alpha_s \equiv \frac{2Z_a Z_b}{kR_s^2 |Z_b - Z_a|} \ll 1. \quad (28)$$

This approximation is appropriate for evaluation of the first-order terms in (15) where $Z_b - Z_a = L_1$ is large. Indeed, in this case for the optical table geometry $\lambda = 1 \mu\text{m}$ and $R_s = L_s = 1 \text{ cm}$ we get $\alpha_s = 1.6 \times 10^{-5}$. For the Solar system geometry with $R_s = 7 \times 10^5 \text{ km}$ (Sun radius), $L_s = 1.5 \times 10^8 \text{ km}$ (the distance from Earth to Sun), and $\lambda = 1 \mu\text{m}$, we get $\alpha_s = 5 \times 10^{-14}$. This parameter becomes even smaller for interstellar distances. Therefore when we calculate G_{12} for a Gaussian absorber described by Eq. (25), the first-order terms can be approximated as

$$\begin{aligned} G_{12}^{(1)}(\vec{\rho}_1, \vec{\rho}_2) &\equiv G_{12}^{(1a)}(L_1, \vec{\rho}_1; L_2, \vec{\rho}_2) + G_{12}^{(1b)*}(L_2, \vec{\rho}_2; L_1, \vec{\rho}_1) \\ &\approx -2 \int d^2\rho \, e^{-\frac{\rho^2}{2R_s^2}} h_{L_1}^*(\vec{\rho} - \vec{\rho}_1) h_{L_2}(\vec{\rho} - \vec{\rho}_2). \end{aligned} \quad (29)$$

The opposite case of (28) occurs when $Z_a = Z_b$. If furthermore q^2 is much greater than all coefficients that multiply ρ^2 in all real and imaginary exponents in (15), then (19) can be proven to approach a δ -function normalized to unity. This is the *small aperture approximation*, applicable for the second-order terms of (15). Let us point out that within this approximation, the object cannot create coherence between the transmitted and scattered light unless the speckle size in the object plane approaches or exceeds the size of the object

itself.

For the optical table geometry as described above, q^2 exceeds all relevant parameters by a factor of at least 3×10^4 . The excess factors are much greater in all reasonable astronomical geometries. Therefore we derive

$$G_{12}^{(2)}(\vec{\rho}_1, \vec{\rho}_2) \approx \int d^2\rho \, e^{-\frac{\rho^2}{R_o^2}} h_{L_1}^*(\vec{\rho} - \vec{\rho}_1) h_{L_2}(\vec{\rho} - \vec{\rho}_2). \quad (30)$$

For a Gaussian absorber case with $L_1 \neq L_2$ we then arrive at the following approximate expressions:

$$\begin{aligned} G_{12}^{(0)}(\vec{\rho}_1, \vec{\rho}_2) &= G_{12}^{(R_s)}(L_1 + L_s, \vec{\rho}_1; L_2 + L_s, \vec{\rho}_2), \\ G_{12}^{(1)}(\vec{\rho}_1, \vec{\rho}_2) &= -2G_{12}^{(\sqrt{2}R_o)}(L_1, \vec{\rho}_1; L_2, \vec{\rho}_2), \\ G_{12}^{(2)}(\vec{\rho}_1, \vec{\rho}_2) &= G_{12}^{(R_o)}(L_1, \vec{\rho}_1; L_2, \vec{\rho}_2). \end{aligned} \quad (31)$$

It is easy to see that very similar expressions can be derived for the disk-shaped source and/or object.

Let us first evaluate the correlation function $g^{(2)}$ found by substituting (31) into (7) in the absence of the object, which is formally achieved by setting $R_o = 0$. In Fig. 17(a) we show this function for a typical optics table parameters ($L_1 \approx L_2 = 1$ m, $L_s = 1$ cm, $\lambda = 1$ μ m), while assuming that the detectors are symmetric relative to the line of sight: $\vec{\rho}_1 = -\vec{\rho}_2$. This allows us to use a single scalar parameter ρ , in the same way it was done in Fig. 13 and will be done in the following.

The correlation reduction due to non-zero ΔL is clearly visible. We would like to emphasize again that this is not due to a limited coherence length of the source, but because of its transverse coherence properties. We can interpret this result as follows. By placing the first detector in the plane L_1 we define the speckle pattern in this plane as the transverse mode structure. These speckles may be further considered as mutually incoherent light sources. As light from these sources propagates further, the coherence areas expand as well as overlap. The expansion causes the widening of the correlation function while the overlap causes the contrast reduction due to multimode detection. Using the expression for normalized Glauber correlation function for thermal light $g^{(2)}(0) = 1 + 1/M$ relating it to the number of detected modes M , we can determine that in our example the longitudinal displacement of the detector by $\Delta L = 6$ mm has lead to the number of detected modes $M \approx 3$. Note that this interpretation differs from the speckle pattern behavior that one might observe e.g. on

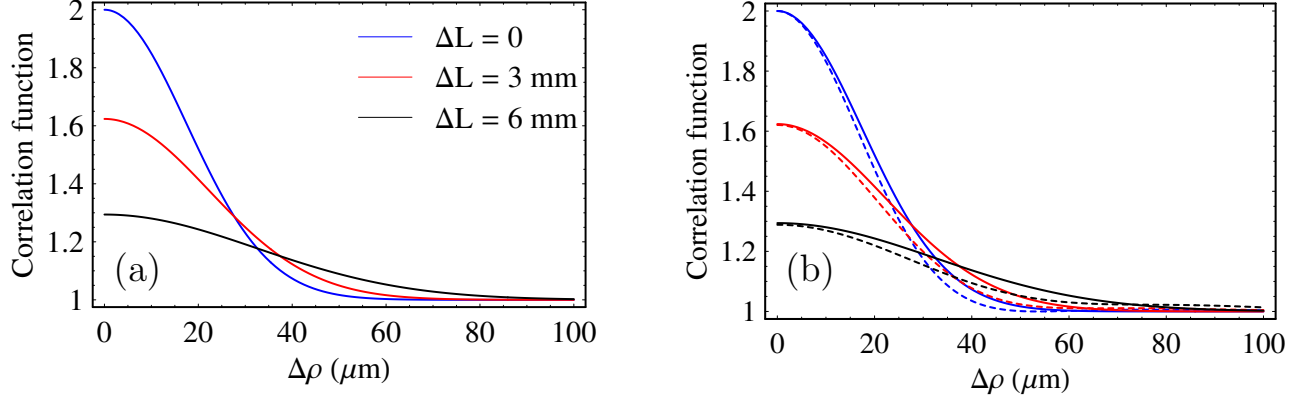


FIG. 17: (a) The correlation functions $g^{(2)}(\Delta\rho)$ in the absence of an object for $R_s = 1$ cm $L_1 = 55$ cm and $L_2 = L_1 + \Delta L$. (b) The same correlation functions (solid lines) become narrower (dashed lines) when a small ($R_o = 1$ mm) Gaussian absorbing object is inserted in the line of sight at the distance $L_s = 55$ cm from the source.

a screen. In this case the speckle do not overlap and do not appreciably change in size for small longitudinal translations.

Now let us “turn on” the object and investigate its effect on the correlation function. If a small ($R_o = 1$ mm) object is placed half way between the source and the detectors, the correlation function becomes narrower, which means smaller speckles, as can be seen in Fig. 17(b). Let us point out that the $\Delta L = 0$ case in Fig. 17(b) is consistent with the $R_o = 1$ mm case from Fig. 13. This agreement validates the large-aperture and small-aperture approximations made in this Section for an absorbing object.

To summarize this Section we notice that the previously made assumption $L_1 = L_2$ indeed provides the best intensity-interferometric observability of the thermal light sources and of dark objects that may obscure such sources. Therefore we will continue using this assumption in the Phase II research.

D. Phase I summary

During our Phase I NIAC research effort we have investigated the possibility of performing the intensity correlation “ghost imaging” of dark objects in space illuminated by thermal light sources (stars) in the background. Our approach hinges on replacing the beam splitter, indispensable for thermal light ghost imaging but infeasible for space applications, with the

object itself. The object size, shape and position are predicted to imprint themselves on the intensity correlation properties of the transmitted light, and could be subsequently extracted from the correlation measurements. To investigate this concept we limited our discussion to fully analytical model relying on a two-dimensional source and an object with Gaussian or uniform (disk-like) distribution of luminosity or absorption, in the paraxial approximation. We demonstrated the variation of the far-field speckle size due to the presence of the object. We have shown that the speckle size variation is a non-trivial function of the object's properties and position. In some cases it allows us to obtain the information not available from a direct intensity-based observation. As an example of such a measurement we have demonstrated how the orbit plane orientation of a transient object can be determined from the intensity-correlation measurements. This understanding has encouraged us to apply our analytical model to a realistic space object imaging scenario, such as observed in the Kepler mission. Prediction for the flux variation following from our model is very close to the actual observation. The model also predicted a similar (about 10^{-4}) fractional variation of the speckle size.

We have carried out a preliminary SNR analysis for a correlation measurement, comparing the SNR expected in such a measurement to the one observed in a direct flux measurement. Our analysis has shown that, for parameters typical of the Kepler mission, the correlation measurement SNR would be significantly worse than the intensity measurement SNR. The situation, however, is expected to improve for narrow-band imaging, e.g. imaging based on a selected spectral line.

To summarize the Phase I results in the context of the key questions posed in the beginning of this chapter, we would like to point out the following.

1. The proposed approach is scientifically sound and conceptually feasible.
2. The proposed approach can be used in conjunction with the conventional observations, providing access to the complementary data, such as e.g. an orbital plane.
3. Either entirely ground-based, or ground/space based mission architectures can be envisioned. We believe that the ground-based mission concept more fully takes the advantage of the intensity interferometry approach being immune to atmospheric distortions.

Based on these conclusions we decided that further research in this direction would be justified. The programatic relations between the Phase I and Phase II NAIC research and

F
E

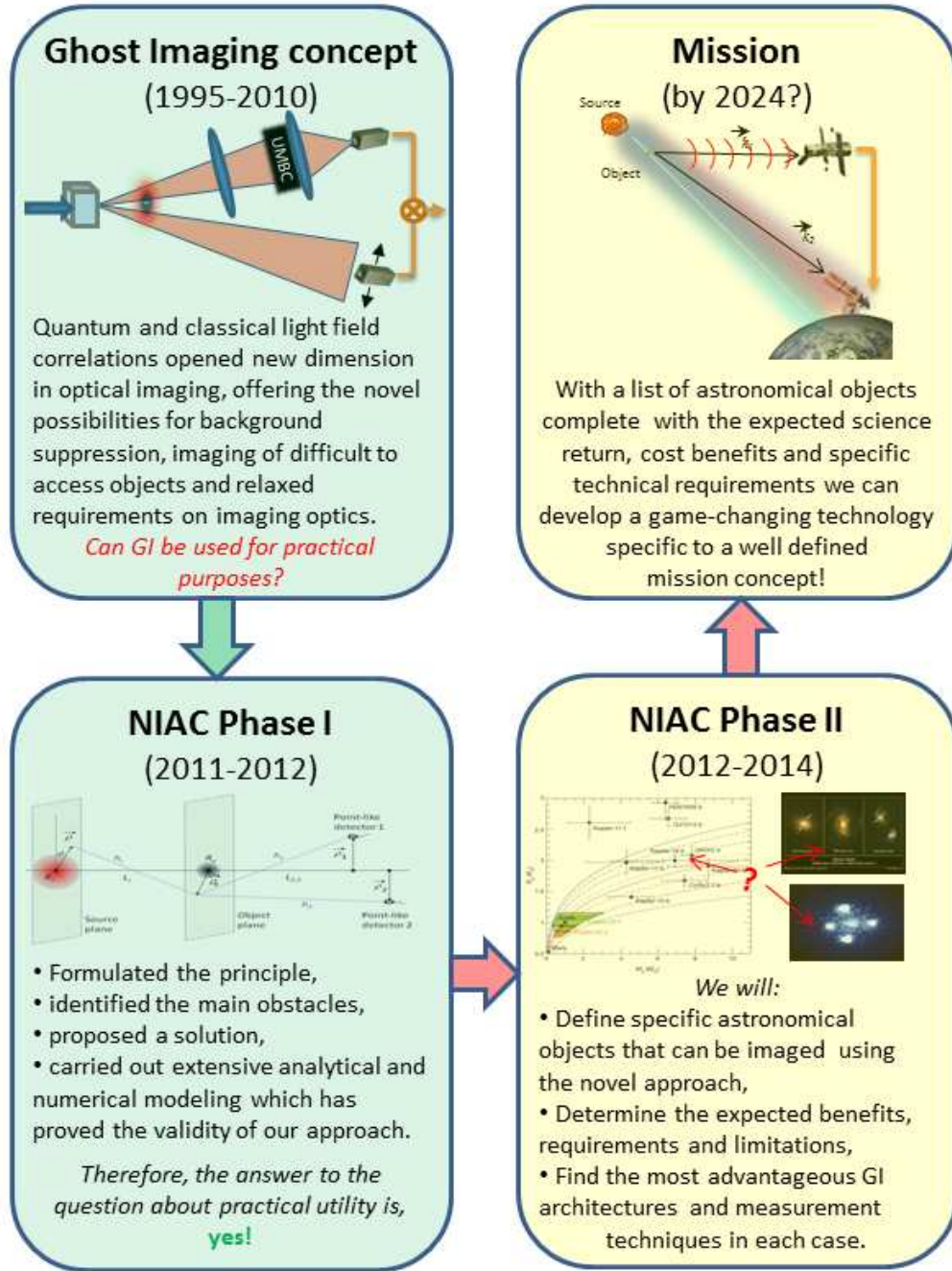


FIG. 18: Our vision of the relations between the underlying Ghost Imaging concept, the results of Phase I research, the Phase II plans, and the future NASA missions.

III. PHASE II GOALS AND ACCOMPLISHMENTS

The main objective of the Phase II research is to advance the intensity interferometric imaging of non-radiating objects towards the level of a viable technology that is ready for mission analysis and design. It should be emphasized that we are not suggesting to replace conventional observation techniques with this technique. Rather, intensity interferometry is envisioned to complement direct observations in such a way that the same detected signal can be utilized for two different processing scenarios: conventional and intensity-interferometric imaging.

Successful completion of the Phase II research would significantly upgrade the conventional optical observation and detection techniques. While the maturity period of the proposed technology is estimated to be of the order of a decade, and the benefiting missions are not yet proposed, much can be learned from reviewing the on-going or near-future missions that could have benefited from this technology. These include the aforementioned Kepler and similar planetary detection missions; Hubble space telescope, aimed to study gravitational lenses among other space objects, as well as other space and ground-based telescopes included into SOFIA program; GALEX and other similar missions. We would not anticipate any conceptual change in an upgraded mission's architecture. Instead, by adding a second observer and implementing a correlation measurement protocol in addition to the standard intensity (photon flux) measurement, we expect to significantly increase the science data return from these missions. Therefore we plan to significantly enhance the future missions scientific return with only an incremental increase of their cost. The additional data will be complementary to the intensity measurement data in that it may provide more information about the object's scattering, absorptive and refractive properties as well as the geometric relations between the object and source sizes and object-source, object-detectors distances.

To facilitate the progress of our research in this direction, the following technical tasks list was suggested for the Phase II:

1. Develop advanced numerical models better approximating the real space objects: opaque disks, randomly scattering objects, phase objects mimicking gravitational lenses.
2. Investigate the potential benefits of using other types of observables (higher-order

correlation functions, intensity difference variance).

3. Carry out a lab demonstration of intensity-correlation imaging of dark objects.
4. Compile a list of astronomical objects that potentially could be observed by intensity-correlation imaging. Supplement this list with observation requirements and constraints specific for each object.
5. Carry out the data rate, SNR, resolution (if applicable), contrast, observation baseline and other fundamental parameters estimates for the selected objects. Verify that application of our approach is indeed practical and beneficial.

The majority of these tasks has been accomplished as reported here. Others, e.g. Tasks 1 and 2, have lead to a new research direction which was deemed more important and potentially more rewarding than the originally planed. As a result, during the Phase II the accent has shifted from *detection* of dark celestial objects and their general characterization towards ground-based, high-resolution intensity interferometric *imaging*. By imaging in this context we understand mapping the column density (in the line-of-sight direction) of the optical absorption for the amplitude objects, or of the phase gradient for the phase objects. This change of the research focus was brought about by an unexpected realization that the object’s shape is encoded in the intensity correlation function, gained during developing of an advanced theoretical model. We then leveraged the knowledge available from “conventional” intensity interferometry to learn how these images can be extracted. The potential benefits of this unforeseen capability were thought to be greater than of the original plan, so the new path was followed.

A. Advanced theoretical analysis

In this analysis we will depart from the Gaussian or disk models for the source and the object, and consider more general distributions of their luminosity and opacity, respectively. To do this we return to our model geometry shown in Fig. 10. We continue using paraxial approximation with the propagation direction denoted as z , and assuming that the source and the object are two-dimensional. We also assume that the detectors are coplanar: $L_1 = L_2 \equiv L$. A departure from the latter assumption has been discussed earlier and concluded

disadvantageous. Let a spatially-incoherent extended source be located at the $z = 0$ plane. For the further analysis we will assume a quasimonochromatic thermal light source with the central wavelength λ . In practice, this implies that narrow bandpass filters have to be used. We denote the scalar positive-frequency component of the source field as $E(\vec{\rho}, t) e^{-i\omega t}$, where $\omega \equiv 2\pi c/\lambda$ is the central frequency, and c is the speed of light in vacuum. The field amplitude is normalized to the square-root of the photon flux.

For spatially-incoherent thermal radiation, $E(\vec{\rho}, t)$ is a Gaussian random function with zero mean value but a nonzero phase-insensitive correlation function given by Eq. (11). A more complete expression for this function is given by [54, 55]:

$$\langle E^*(\vec{\rho}, t_1) E(\vec{\rho}', t_2) \rangle = I_s(\vec{\rho}) \lambda^2 \Gamma(\Delta t) \delta(\vec{\rho}' - \vec{\rho}), \quad (32)$$

where $\Delta t = t_2 - t_1$. In Eq. (32) $\vec{\rho}$ and $\vec{\rho}'$ are two transverse coordinates in the $z = 0$ plane, $I_s(\vec{\rho})$ is the photon flux density in photons per meter-square per second, and $\delta(\vec{\rho})$ is a two-dimensional Dirac delta function. It arises from a delta-function approximation of the spatially-incoherent field's transverse correlation, which is appreciably non-zero only when $|\vec{\rho}' - \vec{\rho}|$ is of the order of a wavelength. We have assumed in Eq. (32) that the correlation function is separable into the product of the spatial and temporal parts, which is generally true for quasimonochromatic thermal light.

Suppose that a dark object with a finite transverse extent is located at $z = L_s$ plane, a distance L_s away from the source. The object modifies the incident field by its transmission function $T(\vec{\rho}_o)$ which generally may be complex, i.e. may affect both phase and amplitude of the incident light. Then, the field emerging from the object plane is given by

$$E_o(\vec{\rho}_o, t) = T(\vec{\rho}_o) \frac{e^{ikL_s}}{i\lambda L_s} \int d^2\rho E(\vec{\rho}, \tau_s) e^{ik\frac{|\vec{\rho}_o - \vec{\rho}|^2}{2L_s}}, \quad (33)$$

where $\tau_s = t - L_s/c$ and the integration is performed over the source plane. Likewise, the field in the detection plane $z = L_s + L$ is given by

$$E_d(\vec{\rho}_d, t) = \frac{e^{ikL}}{i\lambda L} \int d^2\rho E_o(\vec{\rho}, \tau) e^{ik\frac{|\vec{\rho}_d - \vec{\rho}|^2}{2L}}, \quad (34)$$

where $\tau = t - L/c$, the integration is performed over the object plane, and $d = 1, 2$ represents a detector.

As before, let the detections be performed by two pinhole photo detectors that have equal sensitive areas A_d and quantum efficiencies η and are located at $\vec{\rho}_1$ and $\vec{\rho}_2$ of the

$z = L + L_s$ plane. We also assume that the detectors are small enough to neglect the field variation across A_d . The mean photocurrents generated by these detectors in response to the incident fields $E_d(\vec{\rho}, t)$ are given by Eq. (8). The correlation between the intensity fluctuations observed by these two detectors located at $\vec{\rho}_1$ and $\vec{\rho}_2$ is given by Eq. (9), and the correlation observable by Eq. (10).

Deriving (10) we took advantage of the Gaussian moment factoring for the fourth-order moment of the detected fields [54], combined with the assumption that $h_m(t)$ blocks DC. Thus, the correlation signature of interest depends on the phase-insensitive correlation function of the detected fields.

Immediately after the object the coherence has a form

$$\langle E_o^*(\vec{\rho}_1) E_o(\vec{\rho}_2) \rangle = T^*(\vec{\rho}_1) T(\vec{\rho}_2) e^{ik \frac{\vec{\rho}_s \cdot \vec{\rho}_d}{L_s}} K_O(\vec{\rho}_d; L_s), \quad (35)$$

where $\vec{\rho}_s \equiv (\vec{\rho}_1 + \vec{\rho}_2)/2$, $\vec{\rho}_d \equiv \vec{\rho}_2 - \vec{\rho}_1$, and

$$K_O(\vec{\rho}; L) \equiv \frac{1}{L^2} \int d^2 \rho' I_s(\vec{\rho}')^{-ik \vec{\rho} \cdot \vec{\rho}' / L}. \quad (36)$$

To propagate coherence (35) further in the analytical form we need to make the approximations we have avoided in the earlier example of the Gaussian source and object. We note that the Fourier transform relation (36) between I_s and K_O implies that the latter's width is of the order of $\lambda L_s / D_s$, where the source size D_s is defined as the diameter over which the photon-flux density is appreciably greater than zero. This width corresponds to a size of the speckle cast by the source onto the object. In many important cases this speckle size is much smaller than the object features we wish to resolve. Then we can write

$$T^*(\vec{\rho}_1) T(\vec{\rho}_2) \approx |T(\vec{\rho}_s - \vec{\rho}_o)|^2 = 1 - A(\vec{\rho}_s - \vec{\rho}_o), \quad (37)$$

where we have introduced a displacement $\vec{\rho}_o$ of the object's center from the line of sight and converted the *field* transmission T to *intensity* absorption A . Note that in this approximation the phase part of T drops out, so a purely phase object would not alter the coherence propagation within this model.

Approximation (37) notably simplifies our analysis for propagating the coherence to the detector plane. We derive

$$\langle E_d^*(\vec{\rho}_1) E_d(\vec{\rho}_2) \rangle = e^{ik \frac{\vec{\rho}_s \cdot \vec{\rho}_d}{L+L_s}} K_O(\vec{\rho}_d; L + L_s) - K_D(\vec{\rho}_s, \vec{\rho}_d) \quad (38)$$

where the first term represents the source's correlation signature in the absence of any object (i.e., free-space propagation of light over the distance $L + L_s$), and

$$K_D(\vec{\rho}_s, \vec{\rho}_d) \equiv \frac{e^{ik\frac{\vec{\rho}_s \cdot \vec{\rho}_d}{L} - ik\frac{\vec{\rho}_d \cdot \vec{\rho}_o}{L}}}{\lambda^2 L^2} \int d^2\xi A(\vec{\xi}) e^{-ik\frac{\vec{\rho}_d \cdot \vec{\xi}}{L}} \int d^2\zeta K_O(\vec{\zeta}; L_s) e^{ik\frac{L+L_s}{LL_s}(\vec{\rho}_o + \vec{\xi}) \cdot \vec{\zeta}} e^{-ik\frac{\vec{\rho}_s \cdot \vec{\zeta}}{L}} \quad (39)$$

is modification due to the object. Using the convolution theorem we simplify expression to

$$K_D(\vec{\rho}_s, \vec{\rho}_d) = L^{-2} e^{ik\frac{(\vec{\rho}_s - \vec{\rho}_o) \cdot \vec{\rho}_d}{L}} \int d^2\xi I_s \left(\beta(\vec{\rho}_o + \vec{\xi}) - (\beta - 1)\vec{\rho}_s \right) A(\vec{\xi}) e^{-ik\frac{\vec{\rho}_d \cdot \vec{\xi}}{L}}, \quad (40)$$

where $\beta \equiv 1 + L_s/L$.

Without a considerable loss of generality, we can now assume that the detectors are positioned symmetrically about the line of sight, so that $\vec{\rho}_s = 0$. Then, substituting Eq. (40) into Eq. (38), and then substituting the result into Eq. (10), we arrive at

$$C(\vec{q}_d) \approx \frac{\mathcal{C}}{L^4 \beta^4} \left| \mathcal{T}_s \left(\frac{\vec{q}_d}{\beta} \right) - \beta^2 \int d^2\xi I_s \left(\beta(\vec{\rho}_o + \vec{\xi}) \right) A(\vec{\xi}) e^{-i\vec{q}_d \cdot \vec{\xi}} \right|^2, \quad (41)$$

where $\mathcal{T}_s(\vec{q}) \equiv \int d^2\rho I_s(\vec{\rho}) e^{-i\vec{q} \cdot \vec{\rho}}$, and $\vec{q}_d \equiv k\vec{\rho}_d/L$.

To continue the analytical evaluation we have to make our second important approximation, namely

$$\frac{D_o}{D_s} \beta \ll 1. \quad (42)$$

In (42) D_o is the diameter over which the *centered* object's absorption is appreciable. Physically, this means that the angular size of the object (as seen by the observer) is much smaller than the angular size of the source. Let us point out that $\rho_o \beta / D_s \ll 1$ is *not* required, so the approximation (42) is applicable even to small objects that are far away from the line of sight and do not obscure the source. The signal from such objects is of course vanishingly small.

Approximation (42) implies that in the regions where $A(\vec{\xi})$ is non-vanishing, $I_s(\beta(\vec{\rho}_o + \vec{\xi}))$ is nearly constant and therefore can be taken out from the integral:

$$C(\vec{q}_d) \approx \frac{\mathcal{C}}{L^4 \beta^4} \left| \mathcal{T}_s \left(\frac{\vec{q}_d}{\beta} \right) - \beta^2 I_s(\beta \vec{\rho}_o) \mathcal{A}(\vec{q}_d) e^{-i\vec{q}_d \cdot \vec{\rho}_o} \right|^2, \quad (43)$$

where

$$\mathcal{A}(\vec{q}) \equiv \int d^2\rho A(\vec{\rho}) e^{-i\vec{q} \cdot \vec{\rho}}. \quad (44)$$

In Eq. (43) the first term inside the absolute-square is due to the source alone, while the second term is the object-induced modification to the correlation function. It is interesting to

notice that in the absence of an object, $A(\vec{\rho}) \equiv 0$, the result (43) quite expectedly expresses the van CittertZernike theorem. Remarkably, in the absence of the source term, Eq. (43) is reduced to

$$C(\vec{q}_d) \approx \frac{\mathcal{C}I_s(\beta\vec{\rho}_o)}{L^4\beta^2} |\mathcal{A}(\vec{q}_d)|^2, \quad (45)$$

which again expresses the van CittertZernike theorem, but now for the *object*. Since the object is non-radiating, one may interpret the result (45) as the “speckles of darkness” cast by the object. This phenomenon can be viewed as a realization of the Babinet’s principle in intensity interferometry. Of course, it is not possible to arrive to the limit (45) by simply turning off the source, $I_s(\vec{\rho}) \equiv 0$, because it would turn to zero the entire expression. However this limit can be achieved when the source speckle is much smaller than the object speckle, or equivalently, when the source angular size far exceeds that of the object. This limit is therefore consistent with approximation (42). If it is satisfied, the source part of the correlation function may still be large, but will be localized much tighter than the object part, which may have a relatively small magnitude.

To quantify the relative magnitude of the object signature we note that $\mathcal{T}_s(0)/I_s(0)$ and $\mathcal{A}(0)$ are the source and the object effective areas, respectively (or the actual areas, if $I_s = \text{const}$ for the entire source and $A = 1$ for the entire object). Therefore it is easy to see that the ratio $\beta^2\mathcal{A}(0)I_s(0)/\mathcal{T}_s(0) \approx (\beta D_o/D_s)^2 \ll 1$ is the fraction of the optical power radiated by the source that is absorbed by the object. This proves an important statement made earlier, that the object signature in the correlation measurement has the same magnitude as in the direct intensity measurement.

Now we can also understand the earlier discussed stereoscopic aspect of the intensity interferometric imaging, which has allowed us to distinguish the orbits orientations for transients, at a more fundamental level. At the heart of this capability is the phase between the source and object terms of (43) which can mediate their constructive or destructive interference. This phase depends on the object displacement $\vec{\rho}_o$ projected onto the detectors’ baseline $\vec{\rho}_d$, and has no counterpart in conventional observations based on intensity measurements. However, considering the synthetic aperture analogy, we notice that this phase variation corresponds to the object passing through Fresnel zones of a fictitious telescope with aperture ρ_d . It also should be noted that this exponential arises from a Fourier transform of a shifted object $A(\vec{\rho} + \vec{\rho}_o)$ and can be absorbed into $\mathcal{A}(\vec{q}_d)$ without a loss of generality.

Below we will investigate two analytically tractable examples of objects crossing the line of sight of a thermal light source, in close simulation of an exoplanet observation scenario.

For a disc-shaped source and object,

$$I_s(\vec{\rho}) = I_s(0)\text{circ}(|\vec{\rho}|/r_s) \equiv \begin{cases} I_s(0) & \text{for } |\vec{\rho}| \leq r_s \\ 0 & \text{otherwise,} \end{cases} \quad (46)$$

and

$$A(\vec{\rho}) = \begin{cases} 1 & \text{for } |\vec{\rho}| \leq r_o \\ 0 & \text{otherwise,} \end{cases} \quad (47)$$

where $r_o \ll r_s$. Substituting these into Eq. (43), we can write

$$C(x, \theta) = \frac{4CP^2}{L^4\beta^4} \left| \frac{J_1(\pi x/\beta)}{\pi x/\beta} - \beta^2\gamma^2\text{circ}(\beta x_o) \frac{J_1(\pi\gamma x)}{\pi\gamma x} e^{-i\pi x x_o \cos(\theta)} \right|^2, \quad (48)$$

where $x \equiv 2|\vec{\rho}_d|r_s/(\lambda L)$ is the normalized displacement of the detectors, $x_o \equiv |\vec{\rho}_o|/r_s$ is the fractional displacement of the object relative to the source radius, $\theta \equiv \angle\vec{\rho}_d - \angle\vec{\rho}_o$ is the angle between the vectors $\vec{\rho}_d$ and $\vec{\rho}_o$, $P \equiv I_s(0)\pi r_s^2$ is the photon flux of the source, and $\gamma \equiv r_o/r_s$ is the object-to-source size ratio.

Let us consider the image signature from a *differential* observable, which is given by a difference of the measurement with no object, and one with an object present, while nothing else changes. We will assume that the object is much smaller than the source, $\gamma^2 \ll 1$. Then a linearized differential observable is given by the cross-term of Eq. (48) as

$$\Delta C(x, \theta) \approx -2C\frac{\gamma}{\beta} \left(\frac{2P}{\pi x L^2} \right)^2 \text{circ}(\beta x_o) J_1(\pi x/\beta) J_1(\pi\gamma x) \cos(\pi x x_o \cos(\theta)). \quad (49)$$

To evaluate the magnitude of the object's signature we need to specify the parameters of Eq. (49). Typical values of these parameters are given in Table III for two scenarios: a table-top laboratory demonstration, and an Earth-size planet partially occultating a Sun-size source observed from a distance equivalent to that of Kepler 20f. In Fig. 19 we show the results for $C(x, \theta)$ and $\Delta C(x, \theta)$ with a fixed object displacement x_o , for both the lab and the stellar examples.

From Fig. 19 we see that the object signature is mainly manifested by the variation of the correlation function width. We plot this width in Fig. 20 as a function of displacement x_o within the range of approximation (42) validity. This plot corresponds to an observation

Variable	λ [m]	L_s [m]	L [m]	r_s [m]	r_O [m]	$\beta-1$	γ	$\lambda L/(2r_s)$ [m]
Lab	10^{-6}	0.5	0.5	0.01	0.001	1	0.1	$2.5 \cdot 10^{-5}$
Kepler	10^{-6}	$1.496 \cdot 10^{11}$	$8.948 \cdot 10^{18}$	$6.955 \cdot 10^8$	$6.371 \cdot 10^6$	$1.67 \cdot 10^{-8}$	$9.16 \cdot 10^{-3}$	$6.433 \cdot 10^3$

TABLE III: Parameters for a typical lab demo and a stellar imaging example similar to Kepler 20f.

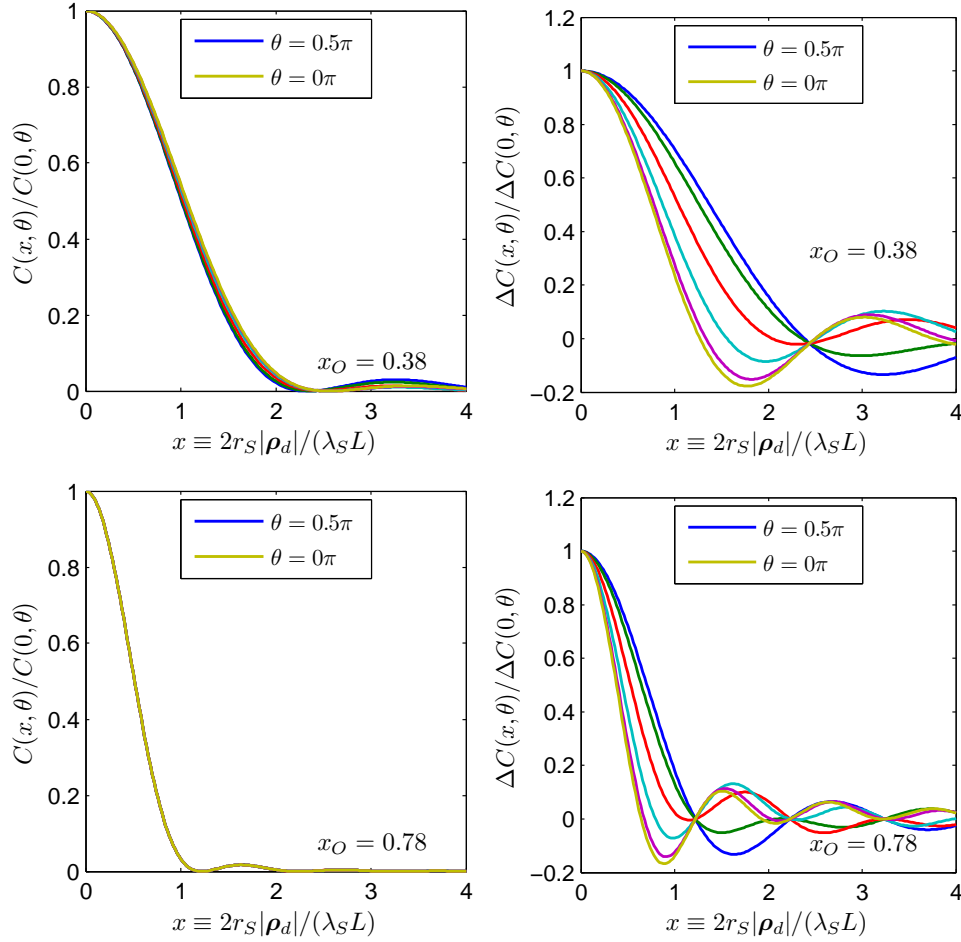


FIG. 19: The normalized correlation measurement observable $C(x, \theta)$ (left column) and its object-induced variation $\Delta C(x, \theta)$ (right column) for the lab demo case (upper row) and stellar imaging case (lower row) are plotted as a function of x for $\theta/\pi = 0$, (the inner curve), 0.1, 0.2, 0.3, 0.4 and 0.5 (the outer curve). The object displacement from the line of sight x_o is fixed as shown.

of the object's transient across the source, crossing the line of sight when $x_o = 0$. While the intensity measurement at $x = 0$ is obviously independent of the transient direction, the θ -dependence of the correlation measurement in Fig. 20 is evident. Thus in the stellar imaging example, one would be able to learn about the planetary ecliptic plane orientation

from this measurement.

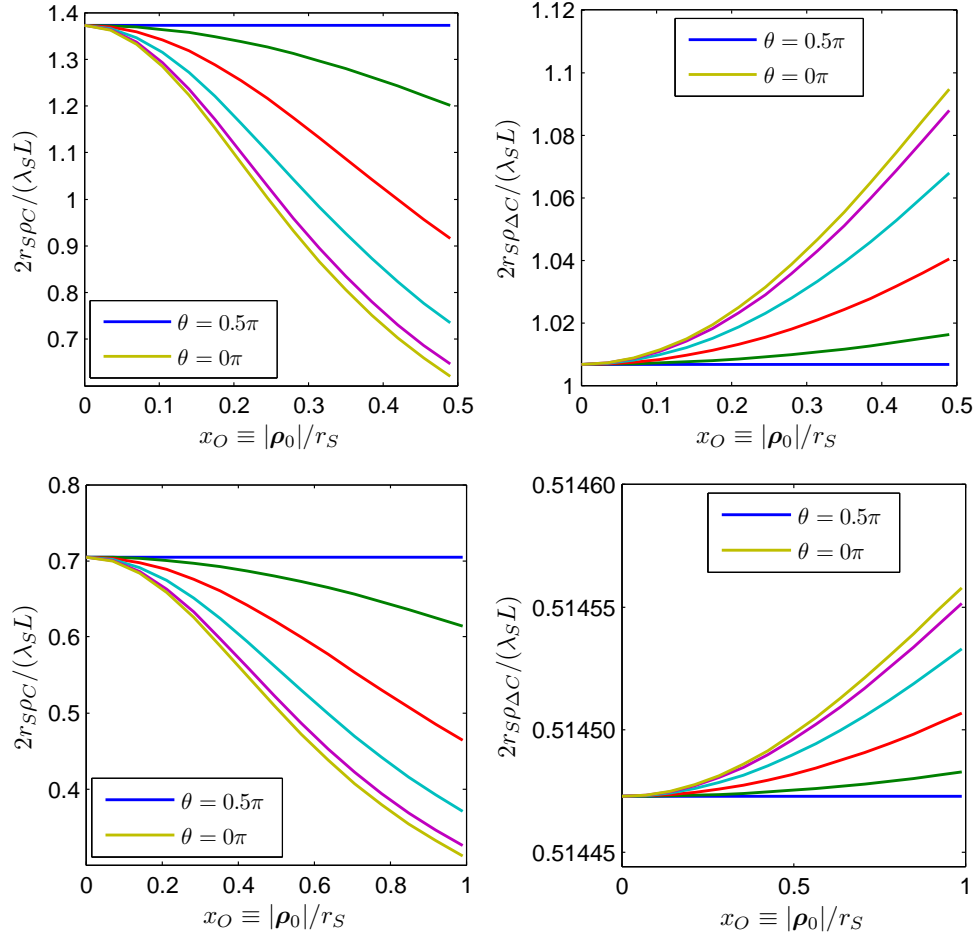


FIG. 20: Widths of the correlation functions from Fig. 19 normalized to the speckle width $\lambda L/(2r_s)$ as a function of the object's transient parameter x_o for $\theta/\pi = 0$, (strongest dependence), 0.1, 0.2, 0.3, 0.4 and 0.5 (constant).

Returning to our initial model of Gaussian profiles of the source and object, we have

$$T_s(\vec{\rho}) = e^{-2|\vec{\rho}|^2/r_s^2}, \quad A(\vec{\rho}) = e^{-2|\vec{\rho}|^2/r_o^2}, \quad (50)$$

where again $r_o \ll r_s$. Substituting these into Eq. (43) and carrying out similar approximations, we obtain

$$C = \frac{CP_G^2}{L^4\beta^4} \left| e^{-\frac{\pi^2 x^2}{8\beta^2}} - \beta^2 \gamma^2 e^{-2\beta^2 x_o^2} e^{-\frac{\pi^2}{8} \gamma^2 x^2} e^{-i\pi x x_o \cos(\theta)} \right|^2, \quad (51)$$

and

$$\Delta C \approx -2 \frac{CP_G^2}{L^4\beta^2} \gamma^2 e^{-2\beta^2 x_o^2} e^{-\frac{\pi^2 x^2}{8\beta^2}} e^{-\frac{\pi^2}{8} \gamma^2 x^2} \cos(\pi x x_o \cos(\theta)) \quad (52)$$

where $P_G = I_s(0)\pi r_s^2/2$, and all other variables have been defined earlier. For the stellar interferometry case with $\beta \approx 1$, we obtain

$$C \approx \frac{\mathcal{C}P_G^2}{L^4} \left| e^{-\frac{\pi^2}{8}x^2} - \gamma^2 e^{-2x_o^2} e^{-\frac{\pi^2}{8}\gamma^2 x^2} e^{-i\pi x x_o \cos(\theta)} \right|^2, \quad (53)$$

and

$$\Delta C \approx -2 \frac{\mathcal{C}P_G^2}{L^4} \gamma^2 e^{-2x_o^2} e^{-\frac{\pi^2}{8}(1+\gamma^2)x^2} \cos(\pi x x_o \cos(\theta)) \quad (54)$$

In Figs. 21 and 22 we have plotted the same results as before, but now for the Gaussian case.

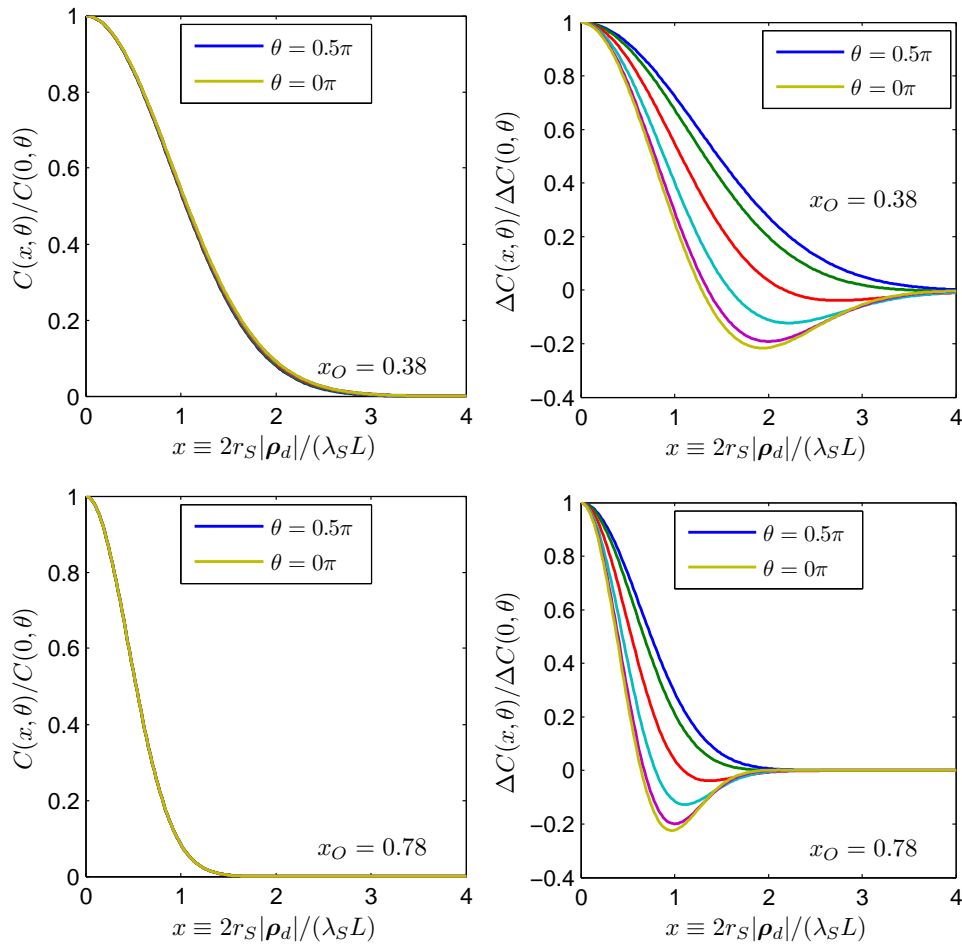


FIG. 21: Gaussian case equivalent of Fig. 19.

Let us note that despite some quantitative difference between the disk and Gaussian models considered above, they both capture all essential aspects of the object signature. Therefore we can use either the disk model for more realistic approximation of stellar or planetary objects, or Gaussian model for more transparent analytical treatment.

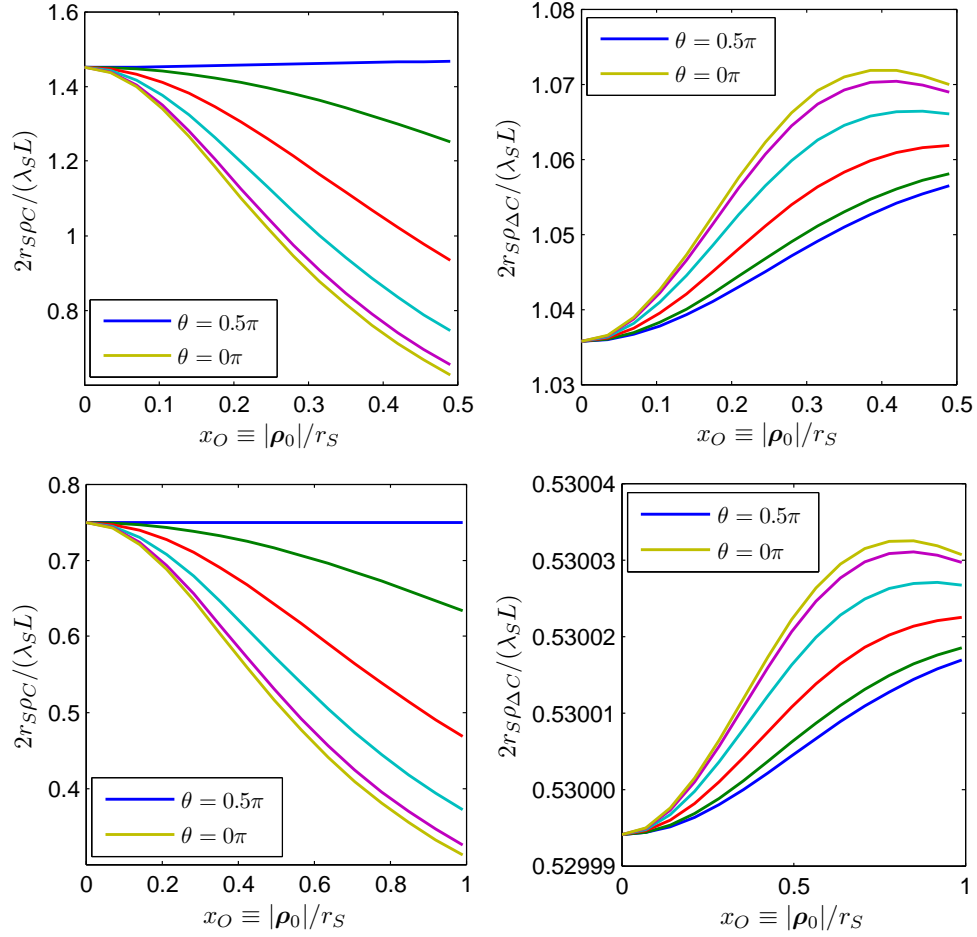


FIG. 22: Gaussian case equivalent of Fig. 20.

B. On observability of a shadow gradient

It should be mentioned that while the object shadow observed at any single point does not provide information about the transient direction, the shadow *gradient* may. We need to investigate this possibility in order to determine if and when it can compete with the stereoscopic feature of the intensity interferometry approach. To compare our intensity correlation results with direct intensity gradient measurements, let us evaluate

$$\langle i(\vec{\rho}, t) \rangle \equiv \eta A_d \int d\tau \langle |E_d(\vec{\rho}, \tau)|^2 \rangle h_{lp}(t - \tau), \quad (55)$$

where h_{lp} is now the *low-pass* filter response function, allowing for the DC intensity measurement. The field absolute square in the integrand is easily obtained by evaluating the

right-hand side of Eq. (38), with the substitutions $\vec{\rho}_s = \vec{\rho}$ and $\vec{\rho}_d = 0$, which yields

$$\langle |E_d(\vec{\rho}, \tau)|^2 \rangle = K_O(0; L + L_s) - K_D(\vec{\rho}_s, 0) = \frac{P_s}{L^2 \beta^2} [1 - \beta^2 I_n(\beta \vec{\rho}_o - (\beta - 1) \vec{\rho}) \mathcal{A}(0)]. \quad (56)$$

Here $P_s \equiv \int d^2 \rho I_s(\vec{\rho})$, and $I_n(\vec{\rho}) \equiv I_s(\vec{\rho})/I_s(0)$ is the normalized source intensity. It is worthwhile to recall that the mean image signature derived here is based on the same assumptions and approximations as the correlation observable derived above.

Substituting Eq. (56) into Eq. (55) we assume that $\int dt h_{lp}(t) = 1$ (i.e., unity DC gain) and drop the time variable in the stationary photo current. We arrive at

$$\langle i(\vec{\rho}) \rangle = \frac{\eta A P_s}{L^2 \beta^2} [1 - \beta^2 I_n(\beta \vec{\rho}_o - (\beta - 1) \vec{\rho}) \mathcal{A}(0)] \quad (57)$$

as the direct observation signature. Here, the first term is the uniform intensity illumination due to the unobscured source, and the second term is the variation due to the object. The shadow gradient, which could potentially be used for determining the transient direction, can be defined as

$$\frac{1}{\langle i(\vec{\rho}) \rangle} \frac{\partial \langle i(\vec{\rho}) \rangle}{\partial \vec{\rho}} \approx \beta^2 (\beta - 1) I'_n(\beta \vec{\rho}_o - (\beta - 1) \vec{\rho}) \mathcal{A}(0). \quad (58)$$

For the order-of-magnitude estimate, we will assume Gaussian distribution for both the source luminosity and the object opacity (50). Then $\mathcal{A}(0) = \pi r_o^2/2$, and the maximum value of $I'_n(\rho_m) = 2/r_s$ is achieved at $\rho_m = r_s/2$.

To make a fair comparison with the intensity interferometry measurement, we need to multiply the gradient (58) by the measurement baseline, which is of the order of a speckle size $2(L + L_s)/(kr_s)$. We arrive at

$$\frac{\Delta \langle i \rangle}{\langle i \rangle} \approx \frac{\lambda L_s}{\pi R_s^2} \beta^3 \gamma^2. \quad (59)$$

We use expression (59) to evaluate the relative intensity variation across the speckle width due to the shadow gradient, and compare it with other object's signatures such as the relative intensity variation due to the object's presence and the normalized variation of the speckle width, see Table IV. As expected, the magnitudes of the intensity variation signature and of the correlation measurement signature (the first two lines of Table IV) are very close. Intensity gradient, on the other hand, provides a far inferior signature (the third line of Table IV), which is not useful e.g. for determining the transient plane. This is the case because the sharp shadow condition [56] is opposite to assumption (42). Therefore we conclude, that the correlation measurement indeed provides the information unavailable from the intensity measurements.

Observable (normalized)	Lab demo	Stellar imaging
Intensity variation	9×10^{-2}	2×10^{-4}
Speckle width variation	7×10^{-2}	1.7×10^{-4}
Intensity variation per speckle	1.3×10^{-4}	1.0×10^{-17}

TABLE IV: Magnitude of the object’s signature in three types of observables and the parameter sets from Table III.

C. Signal-to-noise ratio

Evaluating the feasibility and efficiency of correlation-based observations in Astronomy requires a careful study of the signal-to-noise ratio (SNR), which strongly depends on the object of interest and the imaging geometry. The conventional approach to the intensity interferometry SNR [41, 57] is based on the analysis of fluctuation of the photo currents $i_1(t)$ and $i_2(t)$ produced by the detectors in response to the incident optical field. This analysis can be easily generalized for the photon-counting detectors. The mean values of these photocurrents are given in Eq. (8). The SNR of the intensity correlation observable $C(\vec{\rho}_1, \vec{\rho}_2)$ given by Eq. (9) is defined as

$$\text{SNR} \equiv \frac{\langle C \rangle}{\sqrt{\text{Var}(C)}}. \quad (60)$$

This SNR has been evaluated in [57]. While its general formula is rather cumbersome, two important limits can be considered for the thermal light with the single-mode Glauber correlation function $g^{(2)}(0) = 2$.

In the limit of a quasi-monochromatic source or very high-speed photodetectors and coincidence electronics, $T_c \gg T_B$. For such a “narrowband” case, [57] predicts

$$\text{SNR}^{(nb)} = \frac{\sqrt{TT_B}}{T_c} \frac{N}{\sqrt{1 + 2N(T_B/T_c) + 5N^2(T_B/T_c)^2}}, \quad (61)$$

where $N \equiv \eta A_d(T_c/T) \int_0^T dt \langle |E_d(t)|^2 \rangle$ (for $d = 1, 2$) is the mean photoelectron number per longitudinal mode (or equivalently, per coherence time) of the fields incident on the detectors, and T is the total time of measurement. The terms in the denominator of (61) have intuitive interpretations. The first term, which is independent of N , is due to the shot noise of the two detectors. The third term, with the N^2 dependence, is excess noise resulting from the statistical fluctuations of the incident power on the detectors. This term

is sometimes referred to as relative intensity noise. The middle term, with the linear N dependence, is a result of the beating between the intensity fluctuations and shot noise.

In the shot-noise-limited regime $N \ll 1$ holds, i.e., the mean number of photoelectrons *per mode* is very small, and the SNR can be approximated as

$$\text{SNR}_{N \ll 1}^{(nb)} = \frac{\sqrt{TT_B}}{T_c} N. \quad (62)$$

In the opposite regime with many photoelectrons per mode, $N \gg 1$, the SNR saturates to its maximum value

$$\text{SNR}_{N \gg 1}^{(nb)} = \sqrt{\frac{T}{5T_B}}. \quad (63)$$

In the opposite “broadband” limit of slow electronics or a broad-band source, when $T_c \ll T_B$, [57] predicts

$$\text{SNR}^{(bb)} = \sqrt{\frac{T}{T_B}} \frac{N}{\sqrt{1 + 2N + 2N^2 T_c/T_B}} \quad (64)$$

which has the following limits:

$$\text{SNR}_{N \gg 1}^{(bb)} = \sqrt{\frac{TN}{2T_B(1 + NT_c/T_B)}} \quad \text{and} \quad \text{SNR}_{N \ll 1}^{(bb)} = N \sqrt{\frac{T}{T_B}}. \quad (65)$$

The behavior of the $N \gg 1$ limit in (65) depends on the product of a large number N by a small number T_c/T_B . Depending on the relation between these numbers, the SNR may continue to increase with the increasing signal, or may reach saturation as in (63). The $N \ll 1$ limit of (65) is often encountered stellar intensity interferometry. This result is usually written as

$$\text{SNR}_{N \ll 1}^{(bb)} = n(\lambda) A_d \eta \sqrt{T \Omega_B / 2}, \quad (66)$$

where the spectral density $n(\lambda) = T^{-1} \int_0^T dt \langle |E_d(\lambda, t)|^2 \rangle$ is the mean number of thermal light photons per unit area, per unit frequency (around the central wavelength λ) and per unit time [59], and the electronic bandwidth $\Omega_B = 2/T_B$. Equivalently, (66) can be written in terms of the photon flux F defined as the number of photons per unit area and per unit time within an optical bandwidth $\Delta\lambda$ around the central wavelength λ :

$$\text{SNR}_{N \ll 1}^{(bb)} = \frac{\lambda^2 F}{2\pi c \Delta\lambda} A_d \eta \sqrt{T \Omega_B / 2}. \quad (67)$$

For direct intensity measurements, the signal is proportional to the electric charge acquired during an integration time T :

$$Q = \int_0^T dt \langle i(t) \rangle, \quad (68)$$

where the mean photocurrent is given by Eq. (55). In this case the SNR is defined as

$$\text{SNR}_Q \equiv \frac{\langle Q \rangle}{\sqrt{\langle (Q - \langle Q \rangle)^2 \rangle}}, \quad (69)$$

which leads to

$$\text{SNR}_Q = \sqrt{\frac{T}{T_c} \frac{N}{1 + N}}, \quad (70)$$

where all parameters are as defined before.

To separate the SNR dependence on the integration time T , which is common to both the correlation and direct intensity measurements, it is convenient to normalize the SNR to $\sqrt{T/T_c}$. Fig. 23 shows thus normalized SNR of a direct intensity measurement (70) and the asymptotic approximations (62) and (63) of a correlation measurement, as functions of the mean photoelectron number per mode. As seen from this figure, the correlation measurement SNR can approach the direct intensity measurement SNR for the sources with high spectral brightness $N \approx 1$.

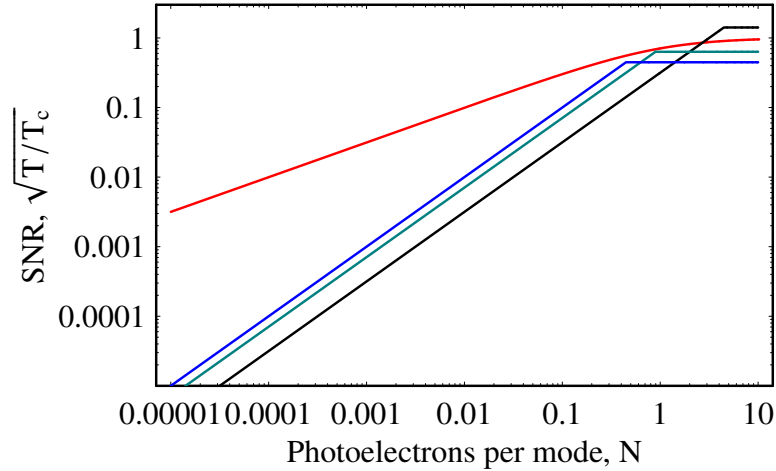


FIG. 23: The normalized intensity SNR (red) and correlation measurement SNR for $T_B/T_c = 0.1$ (black), 0.5 (green), and 1 (blue).

The shot-noise limited correlation-based measurements typically have worse SNR than direct intensity measurements due to the stronger dependence of the former on the incident average photon number N/T_c . However in the excess-noise limited regime, the correlation measurements' SNR improves due to the fact that such measurements can distinguish source fluctuations from those caused by an object better than the direct-intensity measurement.

Note, however, that the plots in Fig. 23 compare the SNRs for equal numbers of photoelectrons per mode relying on the assumption $T_B < T_c$. This assumption implies strong

spectral filtering which reduces the total photon flux available for the correlation measurement. The direct intensity measurement, on the other hand, can integrate over a very wide optical bandwidth without penalty. We have already discussed this aspect of correlation imaging technique considering the example of Solar spectrum, see Fig. 11 and related discussion. Again, let us keep in mind that the spectral filtering penalty may be reduced for intrinsically narrow-band imaging, e.g. imaging using a specific bright or dark spectral line. A narrow spectral feature will lead to the higher spectral brightness and give the correlation imaging advantage according to Fig. 23.

The SNR analysis presented above is typically performed for the “conventional” intensity interferometry. Here we are interested not in the full intensity correlation signal but rather in the signature of a dark object present in this signal. This signature may be weak relative to the baseline signature from the source alone and often can be treated as a perturbation. The easiest way to detect such a perturbation is by a differential measurement, that is, by subtracting the signal of the source without the object from the source with the object present. Many observation scenario (such as e.g. planets transients) naturally support such a measurement technique. However, while a differential measurement can eliminate the source’s baseline and improve the visibility of the object’s perturbation, it will not eliminate the noise contributed by the source. Therefore we need to derive the SNR of the differential measurement in order to develop a better appreciation for the sensitivity of this measurement.

The differential measurement observable can be expressed as $\Delta C(\vec{\rho}_1, \vec{\rho}_2) = C_1(\vec{\rho}_1, \vec{\rho}_2) - C_0(\vec{\rho}_1, \vec{\rho}_2)$, where C_1 is the Eq. (9) measurement *with* the object of interest present, and C_0 is the same measurement *without* the object. As typically these two measurements are separated by a duration significantly longer than the coherence time of the photocurrent fluctuations, the two measurements can be assumed statistically uncorrelated. Thus, the variance of the measurement is,

$$\text{Var}(C_1 - C_0) = \text{Var}(C_1) + \text{Var}(C_0) \approx 2\text{Var}(C_0) \quad (71)$$

where the last approximation arises from our earlier observation that the object’s perturbation signature is significantly weaker than that of the source. Consequently, in this regime it can be assumed that the variance of either measurement will be dominated by the source-induced shot- and excess-noise fluctuations.

The SNR can, therefore, be expressed as

$$\text{SNR} \approx \frac{|\Delta C|}{\sqrt{2\text{Var}(C_0)}} \quad (72)$$

which is different from Eq. (60). We have derived the numerator of expression (72) for the disk and Gaussian source and object profiles (see Eqs. (49) and (52), respectively), so here we focus on the denominator. Using the photocurrent moments discussed above (8), we can express the variance as

$$\text{Var}(C_0) = \int d\tau_1 \int d\tau_2 \int d\tau'_1 \int d\tau'_2 K_h(\tau_1, \tau_2) K_h(\tau'_1, \tau'_2) K_i(\tau_1, \tau_2, \tau'_1, \tau'_2), \quad (73)$$

where

$$K_h(\tau_1, \tau_2) = T^{-1} \int_{-T/2}^{T/2} dt h(t - \tau_1) h(t - \tau_2), \quad (74)$$

and

$$\begin{aligned} K_i(\tau_1, \tau_2, \tau'_1, \tau'_2) = & (\eta A_d)^2 \left[\langle |E_1(\tau_1)|^2 |E_2(\tau_2)|^2 \rangle \delta(\tau_1 - \tau'_1) \delta(\tau_2 - \tau'_2) + \right. \\ & + \eta A_d \langle |E_1(\tau_1)|^2 |E_1(\tau'_1)|^2 |E_2(\tau_2)|^2 \rangle \delta(\tau_2 - \tau'_2) + \\ & + \eta A_d \langle |E_1(\tau_1)|^2 |E_2(\tau_2)|^2 |E_2(\tau'_2)|^2 \rangle \delta(\tau_1 - \tau'_1) + \\ & + (\eta A_d)^2 \{ \langle |E_1(\tau_1)|^2 |E_1(\tau'_1)|^2 |E_2(\tau_2)|^2 |E_2(\tau'_2)|^2 \rangle - \\ & \left. - \langle |E_1(\tau_1)|^2 |E_2(\tau_2)|^2 \rangle \langle |E_1(\tau'_1)|^2 |E_2(\tau'_2)|^2 \rangle \} \right]. \end{aligned} \quad (75)$$

The terms in Eq. (75) have intuitive physical meaning: the first term is the covariance of common-mode fluctuations in the shot noise (i.e., the conditional variance) from the two detectors, the next two terms are the covariances between the shot noise fluctuations in one detector and the signal fluctuations in the other detector, and the last term is the covariance between the signal fluctuations (i.e., the conditional mean-square) from the two detectors.

In order to evaluate Eq. (73), we first perform Gaussian moment factoring [54] on each term in Eq. (75). This yields expressions for every term in Eq. (75) in terms of $K_D(\vec{\rho}_1, \vec{\rho}_2)$, which is given in Eq. (40). Next, we assume that the AC-coupled photodetector impulse responses $h(t)$ are Gaussian-shaped with bandwidth Ω_B , namely,

$$h(t) = \sqrt{\frac{\pi\Omega_B^2}{2}} e^{-t^2\Omega_B^2/8} - \sqrt{\frac{\pi\Omega_N^2}{2}} e^{-t^2\Omega_N^2/8}. \quad (76)$$

The second term here represents the DC notch with bandwidth Ω_N . Henceforth, we assume that $\Omega_B \gg \Omega_N$ and $\Omega_N T_c \ll 1$, which allows us to effectively neglect the notch's contribution

to any nonzero-frequency terms. Our final assumption in evaluating the Eq. (73) is that the integration time T is much longer than both the detector's response time ($T\Omega_B \gg 1$) and the optical coherence time ($T/T_0 \gg 1$), such that we may approximate Eq. (74) as

$$K_h(\tau_1, \tau_2) = T^{-1} \text{rect} \left(\frac{|\tau_1 + \tau_2|}{T} \right) [h \star \overleftarrow{h}](\tau_2 - \tau_1), \quad (77)$$

where \star denotes convolution and \overleftarrow{h} denotes time reversal.

Skipping the steps of evaluating each term in the variance expression, we write the final result for the SNR in a differential measurement:

$$\text{SNR}^{(diff)} = \frac{\cos(\theta_d)\alpha}{\sqrt{\sigma_{ss}^2 + \sigma_{se}^2 + \sigma_{ee}^2}}. \quad (78)$$

Assuming symmetric detectors' positions ($\vec{\rho}_s = 0$), we can write

$$\theta_d = \pi x x_o \cos(\theta), \quad (79)$$

and

$$\alpha \equiv \frac{K_D^{(n)}(\vec{\rho}_s, \vec{\rho}_d)}{K_O(0; L + L_s)} = \beta^2 \gamma^2 \begin{cases} \text{circ}(\beta x_o) \frac{2J_1(\pi \gamma x)}{\pi \gamma x} \\ e^{-2\beta^2 x_o^2} e^{-\pi^2 \gamma^2 x^2 / 8} \end{cases} \quad (80)$$

where the upper case correspond to the disk model and the lower case correspond to the Gaussian model. When $\gamma x \ll 1$, $\beta \approx 1$, and $\beta x_o < 1$ (as in most of the stellar imaging cases), both instances simplify to $\alpha \approx \gamma^2$.

The three terms in the denominator of the $\text{SNR}^{(diff)}$ expression are given by

$$\begin{aligned} \sigma_{ss}^2 &\equiv \frac{\sqrt{2}}{\sqrt{\pi} T \Omega_B \Gamma N^2} \left[1 + \frac{T_c \Omega_B \Gamma}{\sqrt{8} \sqrt{1 + \frac{\Omega_B^2 T_c^2}{8}}} \right], \\ \sigma_{se}^2 &\equiv \frac{2\sqrt{2}}{T \Omega_B \Gamma N} \frac{1 + \frac{T_0^2 \Omega_B^2}{16}}{\sqrt{1 + \frac{T_0^2 \Omega_B^2}{32}}} \left[1 + \frac{\sqrt{2} T_c \Omega_B \Gamma}{\sqrt{3}} \frac{\sqrt{1 + \frac{T_0^2 \Omega_B^2}{32}}}{\sqrt{1 + \frac{T_0^2 \Omega_B^2}{8}} \sqrt{1 + \frac{T_0^2 \Omega_B^2}{24}}} \right], \\ \sigma_{ee}^2 &\equiv \frac{\sqrt{2\pi}}{T \Omega_B \Gamma} \sqrt{1 + \frac{T_0^2 \Omega_B^2}{16}} \left[1 + \Gamma^2 + \frac{T_c \Omega_B \Gamma}{\sqrt{1 + \frac{\Omega_B^2 T_c^2}{8}}} \left(1 + \Gamma + \frac{\sqrt{1 + \frac{T_0^2 \Omega_B^2}{16}}}{\sqrt{1 + \frac{T_0^2 \Omega_B^2}{8}}} \right) \right], \end{aligned} \quad (81)$$

where

$$\Gamma \equiv \left| \frac{K_O(\vec{\rho}_d; L + L_s)}{K_O(0; L + L_s)} \right|^2 \in [0, 1] \quad (82)$$

is the equal-time correlation coefficient between the photocurrents registered at the two detectors, given in terms of K_O which is defined in Eq. (36).

Just as before, it is useful to consider two limiting cases of the $\text{SNR}^{(diff)}$ expression: the case of broadband incident light ($\Omega_B T_c \ll 1$), and of narrowband light ($\Omega_B T_c \gg 1$), relative to the photodetectors bandwidth. Because naturally occurring light sources are typically broadband and are filtered optically at the measurement plane, the broadband limit will usually hold in practical applications. However, with the pseudothermal light sources commonly used in the laboratory settings, the narrowband limit can be applicable.

In the broadband ($\Omega_B T_c \ll 1$) limit, the expression of Eq. (78) simplifies to

$$\text{SNR}^{(diff-bb)} \approx \frac{N \sqrt{T \Omega_B / 2} \cos(\theta_d) \alpha \sqrt[4]{2\pi \Gamma^2}}{\sqrt{1 + 2\sqrt{\pi} N + \pi(1 + \Gamma^2) N^2}}, \quad (83)$$

which has the following low and high signal limits:

$$\text{SNR}_{N \ll 1}^{(diff-bb)} = \frac{\lambda^2 F}{2\pi c \Delta \lambda} A_d \eta \sqrt{T \Omega_B / 2} \cos(\theta_d) \alpha \sqrt[4]{2\pi \Gamma^2} \quad (84)$$

(c.f. Eq. (67)), and

$$\text{SNR}_{N \gg 1}^{(diff-bb)} = \alpha \cos(\theta_d) \sqrt{\frac{\Gamma T \Omega_B}{\sqrt{2\pi}(1 + \Gamma^2)}}. \quad (85)$$

Figure 24(a) shows the transition of the normalized SNR from the photon-starved region to its maximum, as a function of N .

In the narrowband ($\Omega_B T_c \gg 1$) limit, on the other hand, Eq. (78) yields

$$\text{SNR}^{(diff-nb)} \approx \alpha \cos(\theta_d) \sqrt{\frac{\Gamma T}{T_c}} \left[\frac{\sqrt{2}(1 + \Gamma)}{\sqrt{\pi} N^2 T_c \Omega_B} + \frac{(1 + 2\Gamma)}{N} + \frac{\sqrt{\pi}}{2\sqrt{2}} (1 + 2(\sqrt{2} + 1)\Gamma + (1 + 2\sqrt{2})\Gamma^2) \right]^{-1/2}. \quad (86)$$

In this case the photocurrent correlation time is approximately T_c , so the SNR is now proportional to $\sqrt{T/T_c}$. For $N^2 T_c \Omega_B \ll 1$, the signature is photon-starved and the SNR has a linear dependence on mean photon flux. As N increases to $N \gg 1$, the SNR saturates at its maximum value,

$$\text{SNR}_{N \gg 1}^{(diff-nb)} = \sqrt{\frac{T}{T_c}} \frac{\alpha \cos(\theta_d) \sqrt{2\Gamma \sqrt{2/\pi}}}{\sqrt{1 + 2(\sqrt{2} + 1)\Gamma + (1 + 2\sqrt{2})\Gamma^2}}. \quad (87)$$

Figure 24(b) illustrates the variation of the normalized SNR as a function of N in the narrowband case.

In principle, we can chose the narrow band measurement strategy for an intrinsically broadband source by implementing spectral filtering at the detectors so that $\Omega \ll \Omega_B$. In

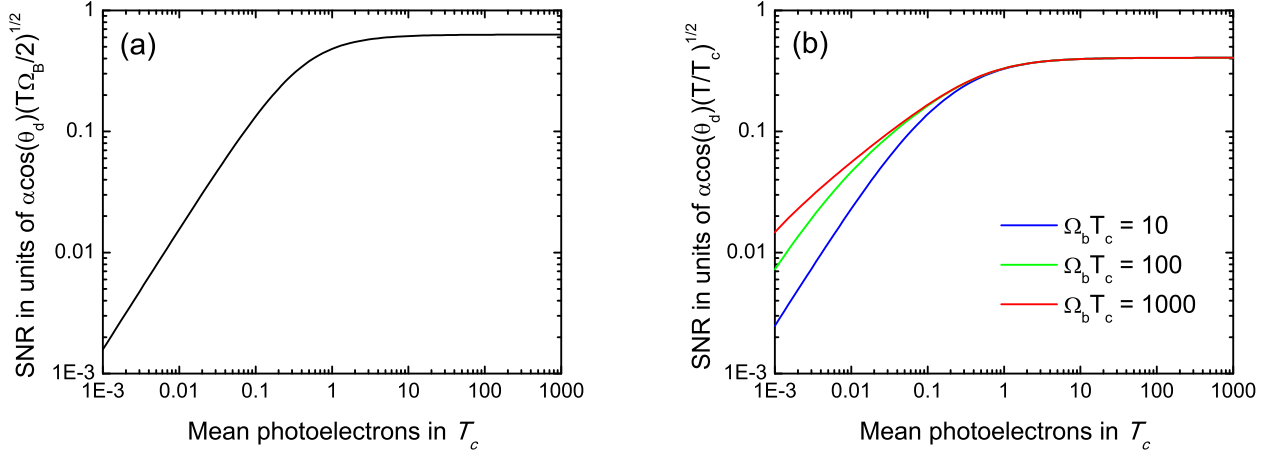


FIG. 24: (a) The normalized signal to noise ratio of the differential intensity covariance measurement is plotted as a function of N for the broadband case. In this case the normalized SNR is independent of the $\Omega_B T_c$ product. (b) The same is plotted for the narrowband case. In this case the normalized SNR in the $N \ll 1$ regime has a dependence on the $\Omega_B T_c$ product such that a larger SNR is attained for larger product, but the maximum (attained when $N > 1$) is independent of this product. In both cases $\Gamma = 1$ is assumed.

the beginning of this section we have already assumed following this approach. It is easy to see that such filtering would not change the spectral brightness of the source, and therefore will not change N . Comparing Eqs. (83) and (86) in the limit of $N \ll 1$ we then find

$$\text{SNR}_{\text{Stel}}^{(\text{nb})} = \frac{\text{SNR}_{\text{Stel}}^{(\text{bb})}}{\sqrt{2}}. \quad (88)$$

This result indicates that for a *uniformly* broadband thermal light source the benefit of increasing the correlation function contrast by going into the single-mode detection regime via spectral filtering is negated by the consequent signal reduction. Similar conclusion was reached in [9] by different reasoning.

Let us estimate the SNR for the two examples from Table III, assuming $\Gamma = 1$ and $\cos(\theta_d) = 1$. In the Lab demo case we assume that a laser-based pseudothermal light source is implemented and the narrowband limit is appropriate. With such a source the $N \gg 1$ regime can be easily achieved, so we can use the maximum SNR value (87). This yields $\text{SNR}_{\text{Lab}} \approx 1.28 \beta_{\text{Lab}}^2 \gamma_{\text{Lab}}^2 \sqrt{T/T_c} = 1.62 \times 10^{-2} \sqrt{T/T_c}$. Thus, with a 1 MHz-wide laser we would need approximately 4 ms integration time to obtain a statistically significant signal

with $\text{SNR}_{\text{Lab}} > 1$. Remarkably, for a better measurement with this scenario one needs a broader-band laser (provided that it remains narrowband compared to the detectors).

To evaluate the SNR in a stellar system measurement, let us return to Eq. (84) and express the photon flux F via the apparent magnitude M_a of the source using the standard expression

$$F[s^{-1}m^{-2}] = 1.51F_0[Jy]\frac{\Delta\lambda}{\lambda}10^{7-M_a/2.5}, \quad (89)$$

where the constant F_0 depends on the spectral band [58]. We obtain

$$\text{SNR}_{\text{Stel}}^{(\text{diff})} = 1.51 \cdot 10^{7-M_a/2.5} A_d \eta \gamma^2 \frac{\lambda F_0}{2\pi c} \sqrt{\Gamma T/T_B} \cos(\theta_d) \sqrt[4]{2\pi}, \quad (90)$$

where all parameters are measured in SI units. In the following we will assume $\Gamma = 1$, $\cos(\theta_d) = 1$ as we did for the Lab example above. It is then convenient to rewrite (90) in the form

$$\text{SNR}_{\text{Stel}}^{(\text{diff})} \approx 1.27 \cdot 10^{-8-M_a/2.5} A_d [m^2] \lambda [\mu m] \eta \gamma^2 F_0 \sqrt{T/T_B}. \quad (91)$$

Returning to the Kepler-20f example, we notice that Kepler-20 is a magnitude 12.497 star in the V+R spectral band [3], characterized by the central optical wavelength $\lambda \approx 500$ nm and $F_0 \approx 3350$ Jy. Let us assume that we have a unity-efficient ($\eta = 1$), ultrafast photo detectors with $T_B = 50$ ps that are coupled to the same kind of telescopes as were actually used in the Kepler mission, with light collection area of 1.54 m^2 . Then from (91) we find

$$\text{SNR}_{\text{Stel}}^{(\text{dif})} \approx 4.63 \cdot 10^{-5} \gamma_{\text{Stel}}^2 \sqrt{T[s]}. \quad (92)$$

Substituting $\gamma_{\text{Stel}} = 9.16 \cdot 10^{-3}$ from Table III, it is easy to find that in order to reach the SNR value of 10^{-4} , achieved in the direct intensity measurement [2], one would have to collect signal for some $6.6 \cdot 10^8$ seconds, or 21 years.

The discouraging result for Kepler20f system's SNR is largely due to a very low brightness of the host star and very small planet-to-star diameter ratio γ . We however can follow this approach to evaluate the systems with more favorable parameters. For this analysis we will assume the light collection area $A_d = \pi(2 \text{ m})^2 \approx 12.6 \text{ m}^2$ as for the CTA project's SST1M telescope, the full detection efficiency $\eta = 0.5$, and the detectors/electronics resolution time $T_B = 1 \text{ ns}$. Then instead of (92) we obtain

$$\text{SNR}_{\text{Stel}}^{(\text{dif})} \approx 2.53 \cdot 10^{-7-M_a/2.5} F_0 \gamma^2 \lambda [nm] \sqrt{T[s]}. \quad (93)$$

Let us allow some reasonable time for the measurement, e.g. $T = 1$ hour, and evaluate the resulting SNR for intensity-interferometric detection of brighter stars' exoplanets listed in Table II. We skip the systems that lack the information necessary to carry out the evaluation. These results are shown in the last column of Table V.

Star	Distance (pc)	M_a	λ_{peak} (nm)	$F_0[\text{Jy}]$	γ	SNR per 1 hour (10^{-4})
<u>Upsilon Andromedae</u>	13.5	4.09	474	4100	0.105	76
<u>82 G. Eridani</u>	6.1	4.25	537	3680	0.0168	1.7
<u>HD 60532</u>	25.4	4.46	475	4100	0.078	30
<u>61 Virginis</u>	8.6	4.74	524	3700	0.0274	2.8
<u>47 Ursae Majoris</u>	14.1	5.10	492	4000	0.117	37
<u>Mu Arae</u>	15.6	5.15	508	3930	0.0899	21
<u>HD 47536</u>	123.3	5.26	662	3020	0.00902	0.19
<u>HD 142</u>	25.8	5.70	469	4100	0.124	24
<u>Gliese 777</u>	15.9	5.71	519	3850	0.0971	15
<u>HD 169830</u>	36.5	5.91	462	4180	0.087	9.6
<u>HD 38529</u>	39.2	5.94	509	3900	0.0912	11
<u>55 Cancri</u>	12.3	5.95	555	3620	0.137	24
<u>HD 69830</u>	12.6	5.95	538	3710	0.0272	0.93
<u>HR 8799</u>	39.6	5.96	390	2670	0.09	0.53
<u>HD 217107</u>	19.9	6.18	513	3850	0.105	11
<u>HD 11964</u>	32.8	6.42	525	3770	0.0382	1.2
<u>24 Sextantis</u>	77.6	6.44	568	3560	0.0258	0.54
<u>23 Librae</u>	26.1	6.45	521	3850	0.094	7.1
<u>HD 1461</u>	23.3	6.47	503	3900	0.0162	0.2
<u>14 Herculis</u>	17.5	6.67	546	3650	0.239	37
<u>HD 40307</u>	12.9	7.17	582	3400	0.0271	0.3
<u>HD 154857</u>	64.1	7.25	532	3710	0.0571	1.2
<u>HD 10180</u>	38.9	7.33	490	3970	0.0308	0.33
<u>HD 12661</u>	35.0	7.44	505	3900	0.121	4.6
<u>HD 128311</u>	16.6	7.51	584	3400	0.203	12
<u>HD 11506</u>	51.8	7.54	478	4000	0.101	3.4
<u>83 Leonis</u>	18.1	7.57	594	3400	0.0376	0.41
<u>HD 74156</u>	64.4	7.61	480	4000	0.124	4.0
<u>HD 37124</u>	33.7	7.68	517	3850	0.109	3.0
<u>HD 183263</u>	55.2	7.86	492	4000	0.127	3.5

TABLE V: Parameters of some brightest stars that are known to have a planet, potentially suitable for intensity interferometry observations.

We see that only among the exoplanet systems there are many good candidates for intensity-interferometric observations with the SNR matching or exceeding that achieved in Kepler-20f observations. Of course, the required SNR level will depend on the specific measurement, which will be possible to obtain by scaling the results from Table V according to Eq. (93).

To summarize this section, we admit that in general, the SNR of correlation measurements and especially of differential measurements detecting small dark objects is considerably worse than of direct intensity measurements. Obviously, in order to have a realistic assessment of the added value of correlation-based measurements for imaging space objects, one must take into account additional factors such as stray light, detector aging, natural variation of the source brightness and other practical concerns that are usually omitted in the SNR analyses published to date. The detectors' dark noise, for example, may be particularly important in cases when the incident photons flux is low. This implies an extensive analysis that needs to be carried out for each potential system of interest individually. We include this research into the follow-on proposals that are intended to advance the present NIAC research.

D. From detection to imaging

Deriving the correlation observable (43) we have noticed that it captures both the source and the object's images (i.e., the transverse distribution of their luminosity and opacity column densities, respectively). This suggests that we can pursue a much more ambitious goal than to just detect a dark object's presence or even to establish its transient direction. We can attempt to reconstruct the object's image or contour. Following the *differential measurement* approach, we assume that the source shape is well-known (perhaps from intensity-interferometric imaging without the object), and we need to reconstruct the object shape. This problem falls into a general category of phase recovery from an absolute-square Fourier transform. There are a few well-known approaches to this type of problems such as the Cauchy-Riemann [10, 11, 60–62] and Gerchberg-Saxton [63–65] approaches. We have adopted the latter approach and optimized it specifically to meet our goals.

A conceptual diagram of the Gerchberg-Saxton algorithm is shown in Fig. 25. The algorithm is based on a cyclic manipulation with the initially unknown image and its Fourier transform, of which only the absolute value is known. During this process, additional infor-

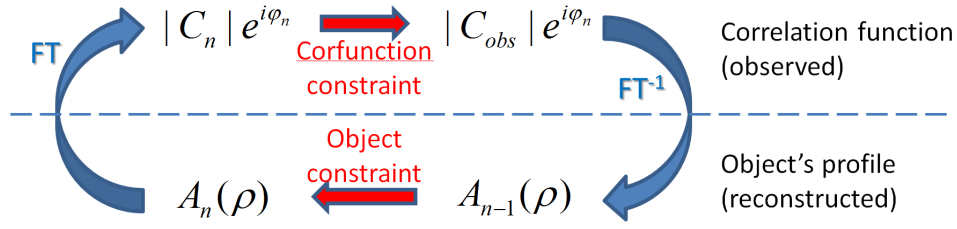


FIG. 25: A conceptual diagram of the Gerchberg-Saxton iterative algorithm.

mation is injected into the cycle. This information may come from various common sense considerations, even those apparently unrelated to the object's shape. Surprisingly, these consideration can often be informative enough to allow for complete image reconstruction.

We have modeled, studied and optimized the Gerchberg-Saxton reconstruction process by first encoding an object (supplied in a form of a graphical image, e.g. a photo, or defined analytically) into the correlation observable (43), and then processing the result following the algorithm shown in Fig. 25. This simulation and analysis were implemented in the Python programming language. A specialized software package was created for this purpose, whose functional diagram is shown in Fig. 26.

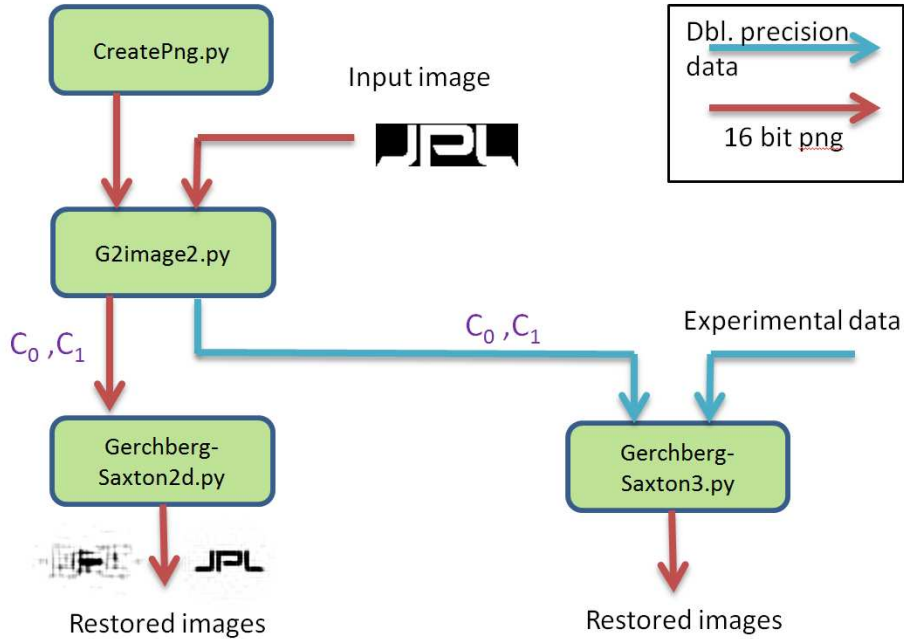


FIG. 26: A diagram of the image encoding/recovering software package developed at JPL.

The pristine image can be created by the CreatePng.py program which offers several options for basic geometric shapes. Alternatively, the image can be taken as a picture or photograph formatted into 16-bit gray scale png file. The image is passed on to the G2image2.py program which generates the correlation observables C and C_0 according to formula (43). These observables are output both in graphic (16-bit gray scale png) and double-precision data array formats. The program has options of assuming either Gaussian or disk source, and introducing additive and/or multiplicative noise to the correlation observables. It also creates a log file where all relevant parameters of the system are recorded. This file is used by the image-reconstruction programs.

The graphic observables are passed on to the Gerchberg-Saxton2d.py program, which realizes the iterative process shown in Fig. 25. In order to make the image recovery process more realistic, this program ignores the prior knowledge of the source shapes. Instead, it relies on C_0 as the sole description of the source. It does, however, require the *a priori* source shape information: Gaussian or disk. The images obtained from this program are compared with the pristine image.

Similar functions are performed by the Gerchberg-Saxton3.py program, except that it takes double-precision data arrays as C and C_0 inputs. This array format closely matches the potential experimental data, so the purpose of this program is to facilitate the transition to the future experimental data analysis.

To handle this problem numerically, we introduce three reciprocal pairs of grids: a and \tilde{a} in the object plane, b and \tilde{b} in the detection plane, and c and \tilde{c} in the source plane. Each of these grids is related to its reciprocal by a discrete Fourier transform of an $N_0 \times N_0$ array, e.g. $a = 2\pi/(N_0\tilde{a})$, etc. Furthermore, discretizing of (43) leads to the following natural choice:

$$\tilde{a} = kb/L \quad \text{and} \quad \tilde{c} = kb/(L + L_s). \quad (94)$$

During the encoding step, we use Eq. (43) to generate correlation arrays $C(\rho_{i,j})$ and $C_0(\rho_{i,j})$ with and without the object, respectively. The arrays size is $N_0 \times N_0$, where by virtue of Eqs. (94) $N_0 = \lambda L/(ab)$. These arrays represent the correlation measurement results with a square array of detectors spaced at $b/2$. The arrays are then truncated to the actual size of the detectors array $N_d \times N_d$, which determines the new object grid $a' = \lambda L/(N_d b)$ and sets the resolution limit for our image reconstruction.

Then the Gerchberg-Saxton reconstruction takes place. Our algorithm follows the general

guidelines [64, 65], however with a few important modifications. As we already mentioned, we abandon our *a priori* analytical expression for $\mathcal{T}(\vec{q})$ and restore it from the $C_0(\rho_{i,j})$ “measurement” in order to more closely simulate an experimental procedure. As an initial guess for the object’s shape we take a Gaussian function whose width is consistent with the total optical power absorbed by the object:

$$A(\vec{\rho}) = \exp \left\{ -\frac{\pi \rho^2}{\sqrt{C_0(0)} - \sqrt{C(0)}} \right\}. \quad (95)$$

Following the Gerchberg-Saxton procedure we then compute \mathcal{A} and replace its amplitude by the “measurement” $\sqrt{C(\rho_{i,j})}$, while retaining its phase. After the inverse Fourier transform this leads to a new estimate for A which we constrain based on sensible assumptions regarding the object. These assumptions are the following:

1. $A(\vec{\rho})$ is real;
2. $A(\vec{\rho}) = 0$ for $\rho > \rho_{Max}$, which means that the object is not too large;
3. $0 \leq A(\vec{\rho}) \leq 1$, which means that the object cannot absorb more than all, or less than none, of the incident light;
4. $A(\vec{\rho}) = 0$ or 1, if the object is completely opaque.

The first constraint can be enforced by taking either the absolute value, or the real part of A . Both methods work, as well as their alternation, converging to the same result. We prefer the alternation method because it provides an indication of the successful image reconstruction, as we will see in the following. It also sometimes leads to a slightly faster convergence.

In the second constraint, the limit ρ_{Max} can be determined e.g. from low-resolution observations [65], from supplementary knowledge such as the object mass, etc. In the absence of such data, we set ρ_{Max} to six times the initial Gaussian width (95).

In the third constraint, imposing the upper limit on the reconstructed function is a new requirement, specific to dark objects. In contrast, reconstructing a light source one cannot be sure that it does not have very bright spots, so the upper limit is not applicable.

The last constraint is specific to completely opaque objects, in which case we are limited to reconstructing only its contour. When applied, it supersedes the previous constraint. We

have found that applying this constraint directly often disrupts the iteration process instead of helping it, especially for the objects of complex shapes. A more subtle way of injecting a large amount of information implied in the last constraint into the reconstruction process is needed. Such a way can be facilitated by modifying the input-output transfer function $A_{n-1}(\vec{\rho}) \rightarrow A_n(\vec{\rho})$ which relates the previous and the next images after all other constraints have been applied. We have empirically studied several types of such transfer functions. One particularly successful example is shown in Fig. 27. As the reconstruction iterations progress, the darker pixels are gradually driven towards unity (opaque), and lighter pixels towards zero (transparent).

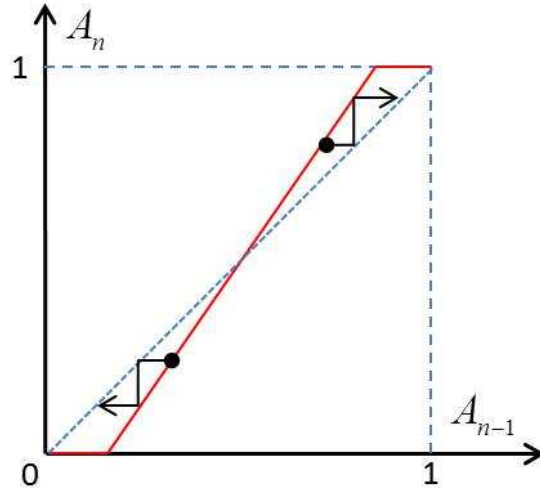


FIG. 27: A transfer function (solid line) applied to the object’s absorption profile between $(n - 1)$ -th and n -th Gerchberg-Saxton iterations gradually drives it towards black-and-white solution. A dashed line represents an identity transfer function $A_n = A_{n-1}$.

The reconstruction process dynamics can be studied by monitoring the normalized variances

$$\sigma_n \equiv \frac{\sum_{i,j} |A_n(\rho_{i,j}) - A_{n-1}(\rho_{i,j})|^2}{\sum_{i,j} |A_{n-1}(\rho_{i,j})|^2}, \quad \tilde{\sigma}_n \equiv \frac{\sum_{i,j} |\mathcal{A}_n(\rho_{i,j}) - \mathcal{A}_{n-1}(\rho_{i,j})|^2}{\sum_{i,j} |\mathcal{A}_{n-1}(\rho_{i,j})|^2}, \quad (96)$$

whose square-roots give the fractional change of the object and its Fourier transform at the n -th step. It is useful to separately calculate a part $\sigma_n^{(o)}$ of σ_n which is due to the “opaque object” constraint alone.

Following a long-standing tradition in the field of *Ghost imaging* [13], we demonstrate the performance of our modified Gerchberg-Saxton algorithm using the initial letters of our

institution, JPL, as a test object. This numeric simulation is carried out in a typical optical lab settings. The object, which is shown in Fig. 28, was assumed to have 2 mm in length. It is placed at $L = L_s = 36$ cm between the source and the detectors array. The array has 1280×1024 pixels with $4.65 \mu\text{m}$ spacing (hence, $b = 9.3 \mu\text{m}$) to match parameters of the actual CCD camera which was used in our experiment. The source is assumed to have Gaussian distribution with $R_s = 2$ mm, radiating at $\lambda = 532$ nm.



FIG. 28: The test object and its computed shadow as would be seen by the detectors array.

Geometrical shadow of an object can be found as

$$I(\vec{\rho}) = 1 - \frac{\beta^2}{\pi R_s^2} \int d^2\xi I_s(\beta\vec{\xi} - (\beta - 1)\vec{\rho}) A(\vec{\xi}). \quad (97)$$

In our case, this shadow is only some 14% deep, see Fig. 28. It is completely featureless and is not useful for the image reconstruction.

The correlation function, on the other hand, has a rich structure which encodes the object image. In Fig. 29 we plot $C(\rho_{i,j})$ on a logarithmic scale in order to highlight the weak features. The outer green and inner red contour lines correspond to $C(\rho_{i,j})/C_0(0) = 2^{-13}$ and $C(\rho_{i,j})/C_0(0) = 2^{-12}$, respectively.

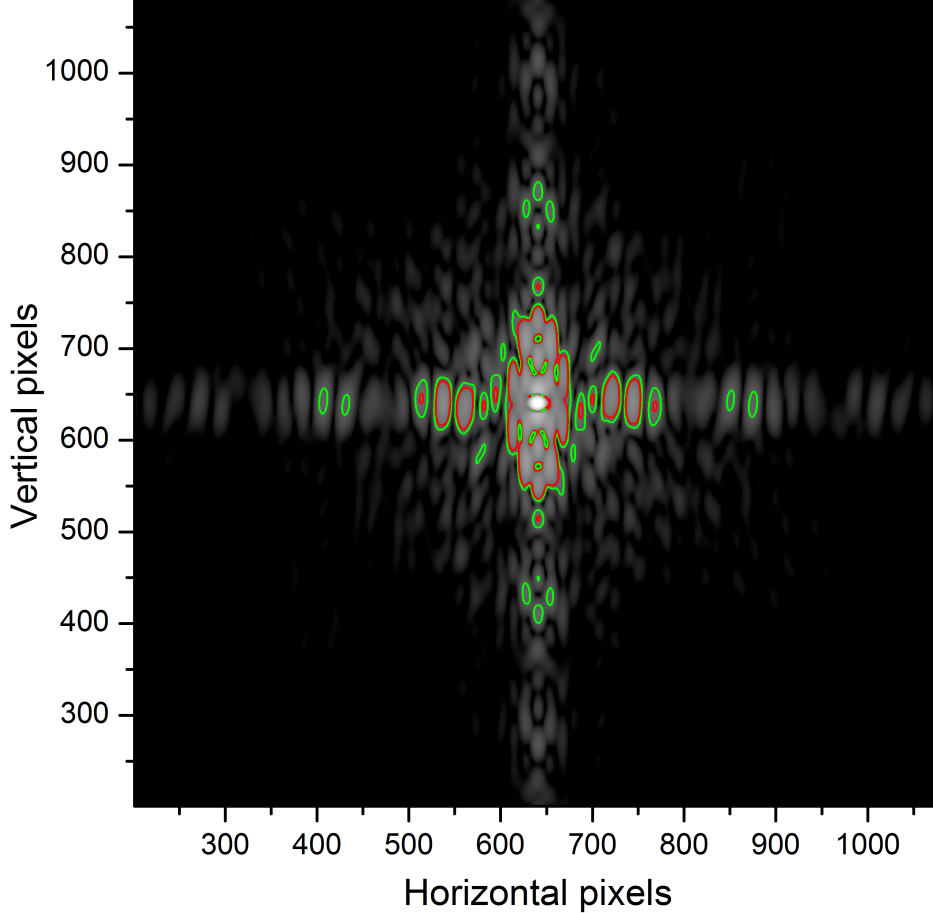


FIG. 29: A logarithmic plot of the correlation function $C(\rho_{i,j})$ reveals the structure which encodes the shape of the object of interest. The solid contour lines correspond to $C(\rho_{i,j})/C_0(0) = 2^{-12}$ (red) and $C(\rho_{i,j})/C_0(0) = 2^{-13}$ (green).

We started by realizing a simple version of the Gerchberg-Saxton algorithm, with constraint 4 disabled by permanently setting the slope of the transfer function in Fig. 27 to unity. The real part of the object function was taken when applying constraint 1. Representative images of a 200-iteration cycle are shown in Fig. 30. These images have been rotated by 180° for convenience; the actual results of this particular run came out up side down, which is a normal situation resulting from the Gerchberg-Saxton algorithm ambiguity.

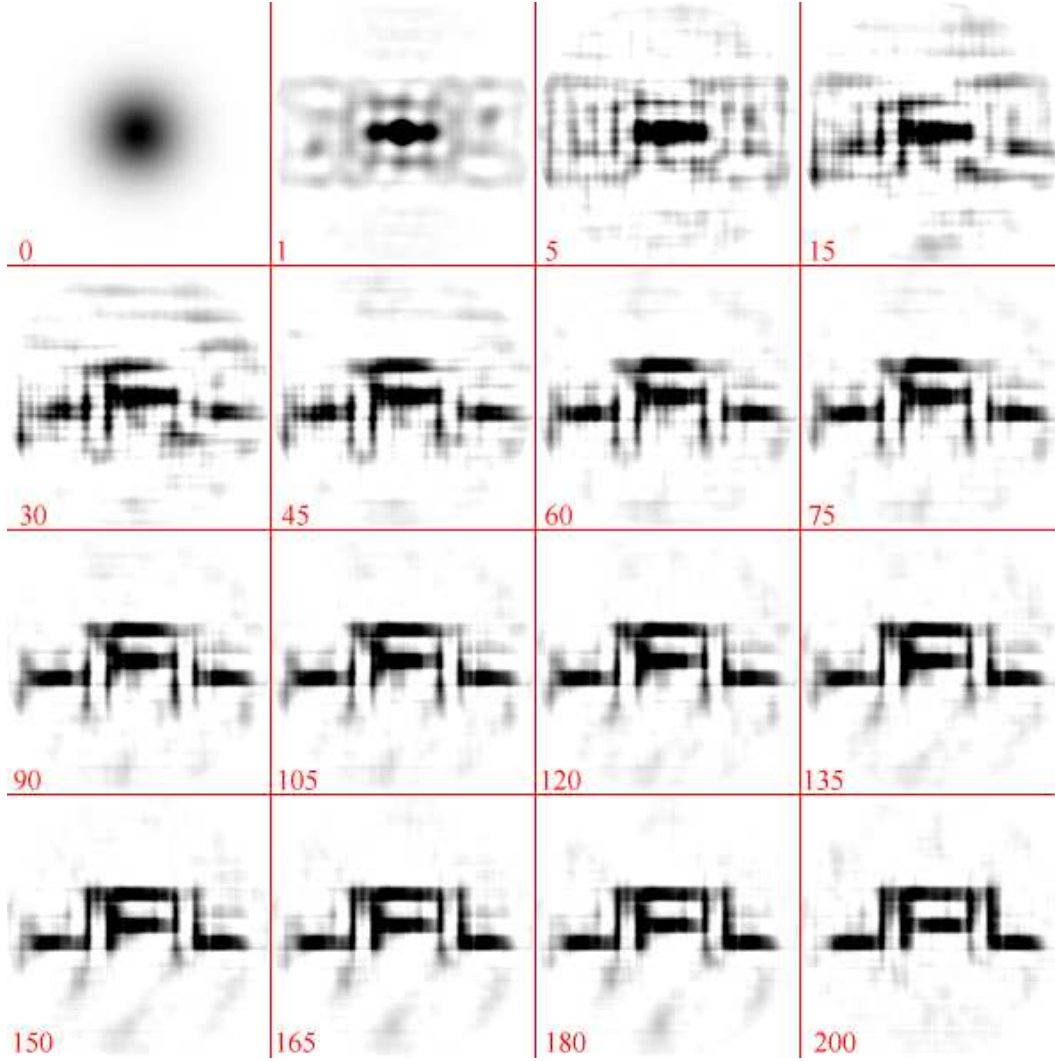


FIG. 30: The results of a simple image recovery algorithm. The step numbers are given in the low left corner of each frame.

Variances (96) for this process are shown in Fig. 31. Their general behavior is similar to the one observed [64] for luminous objects, when periods of rapid improvement were alternating with periods of relative stagnation. Convergence of the process can be improved if one alternates taking the real part of the image and its absolute value as the first image constraint. The variances behavior and representative images corresponding to this scenario are shown in Fig. 32. Here, the same simulated input data has been used, however the second quality transition occurs sooner, and the final image is better. Notice that the steps when the “absolute value” method was used in constraint 1 have larger variances than those when the “real part” method was used.

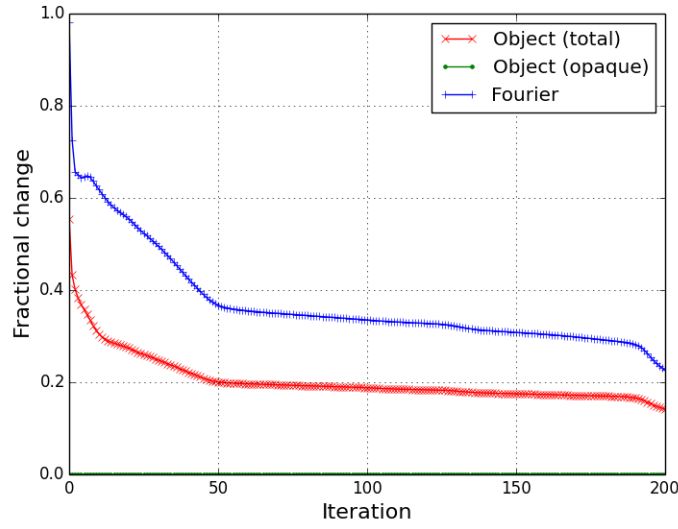


FIG. 31: Fractional change (given by square root of variances (96)) of the test object's image and its Fourier transform in a simple image recovery corresponding to Fig. 30.

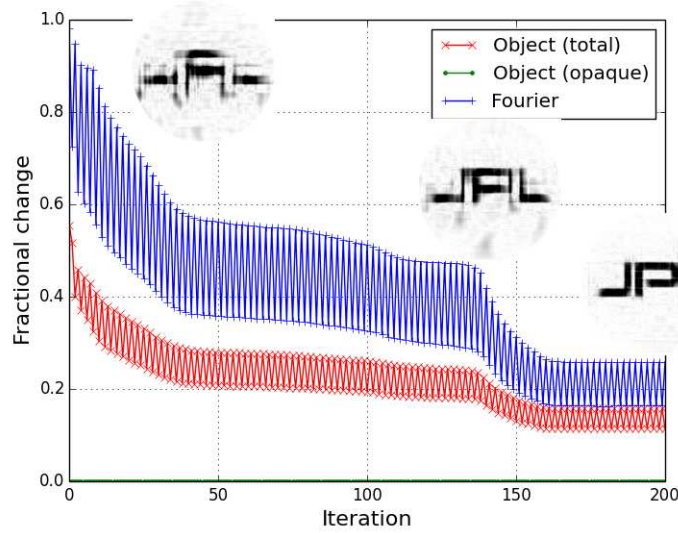


FIG. 32: Fractional change of the test object's image and its Fourier transform in the alternating algorithm; shown are images 40, 130 and 200.

So far we have not utilized our knowledge that the test object is in fact an opaque mask. To take advantage of this information, we enable the “solid object” constraint. We start incrementing the transfer function slope (see Fig. 27) by small steps as soon as both the image and its Fourier transform's evolution becomes stagnant, but will decrement it if either

one of the variances (96) starts to grow. The results of such an *adaptive* Gerchberg-Saxton algorithm with the same input data are shown in Fig. 33. Its realization leads to even faster convergence with even better result. In fact, the image in Fig. 33 stops appreciably changing already after some 125 iteration, at which point it looks practically indistinguishable from the original.

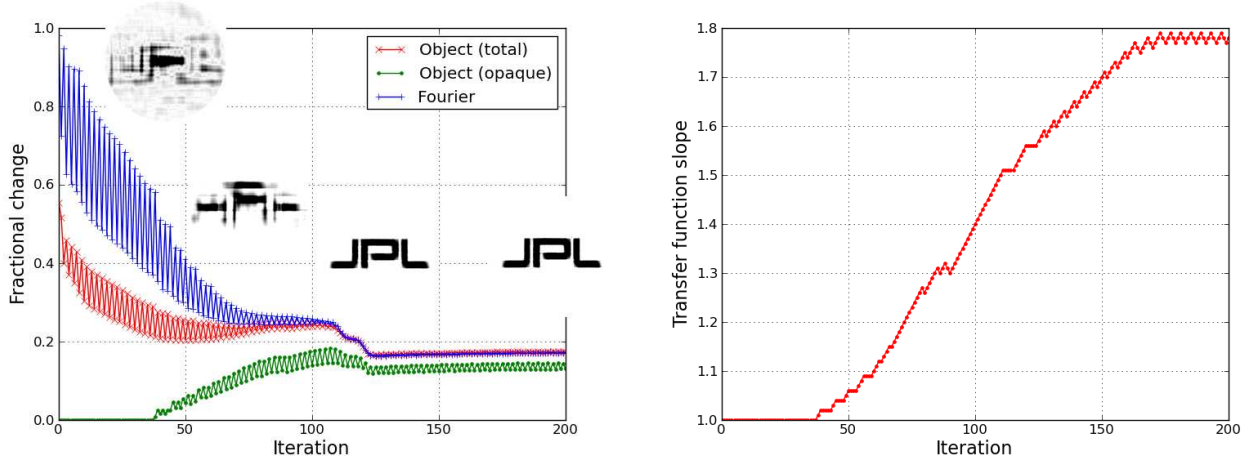


FIG. 33: Left: fractional change of the test object’s image and its Fourier transform in the alternating adaptive algorithm; shown are images 10, 75, 125 and 200. Right: the transfer function slope.

Several interesting observations can be made regarding this result. First, the variances oscillations due to alternating method of handling the complex-to-real conversion disappear as the image improves. This indicates that the image becomes purely real and suggests that with the adaptive algorithm, alternating the methods may be unnecessary. We have confirmed it in a separate run using only the “Real” method which has produced equally good result. Second, the image and its Fourier transform fractional variations become equal when a high-quality image has been obtained and no further progress is achieved. This may indicate that the process has gone into a loop where the object- and Fourier-space constraints repeatedly reverse each other’s effect. Third, the largest part of the object variance is due to the “opaque” constraint, which is consistent with the image solutions being predominantly real and well confined in space.

An important question of practical intensity interferometry imaging is the algorithm tolerance to additive and multiplicative noise. The additive noise is most important in

the dark areas of Fig. 29 where the correlation observable C is small. This type of noise can be suppressed by applying a threshold. Therefore the detrimental effect of this type of noise is limited by such effect of the threshold. To study this effect we have repeated the reconstruction with the same correlation data thresholded at $C(\rho_{i,j})/C_0(0) = 2^{-13}$ and $C(\rho_{i,j})/C_0(0) = 2^{-12}$, which corresponds to discarding the data outside the green (outer) and red (inner) contour lines in Fig. 29, respectively. The restored images are shown in Fig. 34. These images cannot be improved with more iterations.



FIG. 34: The image reconstruction results with the threshold set at 2^{-13} (left) and 2^{-12} (right).

The multiplicative noise was introduced by multiplying each pixel value of $C(\rho_{i,j})$ and $C_0(\rho_{i,j})$ by a random Gaussian function with the mean value equal to unity and a variable width σ_{noise} . The reconstruction process failed at $\sigma_{noise} = 0.01C_0(0)$ but converged to a practically ideal image at $\sigma_{noise} = 0.001C_0(0)$. In practical realizations of this image-reconstruction algorithm, the realistic multiplicative noise level can be inferred from the SNR analysis discussed in the previous Section.

To test our approach with an astronomical parameters set, we consider a hypothetical Earth-size planet in the Oort cloud (1 ly from the Sun) which occultates Sirius (8.6 ly from the Sun, $6 \mu\text{arc sec}$ angular size). The planet would have $0.35 \mu\text{arc sec}$ angular size and would absorb some 0.34% of photon flux from Sirius. To make imaging more exciting we provide the planet with a Saturn-like ring and a pair of moons 1000 km in diameter. The central wavelength is assumed to be $\lambda = 532 \text{ nm}$. The correlation measurements array is assumed to consist of 2000×2000 data points on a square grid with 2 m period. This does not mean that an array of 4 million detectors would be required. As we have seen before, a modest-size array of cleverly placed detectors, such as shown in Fig. 8(a), can cover a lot of reciprocal space and generate a very large correlation data array, such as shown in Fig. 8(b), if all possible pairs of detectors are considered. In general, the resulting data array would not be represented on a square grid. We assume the square grid in this simulation in order to

accommodate our image reconstruction software. Obviously, modifying our software in such a way as to handle the correlation data arrays of any shape would be among the first-priority tasks in the follow-on research efforts that will be based on this NIAC project.

The reconstruction results are shown in Fig. 35. We see that already the first iteration yields a nearly faithful image of the planet, but with four semi-transparent moons instead of two solid ones, and a few other minor defects. It takes about 50 iterations to eliminate the fake moons. At this point the iteration process saturates, meaning that continuing it further does not noticeably change the image.

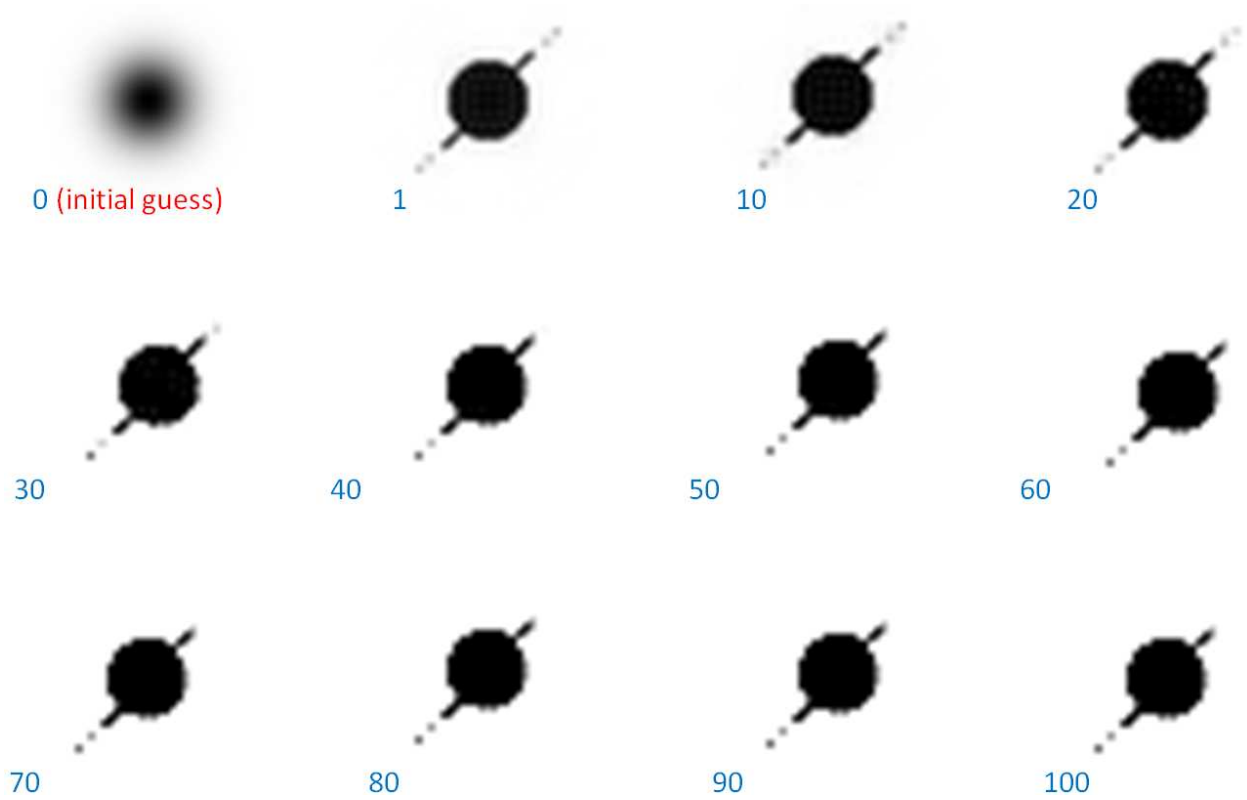


FIG. 35: The results of a planetary image reconstruction without noise. The step numbers are given in the low left corner of each frame.

In the reconstruction shown in Fig. 35 we assumed noiseless data. Let us now model a more realistic case when multiplicative noise is present. Following the analysis from the previous Section, we notice that in the present geometry the factor β is no longer close to unity: $\beta = 1 + L_s/L \approx 8.6$. A square of this factor needs to multiply the right hand side of Eq. (93) for the SNR. Substituting $M_a = -1.47$, $F_0 = 1800$ Jy, $\lambda = 290$ nm and $\gamma = R_{Earth}/R_{Sirius} \approx 5.37 \times 10^{-3}$ into thereby modified equation, we find that $\text{SNR} =$

0.1 can be reached with a $T = 2.8$ hour measurement. We have used the noise-encoding capability of our correlation simulating software to generate the noisy “measurement” result, and reconstructed the original image using the same set of parameters as before. The reconstruction results are shown in Fig. 36.

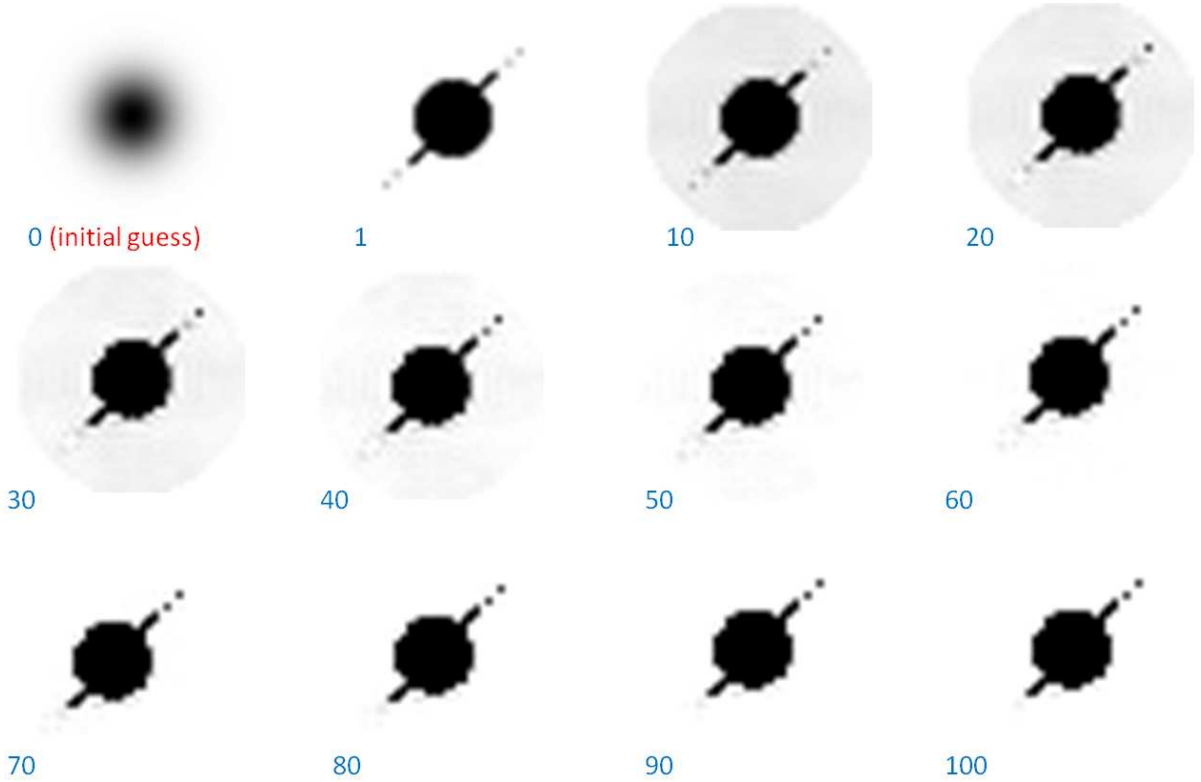


FIG. 36: Image reconstruction results for the same system as in Fig. 35 but with strong multiplicative Gaussian noise present, $\text{SNR} = 0.1$. The step numbers are given in the low left corner of each frame. Notice that the images in this Figure are inverted with respect to those in Fig. 35, which is a normal situation in Gerchberg-Saxton algorithms.

Remarkably, a strong (ten times the signal!) noise present at every correlation data point did not disrupt the image reconstruction. Its presence only lead to a persistent background which nonetheless disappeared after some 50 iterations. This background may be attributed to the high spatial frequency component of the noise, which affects the low-frequency part of the objects, that is, its bulk size. This effect causes a problem which can be understood by reviewing Eq. (95). This equation expresses the object bulk size as the difference between the DC components of the correlation arrays with and without the object. For small objects this difference is small, and in presence of the DC noise its fluctuation may be significant.

To overcome this problem, for the image recovery from the noisy data we still used the bulk size estimate obtained from the noiseless measurement. This “trick” is justified by the following consideration: since the DC component of the correlation array is simply the detected optical power, its measurement can be performed with a much greater precision by an auxiliary apparatus relying only on the intensity measurement and not requiring spectral filtering and high measurement bandwidth. Running into this difficulty and successfully resolving it has been an important experience that will need to be taken into consideration in a realistic mission design.

E. Experimental demonstration

To gain confidence in our theoretical estimations and numerical simulations, it is highly desirable to compare them to actual experimental measurements. To reduce the equipment costs, it has been decided to carry out the initial experimental tests with pseudo-thermal light sources rather than with real thermal light sources. Pseudo-thermal light sources are commonly realized by diffuse scattering of laser light by a rotating ground glass disk [22, 46, 47] or by emulsions (e.g., milk [66]). Rotating a disk or allowing the suspended scattering particles to experience Brownian motion one can observe a constantly (or discretely) changing specular pattern. Each realization of this pattern has exponential distribution of intensity. However multiple realizations of the specular patterns have Poissonian character. It is easy to see that a composition of these two statistics leads to a statistic of single-mode thermal light source. This source *effective* optical bandwidth is determined by the Doppler broadening due to the scatterers motion, and can be made arbitrarily narrow. This allows experimentalists to achieve the narrowband regime (see the SNR section for the definition) even with slow detection technologies, such as e.g. CCD cameras. This reduces the cost of the experiment by orders of magnitude, comparing with equal-size array of high-bandwidth detectors, while allowing for the same series of conceptual experimental tests.

Our pseudo-thermal light source shown in Fig. 37 consisted of a 532 nm laser pointer and a slowly rotating ground-glass disk. To achieve single-mode operation, the light has been passed through a polarizer before the disk. Furthermore, to achieve Gaussian intensity distribution of the source, the laser beam was spatially filtered by passing through a single-mode optical fiber. In a later modification, the fiber was replaced by a mode cleaner

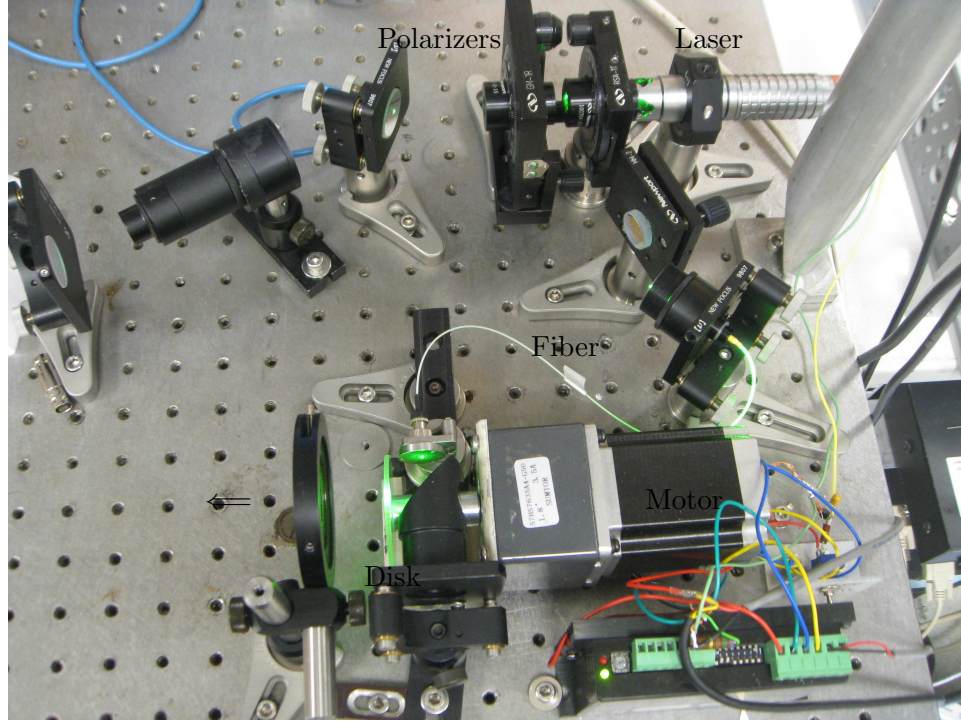


FIG. 37: Pseudo-thermal light source with a 532 nm laser pointer, built for our experimental demonstration.

consisting of two strong confocal lenses with a 20 micron pinhole in the focal spot, and an extra polarizer with the same orientation was added after the scatterer disk to suppress depolarization effects.

We have studied the statistical intensity distribution produced by our source using a Thorlabs CCD camera DCU224M. This is an 8-bit monochrom 1280×1024 camera with 4.65×4.65 micron pixel size. The camera has advanced configuration control which allows for adjusting the gamma-function and disabling the auto-gain and other “features” preventing linear operation of most off-the-shelf CCD cameras. Prior to performing measurements with our pseudo-thermal light source we verified the camera’s linear response by illuminating it through a pair of polarizers and ensuring the cosine character of the camera’s response to the angle between the polarizers. Hence the linear power response of our detector array with discretized dynamic range extending from 0 to 255 was verified.

The pixel-value histograms observed with this camera and our pseudo-thermal light source (in the stationary speckle field regime when the disk is not rotating) are shown in Fig. 38. In these measurements we fixed the optical power and changed the camera exposure from 0.5 to

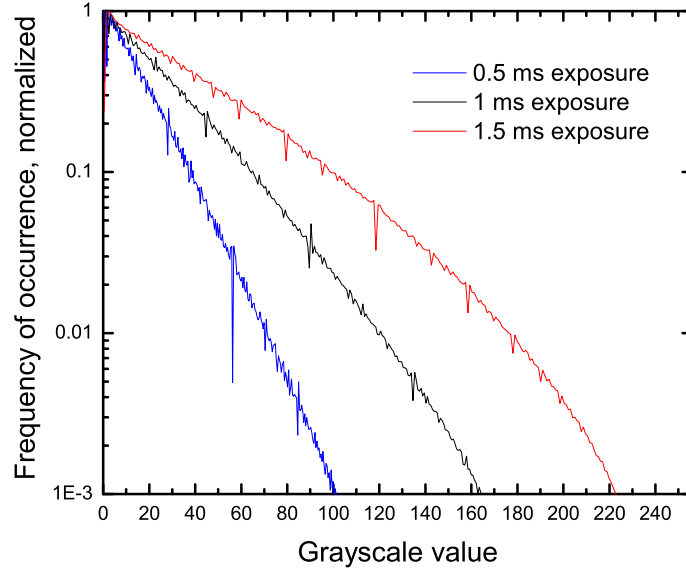


FIG. 38: Histograms of the grayscale pixel values of the CCD camera illuminated by a pseudo-thermal light source. Each data set is taken for 1000 frames with the same source power but different exposure times: 0.5, 1, and 1.5 ms. The run average was 14.7, 28.3 and 41.0, respectively.

1.0 and 1.5 ms, which has lead to different array averages: 14.7, 28.3 and 41.0, respectively. We observed that for low-average exposures the distribution remains exponential with a very high accuracy. For higher-average exposures saturation effects at high pixel values are evident. However their fractional weight is low, as one can see from Fig. 38. Nonetheless we tried to carry the following measurements with low frame averages in order to minimize the saturation effects.

It should be mentioned that averaging multiple speckle fields, we have not been able to achieve the expected value of the Glauber correlation function $g^{(2)}(0) = 2$. The values we achieved were 1.89, 1.82, 1.84 for 0.5, 1.0 and 1.5 ms exposures, respectively. The reasons for this discrepancy are not clear to us. Let us point out, however, that the single-mode illumination is not a necessary condition for the thermal light intensity interferometry imaging. In fact, the broadband regime discussed above is an extreme example of the opposite situation when $g^{(2)}(0) - 1 \ll 1$. Therefore not reaching the theoretical value of $g^{(2)}(0) = 2$ should not hinder our experiment.

The next important step necessary before carrying out the experimental demonstration is

to determine how much averaging of random speckle patterns is required in order to emulate uniform illumination with a thermal light source. The necessity to perform a massive frame averaging is the downside of using a pseudo-thermal light source instead of a real thermal light source. To perform this analysis a specialized Labview program was written which runs multiple averaging cycles with different numbers of frames. The frames are captured at 15 fps and processed in real time. For each measurement cycle, the program computed the correlation observable (10) as

$$G_{AC}^{(2)}(x, y) \equiv \langle I(x, y)I(-x, -y) \rangle - \langle I(x, y) \rangle \langle I(-x, -y) \rangle. \quad (98)$$

In (98) the average is taken over the camera frames (instantaneous speckle patterns), and x, y denote the pixel position relative to the frame center. The program then excluded the results from within a vicinity of the source speckle, i.e. such that $\sqrt{x^2 + y^2} < 6 \times (\text{speckle width})$, and computed the variance for the rest of the $G_{AC}^{(2)}$ array. This variance is plotted as a function of the number of averaged frames as shown in Fig. 39.

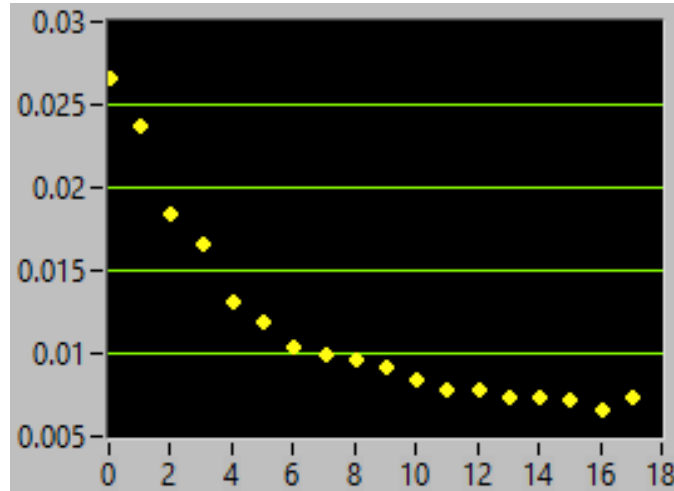


FIG. 39: A screen shot of the Labview program analyzing the variance of the background $G_{AC}^{(2)}$. The graph shows the variance vs. the number of averaged frames (in thousands).

For a true thermal source this variance in Fig. 39 should approach zero. In our measurement, however, we see that the averaging stops improving (or the improvement dramatically slows down) after some 15,000 frames at the level of approximately 7×10^{-3} . Considering the run average $\langle \langle I(x, y) \rangle \rangle_{x,y} \approx 15$ this corresponds to the normalized variance of approximately 3×10^{-5} . Therefore the correlation observable measured with this technique will remain

“grainy” at this level. Applying a threshold discussed in the context of Figs. 29 and 34 of the previous Section will be necessary. This threshold will limit the image reconstruction quality as illustrated in Fig. 34.

For the first attempt of 2D image reconstruction we used the object shown in Fig. 40(a). This metal object, named “the object 1”, had the full height (the vertical size in Fig. 40) of approximately 4 mm. It was suspended on four thin (few tens of microns in diameter) Kevlar threads inside of a large frame placed at $L = 191.1$ cm from the CCD camera array and $L_s = 88.9$ cm from the source. The source was a Gaussian light spot on a rotating ground-glass disk (Thorlabs, part number DG20-220), of the radius $R_s = 2.15$ mm. The object was centered on the line of sight, as evident from the shadow shown in Fig. 40(b). Thus from the CCD camera perspective, the object fits entirely into the brightest part of the source.

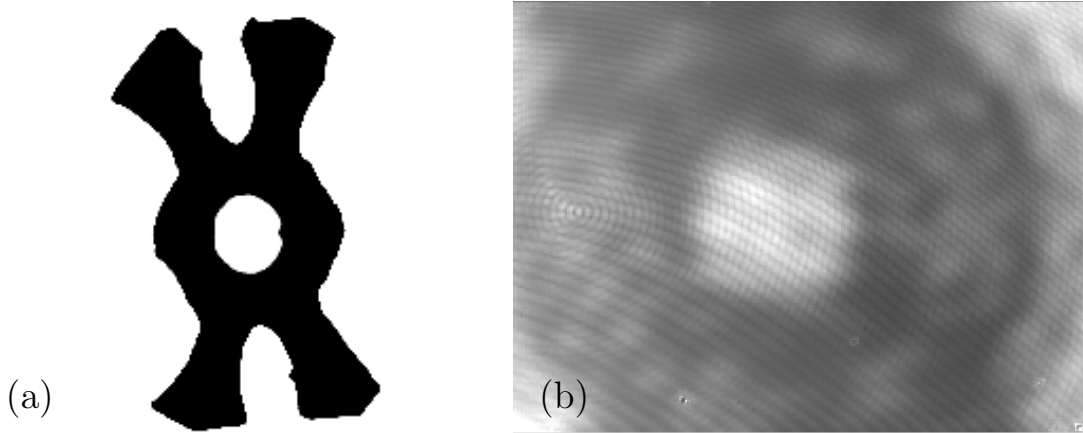


FIG. 40: A photograph of the “object 1” used for the first 2D image reconstruction experiment (a) and its shadow captured by the CCD camera (b).

The computed correlation observable $G_{AC}^{(2)}$ for the first experiment parameters is shown in Fig. 41(a), and the actual data is shown in Fig. 41(b). The agreement between the theory and experiment is superficial at best. The most evident discrepancies are in the shape of the central maximum and in the contrast of the side maxima. Moreover, the experimental data contains classically impossible values $G_{AC}^{(2)} < 0$, outlined with a yellow contour. Inside the red contour, the negative value drops below -5% of the peak value, reaching the value of -18% of the peak near the centers of the red-bordered dark regions.

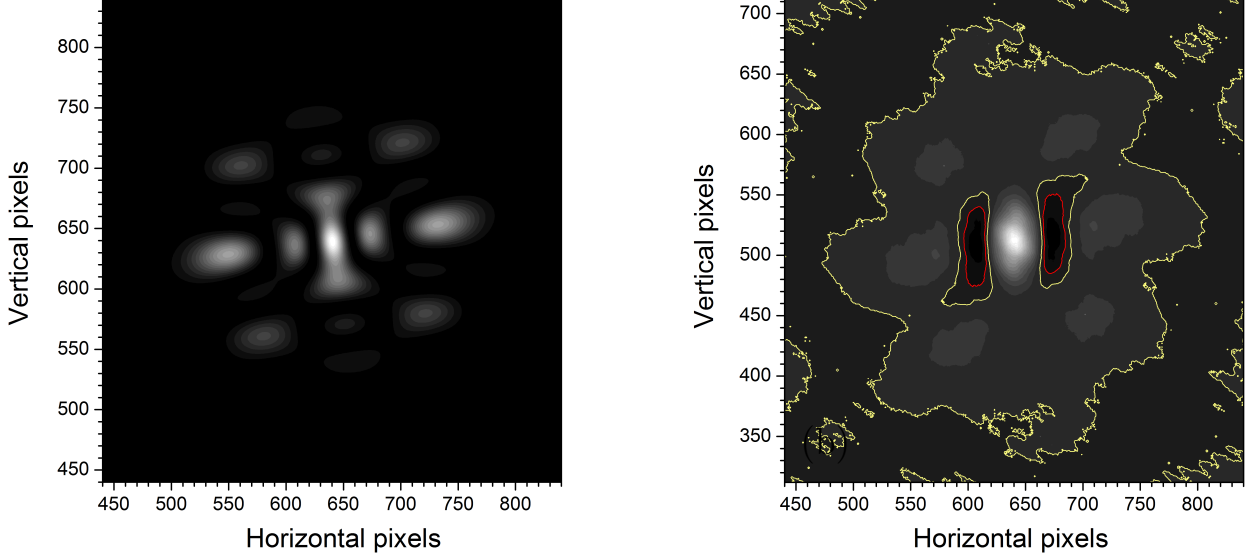


FIG. 41: The theoretical (a) and experimental (b) correlation observable $G_{AC}^{(2)}$ for the “object 1” from Fig. 40.

Clearly, these discrepancies far exceed the statistical variations. It is particularly puzzling that the negative (classically impossible) correlation peaks correspond to positive simulated peaks. One possible explanation could be that our “pseudo-thermal” light source does not properly mimic the thermal light source, which may happen e.g. if the optical field illuminating the object and the CCD camera retains significant spatial coherence. The presence of a family of concentric circular interference fringes centered near the left edge of Fig. 40(b) hints that this may be the case. In any event, while the theoretical correlation matrix plotted in Fig. 41(a) is adequate for successful Gerchberg-Saxton image reconstruction, experimental data from Fig. 41(b) does not lead to a successful reconstruction.

To investigate the failure of the object 1 imaging we decided to first study a one-dimensional case which allows for easier numeric analysis. It also allows us to combine the frames average with the average over the rows of pixels, i.e. $\langle \dots \rangle_y$, and to collect high-quality data faster. Therefore instead of (98) we construct the observable as

$$\langle G_{AC}^{(2)}(x) \rangle_y = \langle \langle I(x, y) I(-x, y) \rangle - \langle I(x, y) \rangle \langle I(-x, y) \rangle \rangle_y. \quad (99)$$

A diagram of our first 1D experiment is shown in Fig. 42. In this experiment we realized one of the most traditional settings in interferometry: a double-slit mask. Analysis of this experiment is very simple. We first notice that the speckle size produced by the source on

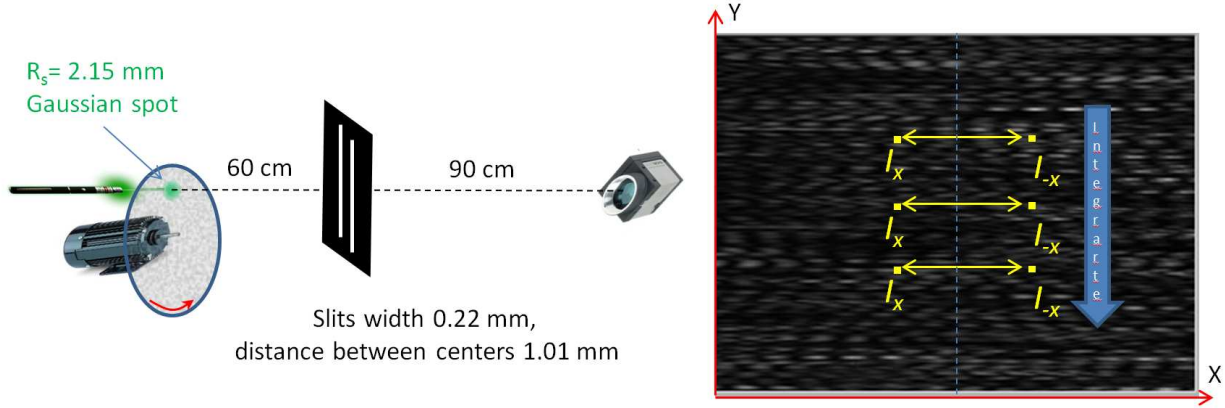


FIG. 42: A diagram of a double-slit experiment with pseudo-thermal source of light and the instantaneous speckle pattern observed in this experiment. The drawing on the pattern explains how the additional pixel rows averaging is performed in 1-D measurements.

the mask is much smaller than the mask feature (the slit width). Therefore the mask itself can be considered as a secondary pseudo-thermal source of light. Its correlation function in the far field obeys the earlier-mentioned van Cittert-Zernike theorem, leading to

$$\langle G_{AC}^{(2)} \rangle_y \propto \cos^2 \left(\pi b \frac{x_2 - x_1}{\lambda L} \right) \text{sinc}^2 \left(\pi a \frac{x_2 - x_1}{\lambda L} \right), \quad (100)$$

where a and b are the slits width and centers separation, respectively.

We have used Eq. (100) to compute the theoretically curve shown in Fig. 43(a). No free fitting parameters have been used. However a careful collimation of the laser beam incident

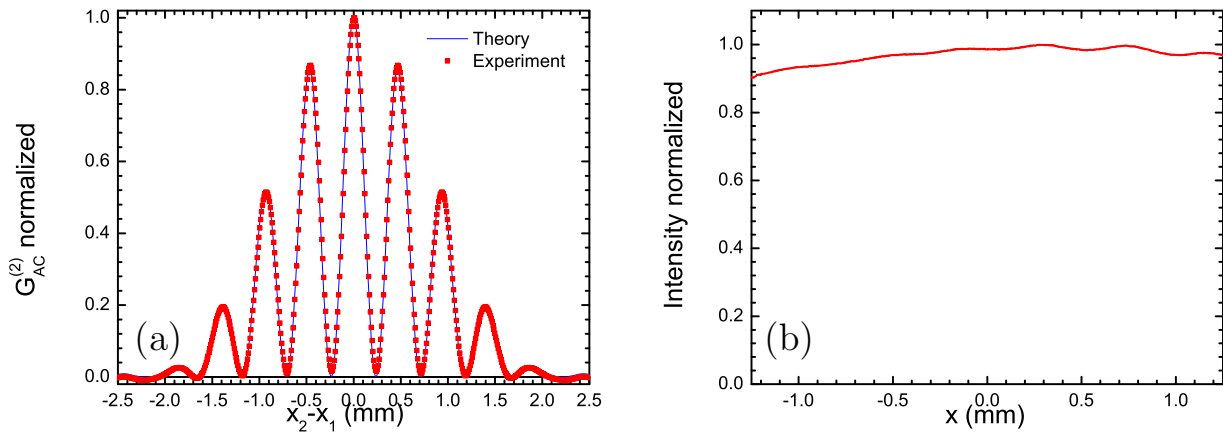


FIG. 43: Normalized correlation function (a) and intensity distribution (b) observed in experiment shown in Fig. 42.

onto the ground glass disk was required in order and to eliminate the first-order interference fringes and to achieve relatively uniform intensity distribution shown in Fig. 43(b). These fringes indicate the presence of the transverse coherence, which has been the prime suspect for arising the negative $G_{AC}^{(2)}$ regions in the experimental results from Fig. 41(b).

Perfect agreement between the theory and experiment in Fig. 43(a) validates our understanding of the physical principles behind the model. To also verify the “speckle of darkness” concept which is directly relevant to the imaging of dark objects by intensity interferometry, we inverted the setup in Fig. 42 and used a double-wire mask instead of a double-slit mask, as shown in Fig. 44. In this case, again, we do not observe any tell-tale shadow, see Fig. 45(b), while the intensity correlation function is well resolved, see Fig. 45(a).

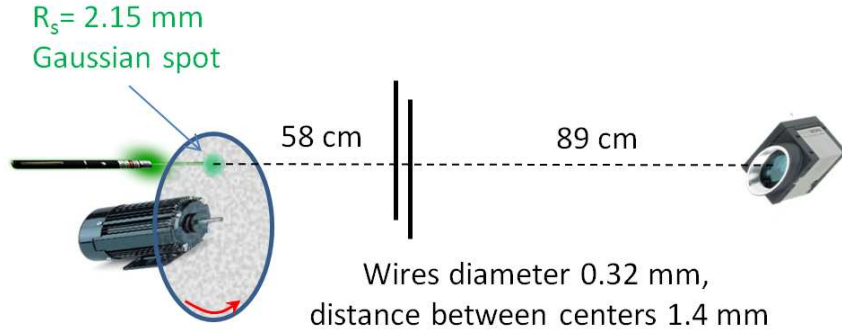


FIG. 44: A diagram of a double-wire experiment with pseudo-thermal light source.

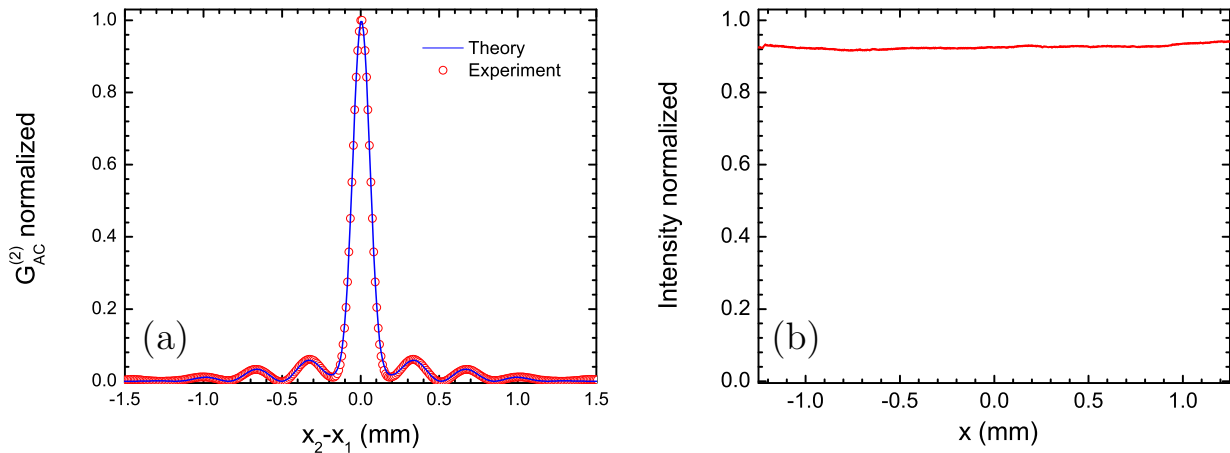


FIG. 45: Normalized correlation function (a) and intensity distribution (b) observed in experiment shown in Fig. 44.

In Fig. 45(a) we see a central maximum which is due to both the source and the mask, and the secondary maxima that are solely due to the mask. The theoretical description of this structure requires a source (Gaussian) term to be added to the right-hand side of Eq. (100). The relative weights of these two terms need to be determined. It is important to point out that using Eq. (43) for this purpose leads to the theoretical estimate of the mask signature exceeding the experimental observation by a factor of several. Using a more complex model of Eq. (41) accounting for the object and source convolution, however, leads to the perfect consistency. This indicates that the assumption (42) is not sufficiently well fulfilled in our experiment, which likely has been another reason for the failure of the first 2D imaging experiment. Using the source-convolution model of Eq. (41) for our double-wire mask entailed, first, scaling the relative visibility of the mask signature by the square of the local intensity of the source at the point found by drawing a line through the CCD camera center and either one of the wires. Secondly, the rows averaging has to be done with a weight which is found by a similar procedure.

The source-convolution model predicts a strong reduction of the object's signature visibility as the object is moved away from the line of sight. Indeed, for our double-wire mask this means that each wire is effectively illuminated with a different intensity. As with a normal double-slit interferometer, this would lead to the loss of the fringes contrast. To verify this conjecture, we shifted the double-wire mask by 1 mm in perpendicular to the wires direction. Then instead of Fig. 45(a) we observe the intensity interference fringe shown in Fig. 46. A dramatic reduction of the object's fringes is evident.

The important role of the source intensity distribution when assumption (42) is only weakly satisfied suggests that using a disk-like source with uniform intensity distribution is better than using a Gaussian source. A disk also serves as a better model for stellar light sources. To achieve this in the experiment, we included in our pseudo-thermal light source a flat-top laser beam shaper, an instrument sold by the Edmunds Optics which is designed specifically to focus a Gaussian beams into a uniform disk spot.

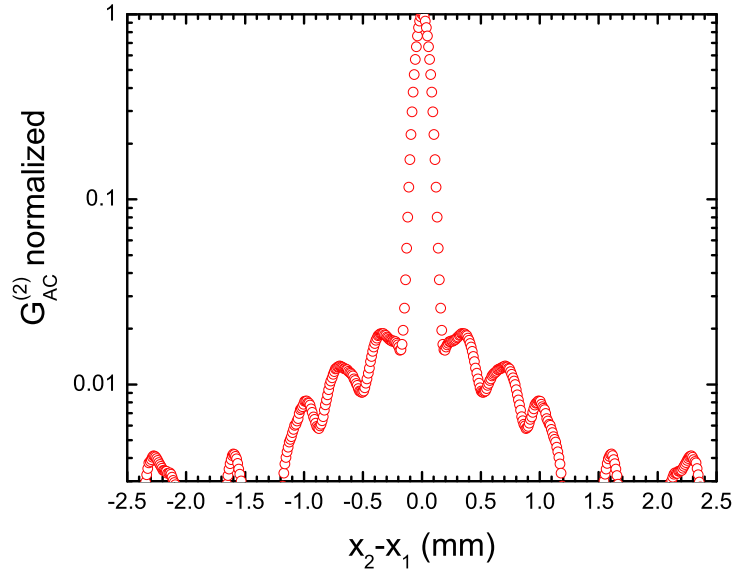


FIG. 46: The same correlation function as in Fig. 45(b) after the mask has been shifted by 1 mm across the line of sight.

With this beam shaper in place and projecting a light disk-shaped spot onto the rotating diffuser, we proceeded to the second 2D imaging demonstration. In this experiment we used a small image of the International Space Station printed on a glass plate, as shown in Fig. 47. The mask size, source diameter and distances L_s and L are chosen such that the effective source intensity is the same for any point of the mask (in other words, a line drawn through the CCD camera center and any point of the mask always ends within the source disk).

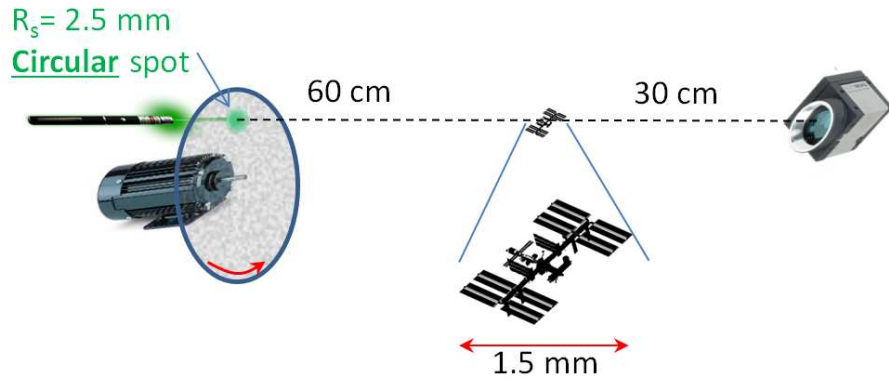


FIG. 47: A diagram of a 2D imaging experiment with a disk-shaped pseudo-thermal light source.

The correlation observable obtained after averaging of 1.3 million frames is shown in Fig. 48(a). Fig. 48(b) shows a computed correlation observable. As an improvement from the first 2D imaging experiment, now there is a strong similarity between Figs. 48(a) and (b), which allows us to claim consistency between the theory and the experiment in the 2D case. However, in spite of the massive averaging, the experimental data has background (additive) noise at the level of 1%. In particular this noise leads to the classically impossible values of $G_{AC}^{(2)} < 0$ marked red in Fig. 48(a).

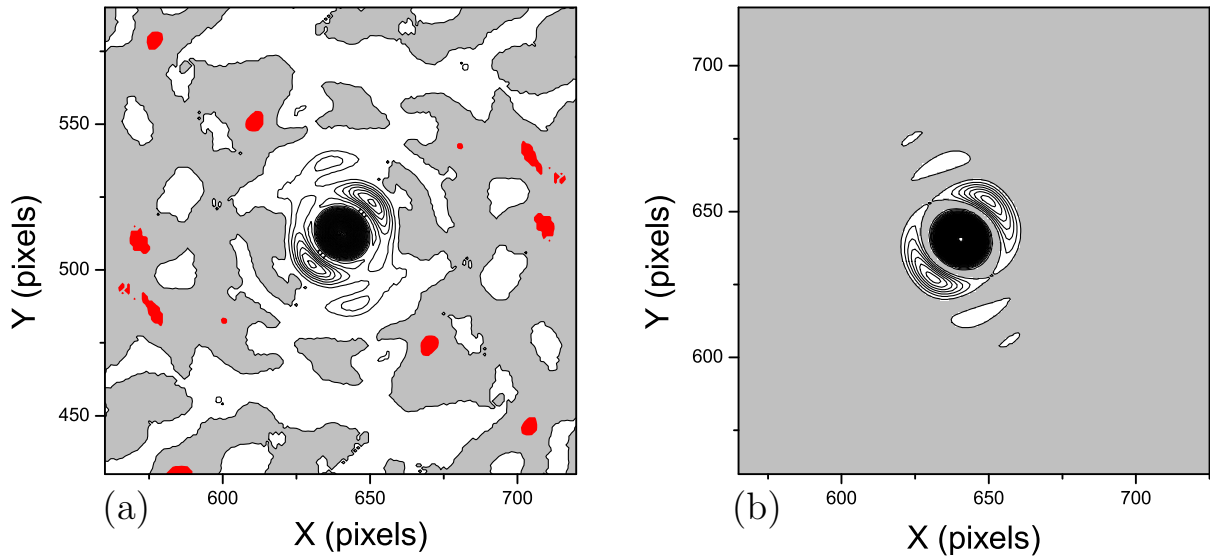


FIG. 48: Measured (a) and computed (b) correlation observables $G_{AC}^{(2)}$ in the ISS imaging experiment (see Fig. 47). Each contour line corresponds to 1% increment.

The computed noiseless $G_{AC}^{(2)}$ shown in Fig. 48(b) is more than adequate for quick and high-quality reconstruction of a 152×152 -pixel ISS image which has approximately 40 micro radians angular resolution, see Fig. 49 and Fig. 50. This resolution is determined by the CCD array size and the distance L , as has been discussed in the previous Section.

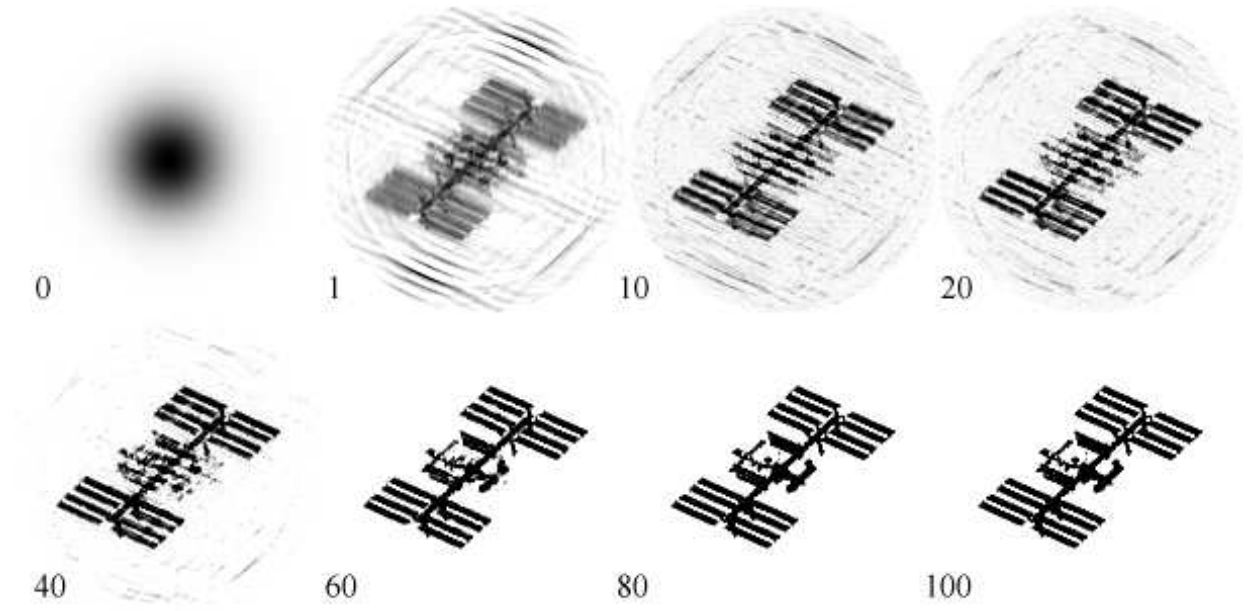


FIG. 49: The image reconstruction steps for the computed noiseless ISS correlation observable shown in Figs. 48(b). Step numbers are given in the lower left corner of each frame.

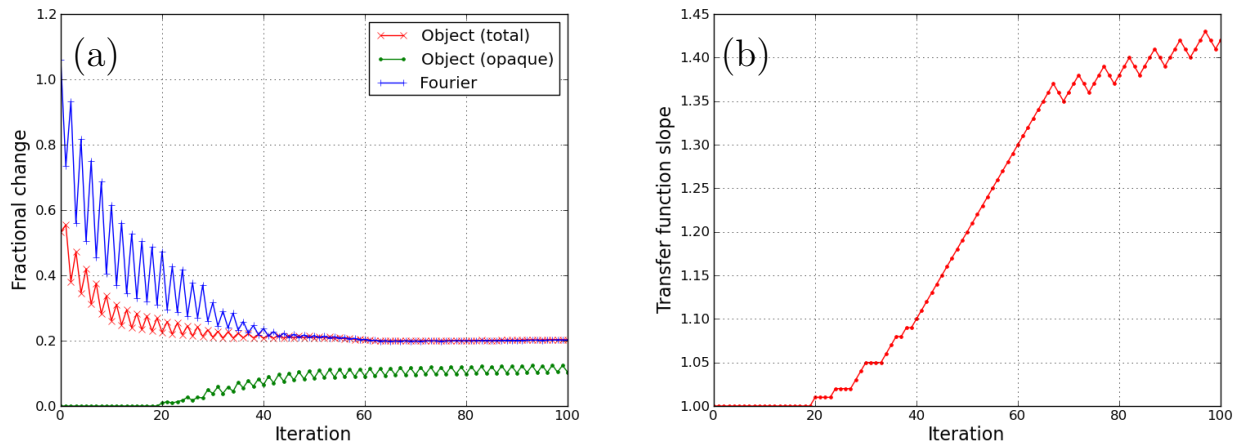


FIG. 50: The object variances (96) (a) and the transfer function slope (b) during the image reconstruction process in Fig. 49.

However, having added to the computed correlation observable Gaussian noise at the level of 1% to simulate the experimental data, we have not been able to recover the image. Fig. 51 shows the result of image recovery attempt for the threshold set at 2% level (an optimized value removing most of the noise but preserving most of useful signal). Other

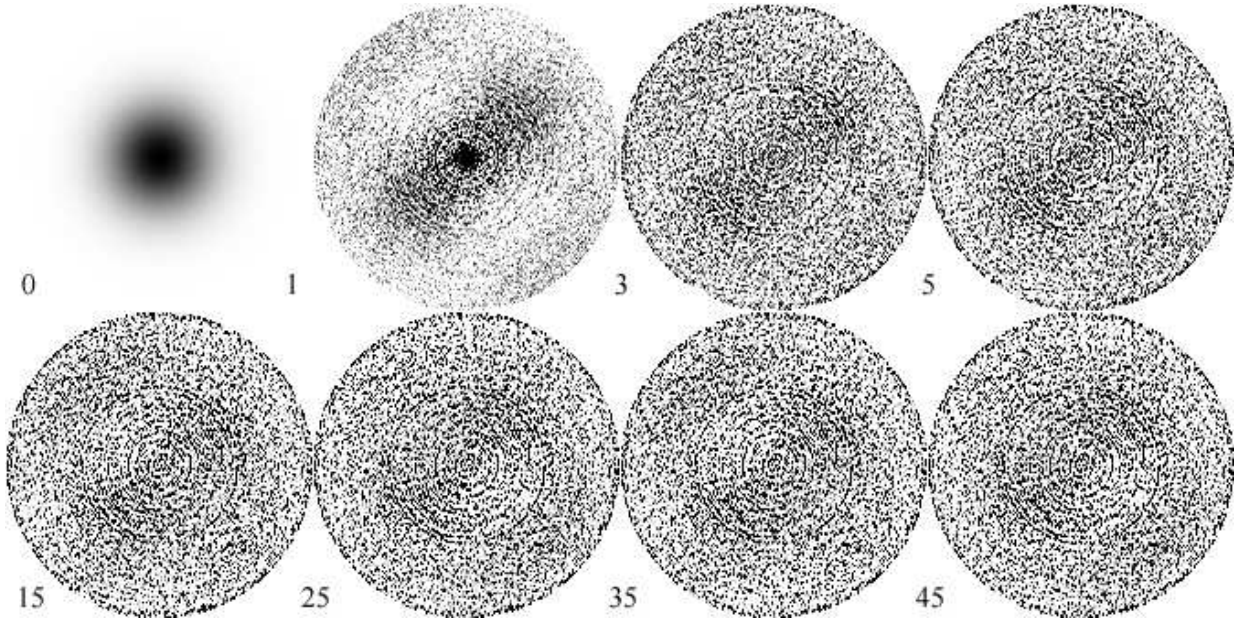


FIG. 51: A failed attempt to reconstruct the ISS image from the computed correlation observable shown in Figs. 48(b) in presence of 1% additive noise with Gaussian distribution. The threshold is set at 2%. Step numbers are given in the lower left corner of each frame.

threshold values likewise did not lead to success. It is not surprising therefore that recovering the image from the experimental data shown in Fig. 48(a) also failed.

It should be noted that the background noise observed in this measurement exceeds the expectations based on the averaging test reported in Fig. 39 by more than an order of magnitude. To investigate this problem, we have carried out a reference measurement with the ISS mask removed, averaging 1.1 million frames. The average intensity and correlation observable from this measurement are shown in Fig. 52. The intensity distribution shows some 10% contrast interference fringes due to the bandpass interference filter, polarizers and other parallel surfaces. It also shows the shadows due to dust particles on the optics and on the CCD array. These features however should not affect the correlation observable by the virtue of its construction, see Eq. (98). The correlation observable in Fig. 52(b) features the “grainy” structure at the same level as in Fig. 49(a). This structure has a characteristic scale comparable to the source speckle size. This may indicate that one possible origin of this noise is a stationary scatter which produces speckles that do not average during data collection.

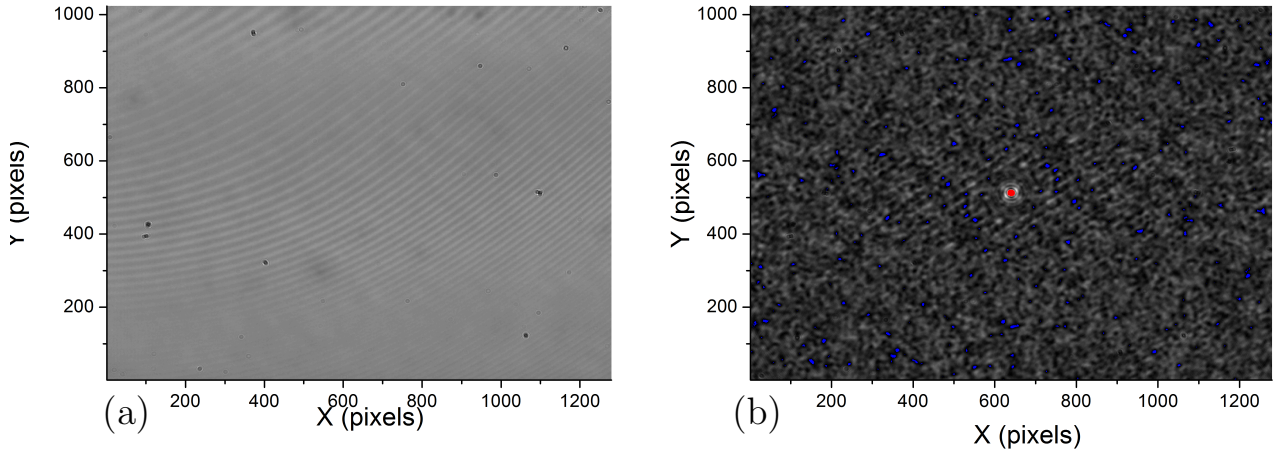


FIG. 52: The mean intensity distribution (a) and correlation observables (b) in the reference measurement (with the ISS mask removed). The grey scale in (b) spans the range of 0 to 5%; values below zero are given in blue, above 5% in red.

Further experimental research focused on demonstration of the 2D intensity interferometric imaging with a pseudo-thermal light source should include solving the additive noise problem as well as development of improved, noise-resilient image-reconstruction algorithms. Developing such algorithms can leverage the techniques used in quantum optics for the quantum state tomography [67].

This work will have to be continued outside the scope of this NIAC effort. It has been included in the NASA-APRA proposal (Proposal Number: 13-APRA13-0032) submitted by our team in May 2014 which is presently under consideration. The experimental part of this 3-year, \$1M proposal goes beyond using the pseudo-thermal light source and includes lab and field demonstrations with actual thermal light source and high-speed detectors. Using a true thermal light source will not only advance the project towards its practical goals, but also eliminate the averaging-related difficulties which have been proven significant. We have already determined the suitable commercially available instrumentation, which includes a Hamamatsu L233-55NB light source and 45 GHz bandwidth Newport 1014 detectors coupled to Millitech LNA-22-02060 amplifiers and MXP-28-RFSFL balanced mixers to implement high-speed signals multiplication. The integrated signals will be acquisitioned by a DAQ board such as e.g. National Instruments model 781047.

F. On observation of phase objects

Phase objects are the objects that refract light without absorbing it. Such hypothetical objects provide a useful model for many astrophysical phenomena related to gravitational lensing and microlensing [68, 69], and interstellar phase screens due to cold gas clouds [38, 39]. They also may be useful for investigating remote atmospheric phenomena and for other applications. Therefore there is a strong motivation for high-resolution optical imaging of phase objects by means of intensity interferometry. However, best to our knowledge, this problem has not been discussed yet.

One model phase object allowing for the fully analytical treatment in the framework of Eqs. (22) and (23) is a thin lens. For an infinitely large thin lens characterized by the focal distance f , (23) yields

$$S(\vec{x}, \vec{y}) = e^{-\frac{ik}{2f}(\rho_o^2 - \rho_o'^2)} = e^{-i\frac{k}{f}\vec{x}\vec{y}}. \quad (101)$$

When this is substituted into (22) we see that the effect of such a lens can be absorbed into $\gamma \rightarrow \gamma_f = k(1/L + 1/L_s - 1/f)$. Then we quickly arrive to

$$\begin{aligned} G_{11} = G_{22} &= \frac{q^2}{\pi D^2} = \text{const}|_{\vec{\rho}_{1,2}}, \\ G_{12}(\vec{\rho}_1, \vec{\rho}_2) &= \frac{q^2}{\pi D^2} e^{\frac{ik}{2L} \frac{D-1}{D}(\rho_2^2 - \rho_1^2)} e^{-(q/D)^2 |\vec{\rho}_2 - \vec{\rho}_1|^2}, \\ g_{12}(\vec{\rho}_1, \vec{\rho}_2) &= 1 + e^{-2(q/D)^2 |\vec{\rho}_2 - \vec{\rho}_1|^2}, \end{aligned} \quad (102)$$

where $D \equiv L(1/L + 1/L_s - 1/f)$ is a dimensionless “out-of-focus” factor. If the lens *images the source plane onto the detector plane*, then $D = 0$ and the speckles become infinitely small while the intensity goes to infinity. The former is a consequence of the thermal field statistics (11). The latter is a consequence of the paraxial approximation leading to the coordinate-independent intensities in (102).

On the other hand, if the source is in focus, $D = 1$, then the light propagates as a collimated beam and the speckle size as well as the intensity in the detector plane will be the same as in the lens plane. These two test cases validate our general approach to phase objects.

For more complex phase objects we need to follow more advanced theoretical analysis explained earlier in this Chapter. However the approximation (37) cannot describe a phase object. We have to retain one more term in the power expansion series, which yields

$$T^*(\vec{\rho}')T(\vec{\rho}'') = e^{i[\phi(\vec{\rho}'') - \phi(\vec{\rho}')] } \approx e^{i\vec{\rho}_d' \vec{\nabla} \phi(\vec{\rho}_s')}. \quad (103)$$

In (103) we make our usual approximation that the speckle size the source casts on the object is much smaller than the object feature, and define $\vec{\rho}_d' \equiv \vec{\rho}'' - \vec{\rho}'$, $\vec{\rho}_s' \equiv (\vec{\rho}'' + \vec{\rho}')/2$. For the correlation observable this leads to

$$\langle E_1^*(\vec{\rho}_1) E_2(\vec{\rho}_2) \rangle = \frac{e^{\frac{ik}{L} \vec{\rho}_s \vec{\rho}_d}}{(\lambda_s L L_s)^2} \int_O d^2 \rho_s' d^2 \rho_d' \int_S d^2 \rho I_s(\vec{\rho}) e^{\frac{ik}{L} \vec{\rho}_s' \vec{\rho}_d'} e^{i \vec{\rho}_d' \vec{\nabla} \phi(\vec{\rho}_s')} e^{-\frac{ik}{L_s} \vec{\rho} \vec{\rho}_d'} e^{-\frac{ik}{L} \vec{\rho}_s \vec{\rho}_d'} e^{-\frac{ik}{L} \vec{\rho}_d \vec{\rho}_s'}, \quad (104)$$

where again $\vec{\rho}_d \equiv \vec{\rho}_2 - \vec{\rho}_1$, $\vec{\rho}_s \equiv (\vec{\rho}_2 + \vec{\rho}_1)/2$. As before, we will assume that the correlation function is measured symmetrically around the line of sight: $\rho_s \equiv 0$. In (104) the inner integral is taken over the source and the outer integrals are taken over the object. Of the latter, the $d^2 \rho_d'$ integral yields a 2-dimensional Dirac δ -function which, when integrated over the source plane, shifts the argument of $I_s(\vec{\rho})$. This yields

$$C(\vec{\rho}_d) \approx K \left| \int d^2 \rho_s' I_s \left[\beta \vec{\rho}_s' + \frac{L_s}{k} \vec{\nabla} \phi(\vec{\rho}_s') \right] e^{-\frac{ik}{L} \vec{\rho}_d \vec{\rho}_s'} \right|^2. \quad (105)$$

We recognize (105) as a Fourier-transform of the source intensity distribution *with a shifted argument*, which can be viewed as a generalized van Cittert - Zernike theorem. For a sufficiently smooth phase object it is reasonable to treat $\phi(\vec{\rho}_s')$ as a polynomial with decreasing higher-order terms. Remarkably, the zeroth-order term is removed by the gradient: the overall phase is not observable in this type of measurement, which is physically reasonable. The linear phase term (such that may be produced by an optical wedge) yields a constant argument shift in $I_s(\vec{\rho})$ which amounts to an apparent shift of the object from the line of sight, or equivalently, a phase shift of its Fourier transform. Since our observable is phase-insensitive, this effect vanishes as well.

The next-order, quadratic, contribution leads to the already studied case of a thin lens with a focal distance f . For such a lens $\vec{\nabla} \phi(\vec{\rho}_s') = -\vec{\rho}_s' k/f$, so it has the effect of linear scaling of the intensity argument: $\beta \vec{\rho}_s' \rightarrow (\beta - L_s/f) \vec{\rho}_s'$, which can be viewed as a change in the effective propagation distance: $L_s + L \rightarrow L_s + L - L_s L/f$. In particular, when $1/L + 1/L_s = 1/f$, this distance becomes zero. This of course corresponds to imaging of the source onto the detection plane, in which case we recover our initial assumption of δ -correlation of the thermal source field as has been shown earlier.

Analysis of the higher-order phase terms is less intuitive. However we can already see that the problem of reconstructing a phase object can be reduced to recovering a source intensity distribution from its Fourier transform absolute square, and then taking the inverse

of the result in order to retrieve the object signature. The following example is designed to demonstrate the first step, while the second step is intentionally made trivial.

Let the source have Gaussian intensity distribution $I_s(\rho) = \exp(-\rho^2/R_s^2)$ with $R_s = \sqrt{0.1}$ cm. Consider a thin lens with a focal length $f=11.36$ cm centered on the line of sight between the source and detectors array so that $L = L_s = 50$ cm. As a phase object, we take a rectangular $x = 0.118$ cm by $y = 0.25$ cm piece of this lens centered at $\Delta_x = 0.293$ cm from the line of sight, and remove the rest of the lens. Then, according to (105), the source argument is linearly scaled within the rectangle, and unperturbed elsewhere. The resulting modified intensity is shown in Fig. 53(a).

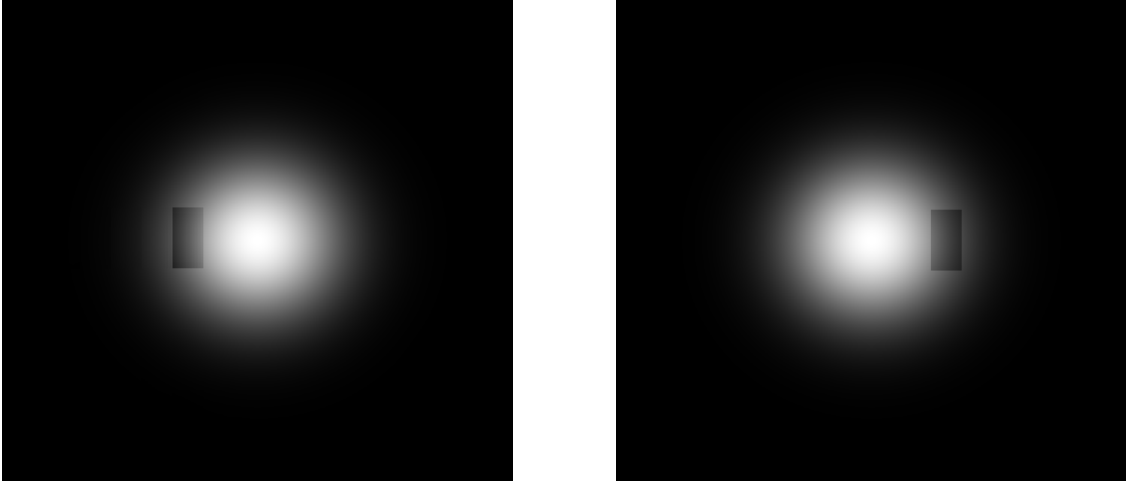


FIG. 53: Numerically modeled intensity distribution of a Gaussian source modified by a rectangular phase object (a) and its reconstruction by Gerchberg-Saxton algorithm after 5000 iterations (b). Side of each image is 2 cm, array size 680 x 680 pixels.

Our phase object reconstruction algorithm is similar to the algorithm we used for the absorbing objects, except that now we abandoned constraints 2 and 4, and set the upper limit to the unperturbed intensity function rather than unity in constraint 3. This considerably weakened our set of object constraints, and the image reconstruction took significantly longer. The reconstruction result obtained after 5000 iterations is shown in Fig. 53 (b). While the image turned out inverted, it has adequate fidelity.

In this example we assume that we have *a priori* knowledge that the object is a rectangular piece of a thin positive lens. To characterize the phase object we therefore use the

reconstructed source function $I_G(\rho)$, in the area G of the phase object (the dark rectangle in Fig. 53) in the form $I_G(\rho) = \exp(-[\rho(\beta - L_s/f)]^2/R_s^2)$. We fit it to find f . The fitting yields $f_{out} = 11.37$ cm with the standard deviation $\sigma_f = 0.19$ cm, which is in remarkable agreement with the input value $f = 11.36$ cm.

Though it may seem artificial, the example with a piece of lens will prove helpful in the following analysis. We already mentioned that in general, finding the inverse function of the source intensity $I_s(\vec{\rho})$ after Gerchberg-Saxton reconstruction of this function would be required. This can be done e.g. when the phase gradient is strong enough to distort the source by more than its angular size, that is, when

$$D_s \ll \frac{L_s}{k\beta} \left| \vec{\nabla} \phi(\vec{\rho}_s) \right|_{min}. \quad (106)$$

In (106) the subscript *min* indicates the minimum absolute value of the phase gradient that we wish to resolve. In this case we can treat $I_s(\vec{\rho})$ as a δ -function, which makes the inversion trivial:

$$\vec{\nabla} \phi(\vec{\rho}) = -\frac{k\beta}{L_s} \vec{\rho} = -\left(\frac{1}{L_s} + \frac{1}{L} \right) k\vec{\rho} \quad (107)$$

for the regions G of $\vec{\rho}$ where $I_s(\vec{\rho})$ is a non-zero constant, and $\vec{\nabla} \phi(\vec{\rho}) = 0$ everywhere else. It is easy to see that this corresponds to the region G “filled” with a lens centered on the line of sight such that it would image the (point-like) source onto the detection plane: $1/f = 1/L_s + 1/L$. This is the best estimate of the phase object that we can achieve with the approximation of Eq. (103). Even though a linear phase gradient such as (107) is not a suitable model e.g. for gravitational lenses, it is possible that this model can distinguish single from multiple phase objects with high resolution.

Clearly, the study of phase objects reconstruction from intensity interferometry data needs to be continued. One of open questions in this field is to what extent finding of the inverse function is possible when the source is not too small or the phase gradient is not too strong, that is, when inequality (106) is not strictly enforced. It may be possible to leverage additional consideration, such as that the phase gradient function is smooth and takes the smallest of possible values, to approximately invert the reconstructed $I_s(\vec{\rho})$ and to find $\vec{\nabla} \phi(\vec{\rho})$. This research has been proposed to JPL’s Research and Technical Development Program as a topic area concept for FY 2015 funding, which is presently being evaluated.

IV. DISSEMINATION AND OUTREACH

An important goal of NASA's innovative research programs is to facilitate the transfer of NASA technology and engage in partnerships with other government Agencies, industry, and international entities to generate U.S. commercial activity and other public benefits. Also, as a Federal Agency, NASA requires prompt public disclosure of the results of its sponsored research to generate knowledge that benefits the nation. Thus, it is the NIAC's intent that all knowledge developed under its sponsorship be shared broadly by means of publishing the research results in peer-reviewed, publicly accessible journals to the greatest extent practical. In response to these requirements, we reported our research results in the following peer-reviewed papers:

- *Ghost Imaging of Space Objects*, D.V. Strekalov, B.I. Erkmen and N. Yu, Journal of Physics, Conf. Series, **414**, 012037 (2013).
- *Intensity interferometry for observation of dark objects*, D.V. Strekalov, B.I. Erkmen and Nan Yu, Phys. Rev. A **88**, 053837 (2013).
- *Imaging dark objects with intensity interferometry*, D.V. Strekalov, I. Kulikov, and N. Yu, Opt. Expr. **22**, 12339-12348 (2014).

Our results have also been reported at the following conferences:

- *Ghost imaging of space objects*, D.V. Strekalov, B.I. Erkmen, and N. Yu, 21th International Laser Physics Workshop, Calgary, Canada, July 23-27 (2012) (*Invited talk*).
- *On using intensity interferometry for feature identification and imaging of remote objects*, Baris I. Erkmen, Dmitry V. Strekalov, and Nan Yu, SPIE meeting, San Diego, California, United States, August 25-29 (2013).
- *Intensity interferometry for imaging dark objects*, Dmitry Strekalov, Baris Erkmen, Igor Kulikov and Nan Yu, Workshop on Hanbury Brown and Twiss interferometry, Nice Observatory (Nice, France), May 12-13 (2014) (*Invited talk*).
- *Imaging Dark Objects by Intensity Interferometry*, D.V. Strekalov, I.K. Kulikov and N. Yu, 23-d International Laser Physics Workshop, Sofia, Bulgaria, July 14-18 (2014) (*Invited talk*).

Besides the regular conferences attendance, the PI was invited to deliver a lecture on this research topic at Max Plank Institute for Physics of Light retreat in Ringberg castle in October 2012, and in July 2014. As one indication of successful dissemination of the new knowledge gained in this project, the PI has been asked to take a role of the Lead Guest Editor and to organize a special issue of the *Advances in Astronomy* journal dedicated to intensity interferometry. This activity is currently in progress.

At JPL, our research results have been reported at several Section-, Division- and Lab-wide presentations and published in the JPL's Interplanetary Network Progress Report 42-192, (February 15, 2013). A new IPN Report is currently being prepared. The innovative technical solutions developed in the course of this research have been disclosed in the following JPL's Novel Technology Report NTR 49465, *Intensity interferometry Image recovery*, submitted on February 12, 2014.

The NIAC program is viewed as a seedling program designed to validate a novel, revolutionary concept and to develop it to a sufficient level to become attractive for other NASA offices or for outside funding. Therefore a significant effort was made to secure the follow-on funding. The above-mentioned JPL meetings were partly focused on this goal. In addition to that, the following proposals have been submitted, see Table VI. Future proposal activity is also planned.

Title	Submitted	Agency (program)	\$\$ K	Status
Cross-band Ghost Imaging of Space Objects	August 2014	JPL (CIF)	100	Under consideration
Intensity interferometry for imaging dark objects in space	May 2014	JPL (RTD Concept)	200	Under consideration
Intensity correlation for imaging dark objects in space	March 2014	NASA (APRA)	992	Under consideration
Imaging of Spacecraft by Intensity Interferometry	August 2013	NRO (DII)	450	Program cancelled

TABLE VI: List of proposals submitted for follow-on funding.

V. CONCLUSION

To conclude this report, we would like to summarize that our “Ghost Imaging of Space Objects” NIAC research effort was successful. As anticipated, its main return has been the newly acquired knowledge and the understanding of the pathways that lead from this knowledge to its applications in observational astronomy. During this research we came across several fundamental insights that were not expected at the beginning. We came to realize that the ghost imaging of dark objects using background thermal light can be treated as a special case of Hanbury Brown and Twiss intensity interferometry in combination with the Babinet’s principle for higher-order observables. Extensive recent work performed in this field by other research groups worldwide might seem to detract from the conceptual originality and novelty of our approach; but at the same time it serves as an encouraging indication that the chosen approach is acknowledged in the broader science community as promising. This newly found synergy, acknowledged in the CTA newsletter from May 2014 reporting on the Workshop on Hanbury Brown and Twiss interferometry in Nice, makes us confident that our published and otherwise disseminated results will be integrated into a larger-scale on-going research effort aimed at performing astronomy observations of both bright and dark objects with unparalleled resolution.

While we are satisfied with acceptance of our results by the international research community as a contribution to the field of intensity interferometry as well as to the on-going mission-oriented projects, we also have been aiming at receiving support to continue and advance this research at JPL. Several proposals have been submitted in pursuit of this goal. Three of them are still under consideration, and we expect to learn about the funding decisions soon. These new projects would leverage the results of this NIAC study and extend it along well-defined directions that have been discussed above.

Shifting the main paradigm of our approach towards intensity interferometry entailed another important realization, that the actual *imaging* of dark objects, in a sense of mapping the column optical density distribution, is possible by using known numerical techniques, such as the Gerchberg-Saxton approach. This insight was also unanticipated in the beginning and caused a shift of the research focus from the initial plan. While this focus shift has been well-justified and fruitful, it has left several issues unexplored. Some of these issues, too, are included in the future research proposals.

First among such outstanding questions is the fundamental possibility and practical feasibility of ghost imaging in the transmitted-scattered configuration, such as shown in Fig. 4(a) and, in fact, on the title page of this Report. The study of this configuration has been deemed to have a low priority because of the difficulties and cost of its practical realization. However this study is still interesting from the fundamental point of view because it goes beyond the Hanbury Brown and Twiss measurement paradigm, and still may be feasible for the near-space objects. In this context, it might be interesting to study the scattered-scattered configuration, which completely eliminates the direct source light and therefore may feature increased SNR.

Another question, or rather a series of connected questions, to be studied in the future is related to other observables than the Glauber intensity correlation function (7) and its variants. One such alternative comes from generalization of Eq.(7) for higher powers m and n of the measured intensities. It has been shown [70] that this could lead to higher contrast images but perhaps with a worse SNR. The optimization of the powers m and n and discussion of the ensuing trade-offs is available in [43]. Applying this technique to our imaging architecture may potentially allow us to further increase the imaging contrast and background suppression. Another novel detection technique [47, 48] relies on measuring a *variance of the difference* of two detectors signal, rather than on photo counts coincidences (i.e., a product). Using correlation observables based on more than two detectors is yet another intriguing possibility [49, 50] which may be useful for the phase retrieval task. Obtaining the “closure phase” between the three detection points could assist or even substitute the numerically intensive and intrinsically ambiguous techniques such as Gerchberg-Saxton reconstruction. These alternative detection techniques may offer interesting trade-offs in terms of the resolution, SNR and instrument requirements, and therefore should be studied as a part of future development of this technology. It is important to point out that the analytical and numerical computations required for this study are going to be very similar to those we performed here. Indeed, the part of the analysis that describes the optical field propagation from the source to the detectors, and also includes the object’s model, will be the same. This is the most extensive and complex part of the analysis. Therefore it is indisputable that this research has successfully formed a theoretical foundation to the follow-on effort. We are also confident that it has succeeded in sparking enough interest to such follow-on study and technology development to make it imminent.

Acknowledgement: The research was carried out at the Jet Propulsion Laboratory, California Institute of Technology, under a contract with the National Aeronautics and Space Administration. Copyright 2014 California Institute of Technology. U.S. Government sponsorship acknowledged.

REFERENCES

- [1] J.J. Lissauer et al., *Nature* **470**, 53-58 (2011).
- [2] F. Fressin et al., *Nature* **482**, 195-198 (2011).
- [3] T.N. Gautier et al., “Kepler-20: A sun-like star with three sub-neptune exoplanets and two earth-size candidates”, *The Astrophysical Journal*, **749**, 19, (2012).
- [4] Hanbury R. Brown and R.Q. Twiss, *Proc. of the Royal Society of London, A*, **242** 300-324 (1957); Hanbury R. Brown and R.Q. Twiss, *Proc. of the Royal Society of London, A*, **243** 291-319 (1958).
- [5] I. Klein, M. Guelman, and S. G. Lipson, “Space-based intensity interferometer,” *Appl. Opt.* **46**, 4237 (2007).
- [6] D. Dravins and S. LeBohec, “Toward a diffraction-limited square-kilometer optical telescope: Digital revival of intensity interferometry,” *Proc. SPIE* **6986**, 698609 (2008).
- [7] S. LeBohec, B. Adamsa, I. Bondb, S. Bradburyb, D. Dravinsc, H. Jensenc, D. B. Kiedaa, D. Kressa, E. Munforda, P. D. N.neza, R. Pricea, E. Ribakd, J. Roseb, H. Simpsona, and J. Smitha, “Stellar intensity interferometry: Experimental steps toward long-baseline observations,” *Proc. SPIE* **7734**, 77341D (2010).
- [8] D. Dravins, S. LeBohec, H. Jensen, and P. D. Nunez, “Stellar intensity interferometry: Prospects for sub-milliarcsecond optical imaging,” *New Astronomy Reviews*, **56**, 143-167, (2012).
- [9] D. Dravins, S. LeBohec, H. Jensen, and P. D. Nunez, “Optical intensity interferometry with the Cherenkov Telescope Array,” *Astroparticle Physics*, **43**, 331-347, (2013).
- [10] P. D. Nunez, R. Holmes, D. Kieda, J. Rou, and S. LeBohec, “Imaging submilliarcsecond stellar features with intensity interferometry using air Cherenkov telescope arrays,” *Mon. Not. R. Astron. Soc.* **424**, 1006171011 (2012).
- [11] R. Holmes, B. Calef, D. Gerwe, and P. Crabtree, “Cramer-Rao bounds for intensity interfer-

- ometry measurements,” *Appl. Opt.* **52**, 5235-5246 (2013).
- [12] I. Klein, M. Guelman, and S. G. Lipson, *Appl. Opt.* **46**, 4237-47 (2007).
 - [13] T.B. Pittman, Y.H. Shih, D.V. Strekalov, and A.V. Sergienko, *Phys. Rev. A*, **52**, R3429 (1995);
 - [14] L. A. Lugiato, A. Gatti and E. Brambilla, *J. Opt. B: Quantum Semiclass. Opt.* **4**, S176S183 (2002).
 - [15] Agedi N. Boto, Pieter Kok, Daniel S. Abrams, Samuel L. Braunstein, Colin P. Williams, and Jonathan P. Dowling, *Phys. Rev. Lett.*, **85**, 2733-2736 (2000).
 - [16] Milena D’Angelo, Maria V. Chekhova, and Yanhua Shih, *Phys. Rev. Lett.*, **87**, 013602 (2001).
 - [17] K.W.C. Chan, M.N. OSullivan, and R.W. Boyd, *Phys. Rev. A*, **79**, 033808 (2009).
 - [18] D. Yu. Korystov, S. P. Kulik, and A. N. Penin, *JETP Letters*, **73**, No. 5, 21417218, (2001).
 - [19] R. Meyers, K.S. Deacon and Y. Shih, *Phys. Rev. A*, **77**, 041801(R) (2008).
 - [20] D.V. Strekalov, A.V. Sergienko, D.N. Klyshko, Y.H.Shih, *Phys. Rev. Lett.*, **74**, 3600 (1995).
 - [21] A. Gatti, E. Brambilla, M. Bache, and L. A. Lugiato, *Phys. Rev. A*, **70**, 013802 (2004); A. Gatti, E. Brambilla, M. Bache, and L. A. Lugiato, *Phys. Rev. Lett.*, **93**, 93602 (2004);
 - [22] Alejandra Valencia, Giuliano Scarcelli, Milena D’Angelo, and Yanhua Shih, *Phys. Rev. Lett.*, **94**, 063601 (2005).
 - [23] L.-G. Wang, S.Qamar,S.-Y. Zhu, and M.S. Zubairy, *Phys. Rev. A*, **79**, 033835 (2009).
 - [24] E.P. Horch, G.V. Belle, R.M. Genet, and B.D. Holenstein, *J. Astr. Instr.*, **2**, 1340009 (2013).
 - [25] J.P. Aufdenberg, H.-G. Ludwig, and P. Kervella, *Astrophysics Journal*, **633**, 424, (2005).
 - [26] A. Labeyrie, S.G. Lipson, and P. Nisenson, *An Introduction to Optical Stellar Interferometry*, ed. A. Labeyrie, S.G. Lipson, and P. Nisenson (2006).
 - [27] J.I. Castor, D.C. Abbott, and R.I. Klein, *Astrophysics Journal*, **195**, 157 (1975).
 - [28] J.K. Cannizzo, M.D. Still, S.B. Howell, M.A. Wood, and A.P. Smale, *The Astrophysical Journal*, **725**, 1393171404, (2010).
 - [29] Lars A. Buchhave, et al., *The Astrophysical Journal, Suppl. Ser.*, **197**, 3, (2011).
 - [30] B. Sicardy, et al., “Probing Titans atmosphere by stellar occultation17, *Nature* **343**, 35017353 (1990).
 - [31] B. Sicardy, et al., “Charons size and an upper limit on its atmosphere from a stellar occultation17, *Nature* **439**, 521754 (2006).
 - [32] F. Roques, et al., *Astron. J.*, **132**, 819-822 (2006).

- [33] H. Chang, et al., *Nature*, **442**, 660-663 (2006).
- [34] H. E. Schlichting, et al., “A single sub-kilometre Kuiper belt object from a stellar occultation in archival data”, *Nature* **462**, 89517897 (2009).
- [35] J. L. Elliot, et al., “Size and albedo of Kuiper belt object 55636 from a stellar occultation”, *Nature* **465**, 89717900 (2010).
- [36] B.C Lacki, “On the Use of Cherenkov Telescopes for Outer Solar System Body Occultations”, arXiv1402.1179L (2014).
- [37] V. McSwain, *Nature*, **505**, 296-297 (2014).
- [38] M. Moniez, *Astronomy and Astrophysics*, **412**, 105-120 (2003).
- [39] F. Habibi, et al., *Astronomy and Astrophysics*, **525**, A108 (2011).
- [40] D.V. Strekalov, B.I. Erkmen and Nan Yu, *Phys. Rev. A* **88**, 053837 (2013).
- [41] “Ghost imaging: from quantum to classical to computational”, B.I. Erkmen, and J.H. Shapiro, *Advances in Optics and Photonics* **2**, 40517450 (2010).
- [42] R. J. Glauber, *Phys. Rev.* **130**, 2529-2539, (1963).
- [43] K. W. C. Chan, M. N. O’Sullivan, and R. W. Boyd, *Opt. Express* **18**, 5562 (2010).
- [44] K.W.C. Chan, M.N. OSullivan, and R.W. Boyd, *Opt. Lett.*, **34**, 3343-3345 (2009).
- [45] H.-C. Liu and J. Xiong, “Properties of high-order ghost imaging with natural light”, *JOSA A*, **30**, 956-961 (2013).
- [46] T. Iskhakov, A. Allevi, D. A. Kalashnikov, V.G. Sala, M. Takeuchi, M. Bondani, and M.V. Chekhova, *Eur. Phys. J. Special Topics* **199**, 127-138, (2011).
- [47] G.Brida, M.V. Chekhova, G.A. Fornaro, M. Genovese, L.Lopaeva, I. RuoBerchera, *Phys Rev. A* **83**, 063807 (2011).
- [48] E.Lopaeva and M. Chekhova, *JETP Lett.* **91**, 447 (2010).
- [49] V. Malvimat, O. Wucknitz, and P. Saha, “Intensity interferometry with more than two detectors?”, *MNRAS* **437**, 79817803 (2014).
- [50] P.R. Fontana, “Multidetector intensity interferometers”, *J. Appl. Phys.* **54**, 473-480 (1983).
- [51] http://www.nrel.gov/solar_radiation/
- [52] A.S. Konopliv *et al.*, “The JPL lunar gravity field to spherical harmonic degree 660 from the GRAIL Primary Mission”, *J.Geophys. Research: Planets*, **118**, 1-20 (2013).
- [53] J.G. Cramer, *Phys. Rev. D*, **22**, 362-376 (1980); J.G. Cramer, *Rev. of Mod. Phys.*, **58**, 647 (1986); D.N. Klyshko, *Phys. Lett. A*, **128**, 133-137, (1988).

- [54] L. Mandel and E. Wolf, *Optical Coherence and Quantum Optics*. Cambridge: Cambridge Univ., (1995).
- [55] J. W. Goodman, *Statistical Optics*, Wiley, New York, Classics ed., 2000.
- [56] V. Laude, Opt. Comm., **138**, 394-402 (1997).
- [57] H. Gamo, “Stellar Intensity Interferometer. I. Signal-to-Noise Ratio for High-Intensity Radiation,” JOSA **56**, 441-451 (1966).
- [58] <http://www.astro.utoronto.ca/~patton/astro/mags.html>
- [59] Hanbury Brown, *The intensity interferometer. Its applications to astronomy.*, ed. Hanbury Brown, R. (1974).
- [60] M.V. Klivanov, P.E. Sacks and A.V. Tikhonravov, “The phase retrieval problem”, Inverse Problems **11**, 1-28, (1995).
- [61] R.B. Holmes, and M. S. Belenkii, “Investigation of the CauchyRiemann equations for one-dimensional image recovery in intensity interferometry”, JOSA A, **21**, 697-706 (2004).
- [62] R.B. Holmes, S. Lebohec, P.D. Nunez, “Two-dimensional image recovery in intensity interferometry using the Cauchy-Riemann relations”, Proc. of SPIE, **7818**, (2010).
- [63] J. R. Fienup, “Reconstruction of an object from the modulus of its Fourier transform,” Opt. Lett., **3**, 27-29 (1978).
- [64] J. R. Fienup , “Phase retrieval algorithms: a comparison,” Appl.Opt., **21**, 2758-2769 (1982).
- [65] J. R. Fienup and A. M.Kowalczyk, “Phase retrieval for a complex-valued object by using a low-resolution image,” J. Opt. Soc. Am. A, **7**, 450-458 (1990).
- [66] D. Dravins, and T. Lagadec, “Stellar intensity interferometry over kilometer baselines: Laboratory simulation of observations with the Cherenkov Telescope Array”, SPIE Proc. **9146**, *Optical and Infrared Interferometry IV*; J.K.Rajagopal, M.J.Creech-Eakman, F.Malbet, eds. (2014).
- [67] D.F.V. James, P.G. Kwiat, W.J. Munro, and A.G. White, “Measurement of qubits”, Phys. Rev. A, **64**, 052312 (2001).
- [68] J. Wambsganss, “Gravitational Lensing in Astronomy,” Living Rev. Relativity **1**, 12, (1998).
- [69] M. Moniez Gen. Relativ. Gravit., “Microlensing as a probe of the Galactic structure: 20 years of microlensing optical depth studies,” **42**, 2047-2074 (2010).
- [70] Xi-Hao Chen, Ivan N. Agafonov, Kai-Hong Luo, Qian Liu, Rui Xian, Maria V. Chekhova, and Ling-An Wu, Opt. Lett. **35**, 1166 (2010).